
Nam Hoai Pham

**Wavefields in porous media:
lithology, pressure and saturation effects**

A thesis presented for the degree of
Dr. Ing. (Doctor of Engineering) of the
Norwegian University of science and Technology
Department of Petroleum Engineering and Applied Geophysics

Mars, 2003

Summary

In the last few years, geophysics has been one of the most rapidly developing parts of petroleum geoscience. Previously, we have used seismics and the concepts of wave propagation for oil-gas exploration. Later, with more understanding of rocks, porous media, and the connections between geophysics, petrophysics, reservoir engineering and geology, several scientists have started investigations to study wave theory for the prediction and detection of many reservoir properties such as lithology, pore fluids, and pressure. The applications of elastic waves are made, not only in seismic surveying, but also in laboratory studies and well logging. The task is difficult, but this difficulty is correlated with the importance of these applications to acquisition, processing, and interpretation of high-resolution seismic data, and to deducing the physical properties of the rocks from seismic data. In fact, elastic analysis is one of the surest means available for the remote investigation of porous rocks. We are now becoming more quantitative and detecting properties ever on the finer scale of the rocks.

In my Dr.ing. project, I have built and investigated a model based on a more complete physical theory to account for the effects of many reservoir properties such as porosity, clay contents, pore fluid and pressure on acoustic wave velocities and attenuation. The model can match the seismic properties for the whole frequency range between laboratory measurements at ultrasonic frequencies (1MHz), sonic well data (10 kHz) and seismic data (30 Hz). It is based on Biot's theory (Biot, 1956) but includes other mechanisms such as thermal effects, intergranular friction, squirt flow treated as the viscoelastic effect, partial saturation and pressure effects (Pham et al., 2002c).

This project is a part of the EU project 'detection of overpressure from seismic and well data'. Therefore, the motivation of this project is to predict and detect the abnormally high pore pressure. Knowledge of pore pressure using seismic data helps in planning the drilling processes to control potentially dangerous abnormal pressures. Various physical processes cause anomalous pressures on an underground fluid. Proper pore pressure prediction should involve drilling engineers, geologists, geophysicists, and petrophysicists. As a practical test of this model it has been applied to predict overpressure in the Tune field (Carcione et al., 2002a). Moreover, the model can be used for detection of several other formation properties such as saturation, porosity, and clay content from elastic properties such as velocities and attenuation.

Project was extended to study the effects of partial saturation on P-wave velocity and attenuation by introducing a number of numerical experiments.

The results reveal the behaviour of natural sandstones. For instance: Both P- and S-wave velocities increase with increasing frequency and decreasing clay content. There is a strong decrease in velocity and Q -factor with increasing pore pressure. In partially saturated rocks, wave propagation depends not only on the saturation but also on the distribution of the fluid phase at various scales. The numerical result reveals the conversion of fast P-wave, into slow P-waves, is the main mechanism of wave dissipation and velocity dispersion in partially saturated rocks. This phenomenon may explain low signal-to-noise P-wave sections, since the presence of gas reduces velocities and increases attenuation. The strong responses of both P-wave velocity and dissipation correspond to permeability while at full saturation the sensitivity to permeability is insignificant, i.e., the biot's effect is insignificant in fully saturated rocks while it become dominant in partially saturated rocks. The relaxation peaks in our numerical result are generally in good agreement with White's model and the expression of relaxation peak (Dutta and Seriff, 1979; Gist, 1994).

Acknowledgements

I am grateful to professor Bjørn Ursin for his advice and support, and for giving me the opportunity to conduct this research.

I would like to thank my supervisor Dr. Hans B. Helle at Norsk Hydro, who continually gave me support and advice and with whom I had many interesting discussions during my stay at Norsk Hydro. I wish to express my gratitude to him.

I also wish to thank Dr. José M. Carcione at Istituto Nazionale di Oceanografia e di Geofisica Sperimentale (OGS), Trieste (Italy) for many interesting discussions and for supervision in the course of my project. Since he is a leading scientist within wave fields in porous media co-operation with him gave me invaluable knowledge and experience in numerical methods for wave field computation. Thanks also to Tommy Toverud for providing me with the high-resolution velocity cube of the Tune field that formed the input to the pore pressure prediction exercise (Chapter 5).

I am grateful to Dr. Børge Arntsen, Professor Michael Batzle and Harald Krostad for reviewing this work. I am thankful for their critical comments and useful suggestions for improving the quality of this thesis.

I want to thank Brian Farrelly and Alpana Bhatt for correcting my English and for improving my approach to many issues in this study.

I also thank Norsk Hydro for financial support and for access to data from the Tune field. Moreover, I am grateful to the management and staff of the Research Centre, Bergen for providing me with all facilities needed to conduct my research.

Financial support from the Norwegian Research Council (PetroForsk program) is acknowledged.

Finally, deep thanks to my family and my fiancée.

Trondheim, Mars 2003

Nam Hoai Pham

Symbols

A	dimensionless empirical parameter
a	dimensionless empirical parameter
a_{21}	tortuosity for the fluid flowing though the sand matrix
a_{13}	tortuosity for the sand flowing though the clay matrix
a_{31}	tortuosity for the clay flowing though the sand matrix
\mathbf{B}	friction matrix
b_{11}	friction coefficient between the sand matrix and the fluid
b_{13}	friction coefficient between the sand and the clay matrices
b_{33}	friction coefficient between the clay matrix and the fluid
C	clay content
c_1	consolidation coefficient of the sand matrix
c_3	consolidation coefficient of the clay matrix
d_m	deviator ($m = 1,3$)
E_k	kinetic energy
E_p	potential energy
F	viscous resistance force
f	frequency
f_c	critical frequency
g_1	consolidation coefficient of the sand matrix
g_3	consolidation coefficient of the clay matrix
K_c	bulk modulus of clay
K_f	fluid bulk modulus
K_s	bulk modulus of the sand grain
K_{av}	average bulk modulus
K_{cm}	bulk modulus of the clay matrix
K_{sm}	bulk modulus of the sand matrix
n_K	effective stress coefficient for bulk modulus
n_μ	effective stress coefficient for shear modulus
\mathbf{q}	relative displacement vector
Q	quality factor
\mathbf{R}	bulk stiffness matrix
\mathbf{r}	relative displacement vector
R	average radii of sand and clay particles

ρ	mass density matrix
ρ	effective density
ρ_c	clay density
ρ_f	fluid density
ρ_g	gas density
ρ_s	sand density
ρ_w	water density
ρ_{ij}	generalised mass coefficients ($i,j = 1,2,3$; see Appendix A)
p	pressure
p_c	confining pressure
p_d	differential pressure
p_e	effective pressure
P_o	pore pressure
r_{12}	geometrical aspect ratio of the boundary separating the sand grains from the fluid phase
r_{13}	geometrical aspect ratio of the boundary separating the sand grains from the clay
r_{23}	geometrical aspect ratio of the boundary separating the clay from the fluid phase
r_{31}	geometrical aspect ratio of the boundary separating the clay from the sand grains
T	total tortuosity
V_{Pm}	P-wave phase velocity ($m = 1,2,3$)
V_{Sm}	S-wave phase velocity ($m = 1,2$)
S_w	water saturation
S_{wc}	critical saturation
S_g	gas saturation
\mathbf{s}	microscopic particle-velocity vector
\mathbf{t}	microscopic particle-velocity vector
\mathbf{u}_m	displacement vector ($m = 1,2,3$)
\mathbf{v}_m	microscopic particle-velocity vector ($m = 1,3$)
\mathbf{w}_m	relative displacement vector ($m = 1,3$)
α_1	fluid/sand matrix coefficient
α_3	fluid/clay matrix coefficient
β_1	clay/sand matrix coefficient
β_3	sand/clay matrix coefficient
α_{Pm}	P-wave attenuation factor ($m = 1,2,3$)
α_{Sm}	S-wave attenuation factor ($m = 1,2$)
η_f	fluid viscosity
η_g	gas viscosity
η_w	water viscosity
κ	permeability

κ_1	(partial) permeability of the sand matrix
κ_3	(partial) permeability of the clay matrix
κ_e	effective permeability
κ_{ri}	relative permeability ($i = w, g$)
Λ_{Pm}	P-wave root of the dispersion equation ($m = 1, 2, 3$)
μ_c	shear modulus of the clay ;
μ_s	shear modulus of the sand grains
μ_{cm}	shear modulus of the clay matrix
μ_{sm}	shear modulus of the sand matrix
$\boldsymbol{\mu}$	shear stiffness matrix
μ_{11}	same as μ_{sm}
μ_{13}	shear coupling between the sand and the clay matrices
μ_{33}	same as μ_{cm}
Ω_{sm}	S-wave root of the dispersion equation ($m = 1, 2$)
ω	angular frequency : $2\pi f$
ϕ_c	proportion of the clay
ϕ	proportion of the fluid or porosity
ϕ_s	proportion of the sand grains
θ_m	dilatation ($m = 1, 2, 3$)
τ	stress

Contents

Summary	iii
Acknowledgements	v
Symbols	vii
1 Introduction	1
2 Poro-elastic representation of shaley sandstones	7
2.1 Introduction	7
2.2 Biot-type three-phase theory	8
2.2.1 Model for shaley sandstone	9
2.2.2 Dry-rock moduli	9
2.2.3 Phase velocity and attenuation	10
2.2.4 Application and limitations of the model	12
2.3 Permeability model.....	13
2.3.1 Tortuosity	13
2.3.2 Permeability.....	14
2.3.3 Partial permeability of sand and clay matrices.....	16
2.4 Viscodynamic operator.....	19
2.5 Case study.....	22
2.6 Summary.....	25
3 Viscoelastic effects	27
3.1 Introduction	27
3.2 Viscoelastic concept.....	29
3.3 Squirt flow and the Zener model.....	30
3.4 Constant- Q model.....	31
3.5 Discussions	33
4 Partial saturation	35
4.1 Introduction	35

4.2	Relative permeability	36
4.3	Mixing laws for multi-fluid model	38
4.4	Case study	40
4.5	Discussion and conclusions	49
5	Pressure effects	51
5.1	Introduction.....	51
5.2	Method	53
5.2.1	Effective stress coefficients	54
5.2.2	Dry-rock moduli as function of effective pressure	55
5.2.3	Hashin-Shtrikman upper bounds	55
5.2.4	Gas dependencies on pressure and temperature	56
5.2.5	Pore pressure prediction procedure.....	57
5.3	Case study	61
5.4	Pore pressure prediction on Tune field.....	65
5.4.1	Application and analysis on Tune field.....	65
5.4.2	Velocity determination by tomography of depth migrated gathers	72
5.4.3	Application of the velocity model for pressure prediction	73
5.5	Discussion and conclusions	80
6	Numerical experiments-Velocity and attenuation in partially saturated rocks	81
6.1	Introduction.....	81
6.2	Fractals and saturation distribution.....	85
6.3	Phase velocity and attenuation estimation	86
6.4	Wave simulation and analysis of the wavefields.....	91
6.4.1	Wave responses in partially saturated rocks.	91
6.4.2	heterogeneities in rock material versus fluid distribution fluid	102
6.5	Conclusions.....	106
7	Comparison of White's model with numerical experiments in partially saturated rocks	107
7.1	Introduction.....	107
7.2	White's model for partial saturation	108
7.3	Results.....	112
7.4	Conclusion	130
8	Conclusions and future work	131

Appendix A	Three-phase Biot-type theory of shaley sandstones	135
Appendix B	Numerical algorithm for wave propagation in poro-elastic isotropic media	141
References		149

Chapter 1

Introduction

The successful development in geophysics of a better interpretation of seismic data related to reservoir properties depends on knowledge of wave propagation through porous media. Porous media are, by their essence, composite and multiphase. Composite because the solid fraction - the skeleton - is formed of grains whose chemical or crystalline features are often different and multiphase because this solid fraction is always associated with a gas or liquid phase that occupies the voids between the grains. This microscopic heterogeneity of the porous medium induces a complex macroscopic physical behaviour sensitive to slight variation in fluid content or of the solid structure. The acoustics of porous media attempts to characterise the behaviour of the waves by synthesising between the rigor of the laws of mechanics and the natural disorder of porous media. Several theories have been developed and applied in this field.

Gassmann (1951) derived a relation between the individual elastic properties of the solid fabric (skeleton, matrix) and the effective elastic properties of the composite medium. Biot (1956) developed the theory for the propagation of acoustic waves in a porous material containing a compressible viscous fluid. He developed different theories for the low and high frequency waves. For low-frequency waves, the concept of Poiseuille flow was used, while for the high-frequency range, this concept breaks down, and potential flow is used instead. Biot found that in general there are two P-waves present, one slow and one fast.

The most interesting area of application, at least for its economic benefits, is for sandstone reservoirs saturated with hydrocarbons. In general, sandstones contain some clay material that considerably affects the wave properties, such as compressional and shear wave velocity and attenuation. In this study, based on physical theory combined with experimental data, we have attempted to build a more comprehensive multiphase model for shaley sandstone, which is one of the common rocks in hydrocarbon reservoirs. Figure 2.1 shows an example of typical

rocks in a sandstone reservoir where clay is present. The theory can be used for other kinds of rocks such as sandy shale, carbonates, and others.

Unlike previous attempts based simply on slowness and/or modulus averaging or on two-phase models, we started by investigating the Biot-type three-phase theory (Leclaire et al., 1994; Carcione et al., 2000) that considers the existence of two solids, i.e. sand grains and clay particles, and the fluid. The terms responsible for the interaction between sand grains and clay particles are included in the kinetic and potential energies of the system. The bulk and shear moduli of the sand and clay matrices versus porosity are obtained using the (modified) relationships of Krief et al. (1990), where empirical parameters can be adjusted for calibrating the model against experimental data.

Since the model is based on a Biot-type formulation of the wave equation, additional compressional and shear waves are predicted and their frequency characteristics are shown to be strong functions of clay and fluid contents. In the particular case when the clay content tends to zero, the model is shown to behave like the classical two-phase Biot's medium for a fully saturated pure sand matrix.

Moreover, several effects have been considered and taken into account in order to obtain a comprehensive multiphase model. These are; (i) the effect of clay on permeability, (ii) the frequency dependent viscodynamic operator, (iii) viscoelasticities of the grain material and squirt flow (iv) fluid pressure, and (v) partial saturation when there is more than one fluid present in pores.

In Biot's theory, which takes into account the different particle displacements of solid and fluid components, the permeability is important for the dynamic dissipation of acoustic waves. Here, we use a permeability model of the Kozeny-Carman type (Carman, 1961), which relies on porosity, clay content and tortuosity, and is calibrated against the experimental data of Klimentos and McCann (1990).

The acoustic waves passing through porous media supply energy to the media and induce a fluid flow. Low frequency waves (e.g. seismic frequencies) induce laminar flow, while, at high frequencies (e.g. sonic and ultrasonic frequencies) the laminar flow breaks down and becomes turbulent. In this case, the viscodynamic operator should be introduced to account for the transition from laminar to turbulent flow regimes. The viscodynamic operator is implemented by using a dynamic tortuosity (Johnson et al., 1987), which accounts for the dynamic properties of the fluid motion in the pores and is valid for the whole frequency range.

Wave properties such as velocities and attenuation in fluid saturated rocks are known to vary with frequency. Biot (1956) considers this, but several observations have demonstrated that Biot's theory of dynamic poro-elasticity

alone cannot explain the measured dispersion of real rocks. The dispersion due to local flow (squirt flow), grain friction, thermal loss, and intrinsic attenuation is not accounted for. The essential concept behind the squirt flow (local flow) is that the fluid tends to flow from the compliant (mechanically weaker) regions to the less compliant (mechanically stronger) regions when an acoustic wave deforms the pore space. Fluid in flat cracks tends to be squeezed into more rounded pores, which are stiffer when the acoustic wave passes. In order to describe the squirt flow phenomenon we use the standard linear-solid model (Zener type) (Carcione, 1998). For presenting other attenuation mechanisms such as friction loss, thermal loss, and intrinsic attenuation, we use a constant- Q model, which is applied to the dry-rock moduli (Kjartansson, 1979). Constant- Q models provide a simple parameterisation of seismic attenuation in natural rocks in oil exploration and in seismology (Pham et al., 2001 and 2002c).

The problem is more complex in the case when there is more than one fluid type in the porous rock. A simple solution is to apply mixing laws to obtain the effective properties of the mixture. For liquid/liquid mixtures such as oil/water, Biot's theory may apply even at high frequencies since the properties of the two fluids are similar. For a gas/liquid mixture, on the other hand, the problem is entirely different since their properties, i.e. viscosity, density and bulk modulus may differ by orders of magnitude and the Biot-Gassmann theory cannot reproduce the observed features at high frequency. The main challenge was thus to determine the appropriate mixing laws that were applicable within the framework of Biot's theory to reproduce the experimental data. We introduced the semi-empirical model of Brie et al. (1995) for the bulk modulus of a gas/fluid mixture, modified to account for its frequency dependency (Pham et al., 2002c). Moreover, numerical wave simulation experiments using the Biot poroelastic equations were conducted to support the results (Pham et al., 2002a,b, Helle et al., 2002a and Carcione et al., 2002b).

Observations show that the velocity and quality factor (Q -factor) increase with increasing confining pressure and decrease with pore pressure. This is usually considered to be due to the closing of cracks in the rock matrix, inducing a stiffening of the rocks and preventing the fluid motions. In the present study, the pressure effects are introduced by using the effective stress law of Carcione and Gangi (2000a,b). The pressure dependency of the dry-rock moduli is determined by inversion of well data or laboratory measurements.

For instance, this model was applied to pressure prediction of the Tune field (Carcione et al., 2001b, 2002a). Here, calibration of the model was based on well log data to obtain the dry-rock moduli and the effective stress coefficient as a function of depth and pore pressure. Then the seismic velocity derived from velocity inversion was fitted with the theoretical velocities by using pore pressure as a fitting parameter.

The sensitivity of phase velocities and attenuation to pore fluids lies in the heart of most schemes for direct detection of hydrocarbons. However, the task of interpreting the seismic response is difficult due to the complexity of the rock and is harder when two or more fluids occupy the pore space. In order to study the effects of saturation and fluid distribution on the wave velocities and attenuation as a function of frequency, we perform numerical wave propagation experiments in rocks partially saturated with water and gas, using a 2-D poroelastic algorithm developed by Carcione and Helle (1999). This method is highly accurate provided a sufficiently fine grid is used. Moreover, the generation of snapshots and seismograms provides direct insight into the various wave phenomena and hence constitutes an important aid in interpreting and understanding the physical mechanisms of wave propagation in realistic media. The numerical results are in qualitative, and reasonable quantitative, agreement with published experimental results. Furthermore, our numerical experiments of wave propagation are compared with those of White's theory for partial saturation (White, 1975).

The main objective of this project is to develop a rock physics model based on a more complete physical theory enabling us to match the wave properties for all frequencies from the seismic to the ultrasonic band. One of the central aspects of the project is the need for a better understanding of the relationship between the seismic properties of reservoir rocks, their production related properties (porosity, permeability, clay content) and their state (saturation, pore pressure).

In exploration, elastic means P- and S-waves, while acoustic means P-waves only. Poro-elasticity refers to a porous media where only Biot's effect (global flow) contributes to wave dissipation. Poro-viscoelasticity refers to a porous media where there exist additional dissipation mechanisms such as squirt flow, viscous loss in the solid, thermal effects, and others.

In chapter 2, I introduce the poroelastic representation of shaley sandstones, which is based on Biot's theory applied to a three-phase medium, i.e. the two solids sand and clay and a single fluid (Carcione et al., 2000). The permeability of the composite matrix is based on the Kozeny-Carman model. Moreover, the viscoelastic effect is implemented in the theory. An example is provided to demonstrate the variation in velocities and attenuation of the different wave modes as a function of clay content and frequency. Here we have five different wave modes, three compressional waves (one fast wave and two slow waves) and two shear waves (one fast and one slow wave). In chapter 3, the viscoelastic effect is introduced into the theory. Here, the constant- Q model is implemented in the moduli of the sand matrix and the standard linear-solid model presented for squirt flow is introduced in the fluid-solid coupling modulus (Carcione, 1998). In chapter 4, I present the effect of partial water/gas saturation on elastic wave response. In this model, we use the empirical fluid mixing laws for the mixture of fluids. The model is calibrated and compared with experimental data of King et al. (2000) (Pham et al. 2001 and 2002c). Chapter 5 shows the effect of pressure

on elastic wave responses and a method for pressure prediction from seismic reflection data. The method is applied to the Tune field in the Viking Graben of the North Sea to predict the high-pressure zone from 3-D seismic data (Carcione et al., 2002a). In chapter 6 numerical experiments in patchy saturated rocks are presented. Here the fluid distribution is based on data from Cadoret et al. (1995) and modelled using the random-fractal approach (Frankel and Clayton, 1986). The wave simulation is based on the numerical solution of the poroelastic wave equation (Biot, 1962; Biot and Willis, 1957) on a 2-D staggered mesh (Carcione and Helle, 1999, Pham et al., 2002a,b and Helle et al., 2002a). Chapter 7 is an extension of Chapter 6 and is devoted to the comparison of results from White's theory of wave propagation in partially saturated rocks with those from numerical experiments (Carcione et al., 2002b).

Chapter 2

Porosity-elastic representation of shaly sandstones

2.1 Introduction

Modelling the acoustic properties of shaly sandstones implies quantifying the variations of wave velocities V_p , V_s and their amplitudes versus porosity, clay content and frequency. This is done within the framework of Biot's theory of porosity-elasticity.

For clay/sand mixtures, such an approach requires the consideration of a medium consisting of three phases: sand, clay, and fluid. A three-phase Biot-type theory was developed by Leclaire et al. (1994) for frozen porous media. This three-phase theory assumes that there is no direct contact between sand grain and ice, implying the existence of a water layer around the grains, isolating them from the ice. The model, which predicts three compressional waves and two shear waves, has recently been applied, with some minor modifications, to modelling the acoustic properties of permafrost (Carcione and Seriani, 1998) and gas hydrates (Carcione and Tinivella, 2000)

Carcione et al. (2000) replaced ice with clay and included the terms responsible for the interaction between the sand grains (pure quartz grains) and the clay particles in the potential and kinetic energies. Lagrange's equations provide the differential equations of motion. A plane-wave analysis gives the wave velocities and attenuation factors of the different modes. The bulk and shear moduli of the sand and clay matrices versus porosity are obtained from a relationship proposed by Krief et al. (1990). This relationship introduces two empirical parameters that can be obtained by calibrating the model with experimental data. An additional parameter provides one more degree of freedom for adjusting the velocity-porosity curves (at constant clay content) to the data.

The model for shaley sandstones provided by Carcione et al. (2000) is somewhat similar to that recently proposed by Goldberg and Gurevich (1998). An important difference, however, is associated with our three-phase approach. Indeed, Goldberg and Gurevich (1998) assumed that the medium is composed of only two phases, solid and fluid. The solid matrix, in turn, is a composite material, made of sand grains and clay particles. The elastic moduli of the solid/fluid mixture were derived using the Gassmann's equation. However, the latter is valid only when the solid matrix is homogeneous (Brown and Korrington, 1975). This implies that the sand and clay particles are mixed homogeneously and form in effect composite grains, which in turn form the rock matrix. The three-phase approach is free of such assumption, but it also implies a particular topological configuration, namely the one where sand and clay form two continuous and interpenetrating solid matrices (see Figure 2.1).

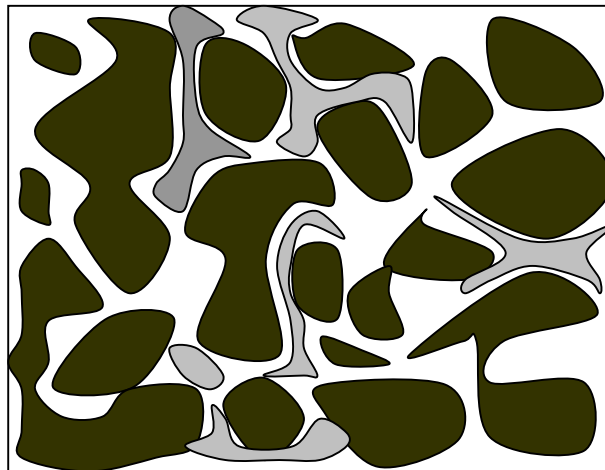


Figure 2.1: Interpenetrating sand (dark grey) and clay (light grey) matrices forming the composite skeleton of the shaley sandstone.

2.2 Biot-type three-phase theory

As mentioned above, we have started by investigating the Biot-type three-phase theory that considers the existence of two solids (i.e. sand grains and clay particles) and one fluid. The theory developed first by Leclaire et al. (1994) explicitly takes into account the presence of three phases: solid, ice and water, which is applied for frozen media. Later, Carcione et al. (2000) replaced ice with clay and included the contributions to the potential and kinetic energies due to the contact between the sand grains and the clay, which are needed for shaley sandstone.

2.2.1 Model for shaley sandstone

Following Carcione et al. (2000), the equation of motion can be written in matrix form as

$$\mathbf{R} \text{ grad div } \mathbf{u} - \boldsymbol{\mu} \text{ curl curl } \mathbf{u} = \boldsymbol{\rho} \ddot{\mathbf{u}} + \mathbf{B} \dot{\mathbf{u}} \quad (2.1)$$

where \mathbf{u} is the displacement field, the dot denotes as time differentiation.

$$\mathbf{R} = \begin{pmatrix} R_{11} & R_{12} & R_{13} \\ R_{12} & R_{22} & R_{23} \\ R_{13} & R_{23} & R_{33} \end{pmatrix} \quad \text{and} \quad \boldsymbol{\mu} = \begin{pmatrix} \mu_{11} & 0 & \mu_{13} \\ 0 & 0 & 0 \\ \mu_{13} & 0 & \mu_{33} \end{pmatrix} \quad (2.2)$$

\mathbf{R} and $\boldsymbol{\mu}$ are the bulk and shear stiffness matrices, while

$$\boldsymbol{\rho} = \begin{pmatrix} \rho_{11} & \rho_{12} & \rho_{13} \\ \rho_{12} & \rho_{22} & \rho_{23} \\ \rho_{13} & \rho_{23} & \rho_{33} \end{pmatrix} \quad (2.3)$$

is the mass density matrix, and

$$\mathbf{B} = \begin{pmatrix} b_{11} & -b_{11} & 0 \\ -b_{11} & b_{11} + b_{33} & -b_{33} \\ 0 & -b_{33} & b_{33} \end{pmatrix} \quad (2.4)$$

where index $i = 1,2,3$ denotes sand, water and clay, respectively. The parameter b_{13} , which describes the interaction between the sand and clay matrices, has been assumed equal to zero. The fact that there is a frictionless connection between the two constituents can be interpreted as meaning that the sand and clay frames are welded together. There is an interchange of kinetic energy (described by ρ_{13}) and potential energy (described by R_{13} and μ_{13}) at the contact points, but no dissipation. Details are given in Appendix A and in Carcione et al. (2000).

2.2.2 Dry-rock moduli

The model of Krief et al. (1990) is considered to obtain estimates of the dry-rock moduli K_{sm} , μ_{sm} (sand matrix), K_{cm} and μ_{cm} (clay matrix) versus porosity and clay content. The porosity dependency of the sand and clay matrices should be consistent with the concept of critical porosity, since the moduli should vanish above a certain value of the porosity (usually from 0.4 to 0.5). This dependency is determined by the empirical coefficient A (see equation 2.5). The coefficient A

depends on texture of the rocks (the orientation of grains and the shape of the pores). This relation was suggested by Krief et al. (1990) and applied to sand/clay mixtures by Goldberg and Gurevich (1998). Moreover, in some rocks there is an abrupt change of rock matrix properties with the addition of a small amount of clay. This is attributed to softening of cement, clay swelling and surface effects, i.e. the velocities decrease significantly when the clay content increases from zero to a few percent (Goldberg and Gurevich, 1998). In order to model this effect Carcione et al. (2000) introduced an empirical coefficient a for the shear modulus of sand matrix with values in the range $[0,1]$. The bulk and shear moduli of the sand and clay matrices are respectively given by

$$\begin{aligned} K_{sm} &= K_s[1-C][1-\phi]^{1+A/[1-\phi]} \\ K_{cm} &= K_c C[1-\phi]^{1+A/[1-\phi]} \\ \mu_{sm} &= F_\mu K_{sm} \mu_s / K_s \\ \mu_{cm} &= K_{cm} \mu_c / K_c, \end{aligned} \quad (2.5)$$

where the additional factor $F_\mu = \exp[-((1-C)C)^a]$ is introduced by Carcione et al. (2000) ($F_\mu = 1$ for the Krief et al.'s model). C is the clay content, ϕ is porosity, K_s and μ_s are the bulk and shear moduli of the sand grains, while K_c and μ_c are those of the clay particles. Krief et al. (1990) set the A parameter to 3 regardless of the lithology, and Goldberg and Gurevich (1998) obtained values between 2 and 4, while Carcione et al. (2000) used $A = 2$. The ideal approach is to estimate its value using well data from the study area.

2.2.3 Phase velocity and attenuation

By solving the equation (2.1), we obtain three solutions of the P-wave velocities and attenuation and two solutions for shear wave.

The three compressional velocities of the three-phase porous medium are given by

$$V_{Pi} = \left[\text{Re}(\sqrt{\Lambda_i}) \right]^{-1}, \quad i=1,\dots,3, \quad (2.6)$$

and the attenuations are given by

$$Q_{Pm}^{-1} = -\frac{\text{Im}(\Lambda_i)}{\text{Re}(\Lambda_i)}, \quad i=1,\dots,3, \quad (2.7)$$

where Re and Im are the real and imaginary parts and Λ_i are obtained from the generalised characteristic equation $\det[\Lambda \mathbf{R} - \tilde{\mathbf{p}}] = 0$, which yields

$$\Lambda^3 \det[\mathbf{R}] - \Lambda^2 \text{tr}[\overline{\mathbf{R}}\tilde{\boldsymbol{\rho}}] + \Lambda \text{tr}[\mathbf{R}\overline{\tilde{\boldsymbol{\rho}}}] - \det[\tilde{\boldsymbol{\rho}}] = 0, \quad (2.8)$$

where tr denotes the trace, the overbar denotes the cofactor matrix (e.g., Fedorov, 1968), and the effective matrix,

$$\tilde{\boldsymbol{\rho}} = \boldsymbol{\rho} - \frac{i\mathbf{B}}{\omega} \quad (2.9)$$

is defined in the frequency domain.

For shear wave propagation, an analogous method to the one for longitudinal waves may be used. In fact, we simply have to replace the rigidity matrix \mathbf{R} by the shear modulus matrix $\boldsymbol{\mu}$ in the equations. Disregarding the matrix \mathbf{B} , the characteristic equation for transverse waves is written as

$$\Omega^2 \text{tr}[\overline{\boldsymbol{\mu}}\tilde{\boldsymbol{\rho}}] - \Omega \text{tr}[\boldsymbol{\mu}\overline{\tilde{\boldsymbol{\rho}}}] + \det[\tilde{\boldsymbol{\rho}}] = 0, \quad (2.10)$$

and the two shear-wave velocities V_{Si} are given by

$$V_{Si} = \left[\text{Re}(\sqrt{\Omega_i}) \right]^{-1}, \quad i = 1, 2 \quad (2.11)$$

The attenuations are given by

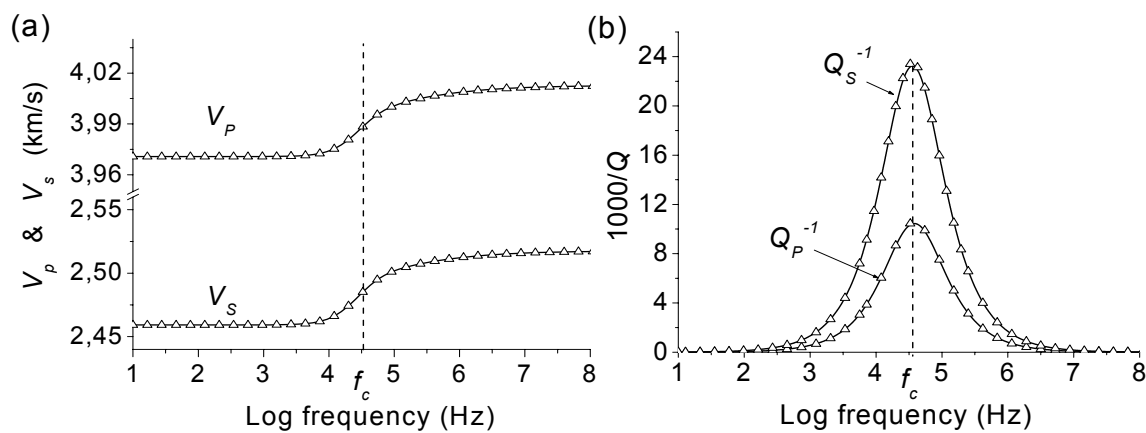
$$Q_{Si}^{-1} = -\frac{\text{Im}(\Omega_i)}{\text{Re}(\Omega_i)}, \quad i = 1, 2 \quad (2.12)$$

Testing the theory was done by comparing the results of the three-phase Biot-type model with $C = 0$ against the classical two-phase Biot-type model with one solid and one fluid part. The rock parameters are; $\phi = 0.25$, $C = 0$, permeability $\kappa = 528$ mD, empirical parameters $A = 2$, $a = 0.5$ and the remaining properties from Table 2.1. The results are shown in Figure 2.2.

The results display an excellent match between three-phase Biot-model and the two-phase Biot-model in the limiting case when $C = 0$. f_c is the critical frequency when the fluid flow goes from unrelaxed to relaxed state, and the P- and S-velocities undergo a transition from low to high values.

Solid grain	bulk modulus, K_s	39 Gpa
	shear modulus, μ_s	39 Gpa
	density, ρ_s	2650 kg/m ³
	average radius, R_s	50 μ m
Fluids	bulk modulus, K_w	2.4 GPa
	density, ρ_w	1000 kg/m ³
	viscosity η_w	1.798 cP

Table 2.1: Material properties of the clay-bearing sandstone.

Figure 2.2: An example of velocities (a) and attenuation (b) versus frequencies. The solid lines are obtained from two-phase Biot theory, while the points are from three-phase Biot theory. f_c is the critical frequency.

2.2.4 Application and limitations of the model

The Three-phase model can be applied to inversion of well logs for model calibration at sonic frequencies and subsequently applied to inversion of low-frequency surface seismic data. The model is based on a Biot-type formulation of the equation of motion. However, like the general Biot theory (1956), the Biot-type three-phase model has the following assumptions and limitations:

- Statistical isotropy and homogeneity of the pore and solid structures.
- The grains in the solid part are connected.
- The pore volume is connected.
- The pore size distribution is concentrated around its average value.
- Poiseuille fluid flow (laminar flow) valid for only for the low-frequency range.

Due to the complexity of the natural rocks and its pore-fill, Biot's theory alone is not sufficient for modelling porous media. To approach the optimal accuracy of the model several effects should be added and taken into considerations such as viscodynamic effects, viscoelastic effects, pressure, and partial saturation.

2.3 Permeability model

(Absolute) permeability is a measure of the capacity of the porous medium to transmit fluids and hence a property of the rock, which is independent of fluid type. Unlike Gassmann's theory, the Biot theory accounts for the differential movements of the fluid relative to the solid matrix. Therefore, an accurate permeability model would be required, which can link the permeability to common rock parameters such as clay content and porosity.

However, the introduction of clay in sand sandstones has strong impact on its permeability. The permeability of a clay matrix is generally very low since the clay particle size is small ($\sim 1 \mu\text{m}$), compared to the sand grains ($\sim 100 \mu\text{m}$). In this section, an empirical permeability model is presented based on Kozeny-Carman relation (Carman, 1961, Mavko and Nur, 1997). The permeability does not depend only on porosity and tortuosity, but also on clay content.

2.3.1 Tortuosity

Tortuosity is one of the dynamic parameters of flow in the rock. It is defined as the square of the ratio of total flow-path length to length of the sample, which depends on porosity and structure of the rock,

$$T = \left(\frac{l}{L} \right)^2. \quad (2.13)$$

Based on the theory of Berryman (1980), the tortuosity parameters are expressed in three phase media by

$$\begin{aligned} a_{21} &= \frac{\phi_s}{\phi} r_{12} + 1, \\ a_{23} &= \frac{\phi_c}{\phi} r_{23} + 1, \\ a_{13} &= \frac{\phi_c}{\phi_s} r_{13} + 1, \\ a_{31} &= \frac{\phi_s}{\phi_c} r_{31} + 1 \end{aligned} \quad (2.14)$$

where a_{ij} are partial tortuosity parameters for i -phase in j -phase and r_{ij} characterises the geometrical features of the pores (equal to 0.5 for spheres).

Carcione et al. (2000) expressed the total tortuosity as a function of partial tortuosity and clay content

$$\frac{1}{T} = \frac{1-C}{a_{21}} + \frac{C}{a_{23}}, \quad (2.15)$$

where a_{21} and a_{23} are tortuosity parameters for sand and clay matrix, respectively. Equation (2.15) considers that the tortuosity of the rock can be obtained by using an analogy with electric circuits. It is given by a parallel connection of resistances, where the resistances are the tortuosity through the sand matrix, and the tortuosity through the clay matrix. This analogy uses the fact that increasing tortuosity increases the resistance to fluid flow. Figure 2.3a shows the variation of tortuosity with porosity and clay content based on equation (2.15). Observe, for instance that $T \rightarrow \infty$ for $\phi \rightarrow 0$ and $T \rightarrow 1$ for $\phi \rightarrow 1$, as expected from physical reasoning.

2.3.2 Permeability

The intergranular space displays a relationship of porosity, ϕ , and permeability, κ , which is fairly well-known experimentally, at least for grains of sub-spherical shape and constant grain size distribution. The Kozeny-Carman (Carman, 1961) relation provides a way to estimate the permeability of a porous medium in terms of generalised parameters such as porosity, surface area, particle size, and so forth.

The combination of the Darcy and Poiseuille equations for the flow through a pipe, gives a permeability model expressed in terms of ϕ and grain dimension d , and tortuosity T ,

$$\kappa = \frac{B\phi^3 d^2}{T}, \quad (2.16)$$

where B is a geometric factor. Equation (2.16) shows the strong effects of particle size, d , and porosity on permeability. The tortuosity, T , is also an important factor that has to be taken into account.

Mavko and Nur (1997) suggested the existence of a percolation porosity ϕ_p , below which the remaining porosity is disconnected and does not contribute to

flow. The effect of percolation can easily be incorporated into the model by replacing ϕ with $(\phi - \phi_p)$ in the Kozeny-Carman relation

$$\kappa = \frac{B(\phi - \phi_p)^3 d^2}{T}. \quad (2.17)$$

To include the effect of clay in the rock we follow Dullien (1991) who suggested that the Kozeny-Carman relation can still be applied for a distribution of particle sizes by substituting d by an effective particle size, \bar{d} , defined by

$$\frac{1}{\bar{d}} = \frac{\sum_i \frac{m_i}{d_i}}{\sum_i m_i} = \sum_i \frac{f_i}{d_i}, \quad (2.18)$$

where f is the volume fraction, i is the index for sand and clay and m is mass of the particle assuming the densities of clay and sand are the same.

Finally, from equations (2.17) and (2.18) the permeability as function of porosity and clay is obtained

$$\kappa = B \frac{(\phi - \phi_p)^3}{T} \left(\frac{(1 - \phi - \phi_p)}{\frac{\phi_s}{d_s} + \frac{\phi_c}{d_c}} \right)^2$$

or simplified

$$\kappa = B \frac{(\phi - \phi_p)^3}{T \left(\frac{1-C}{d_s} + \frac{C}{d_c} \right)^2}, \quad (2.19)$$

where

$$C = \frac{\phi_c}{\phi_s + \phi_c} \quad \text{and} \quad \phi + \phi_s + \phi_c = 1, \quad (2.20)$$

and ϕ_s and ϕ_c are the volume fractions for sand and clay, respectively. Equation (2.19) is not restricted to any particular model of the pore space. The information about the pore geometry and grain sizes is contained in the parameters B , d_s , d_c and τ . This description of permeability assumes an even distribution of the clay particles in the elementary volume. In this sense, the description is consistent with the model of interpenetrating sand and clay matrices on which the three-phase Biot-type theory is based.

The geometrical factor B may vary from one rock type to another. In this study, the value of B is estimated as 15 by fitting the equation (2.19) with the experimental data for sandstones of Klimentos and McCann (1990) and using $\phi_p = 0.035$ (Mavko et al., 1998, p 262).

Figure 2.3b the permeability versus porosity and clay content, for various values of the clay content and porosity, respectively. In general, the permeability (and porosity) data from core measurements exhibit a scattered appearance, and there are several reasons for this (Worthington, 1991), mainly related to the core handling and measurement methods. This problem was also discussed in Helle et al. (2001). In view of this, the fit between the model with the experimental data is considered acceptable. Note the strong decrease in permeability due to the addition of a small amount of clay in pure sandstones.

2.3.3 Partial permeability of sand and clay matrices

In the three-phase Biot-type model, the fluid-sand and fluid-clay dynamic interactions are considered separately. Therefore, expressions for the partial permeabilities of sand and clay matrices have to be developed. The expression for permeability obtained in the previous section is the permeability, κ , for a rock of mixed particle size and cannot directly be used in our three-phase model. Thus, the conversion of κ to partial permeabilities κ_1 and κ_3 , corresponding to sand and clay matrices, respectively, is required. Following Carcione et al. (2000), the permeability, κ , is given by

$$\kappa = \kappa_1 \phi_s + \kappa_3 \phi_c, \quad (2.21)$$

and the ratio of partial permeabilities is

$$\frac{\kappa_3}{\kappa_1} = \left(\frac{d_c}{d_s} \right)^2 \left(\frac{\phi_s}{\phi_c} \right) \quad (2.22)$$

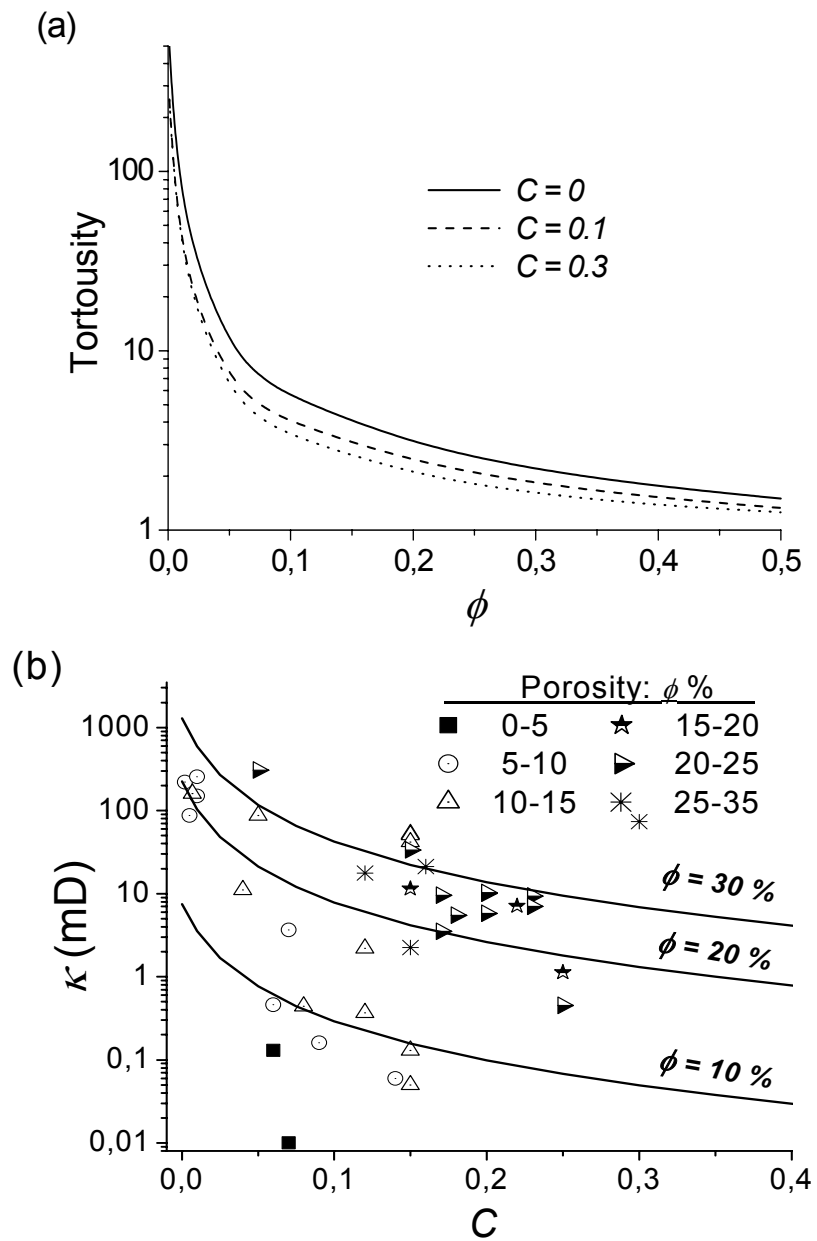


Figure 2.3: Tortuosity versus porosity with different clay content (a), and calibration of permeability model with experimental data (Klimentos and McCann, 1990) (b).

Then from equations (2.21) and (2.22), the partial permeabilities can be expressed by (see figure 2.4)

$$\kappa_1 = \frac{\kappa}{\phi_s \left[1 + \left(\frac{d_c}{d_s} \right)^2 \right]}, \quad (2.23)$$

and

$$\kappa_3 = \frac{\kappa}{\phi_c \left[1 + \left(\frac{d_s}{d_c} \right)^2 \right]} \quad (2.24)$$

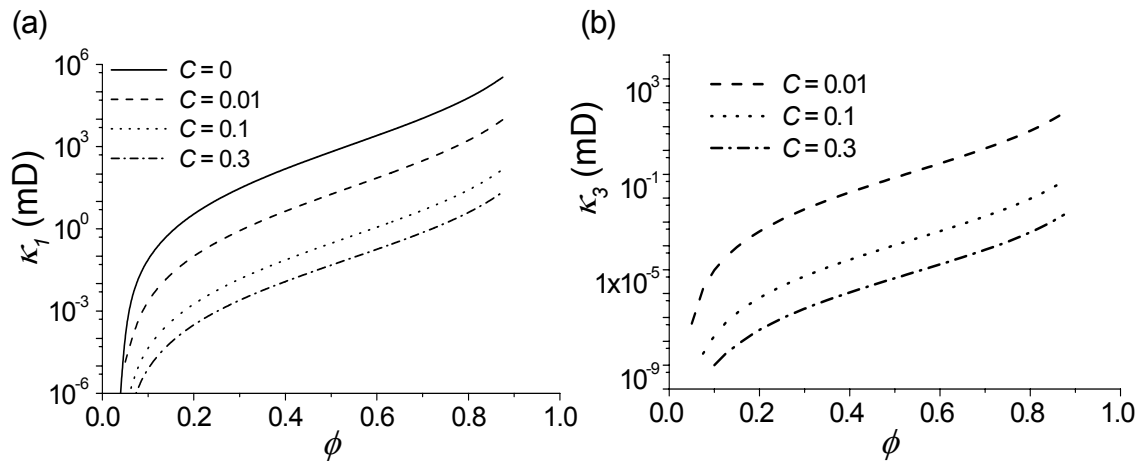


Figure 2.4: Partial permeability for sand (a) and clay (b) matrix as a function of porosity and clay content (note that $\kappa_3 \rightarrow \infty$ for $C \rightarrow 0$).

2.4 Viscodynamic operator

In a Poiseuille flow (laminar flow), energy dissipation is dominated by viscous drag in the boundary layer at the solid-fluid contact. In this case, the fluid front is parabolic and parallel to the pore wall. When the laminar flow breaks down and becomes turbulent, the viscous drag at the wall is less important, while the inertial forces in the fluid cause the flow pattern to be more irregular.

Flow characteristics depend on the size of the pores and the viscous skin depth, δ , given by

$$\delta = \sqrt{\frac{\eta_f}{\pi f \rho_f}}, \quad (2.25)$$

where ρ_f and η_f are density and viscosity of the fluid, respectively. Fluid flow is of Poiseuille type whenever viscous skin depth is larger than the size of the pores. Skin depth determines the definition of the low and high frequency ranges. The distinction between low and high frequencies is dependent on whether the viscous skin depth is large or small relative to the size of the pores. The two fluid flow situations are illustrated in Figure 2.5.

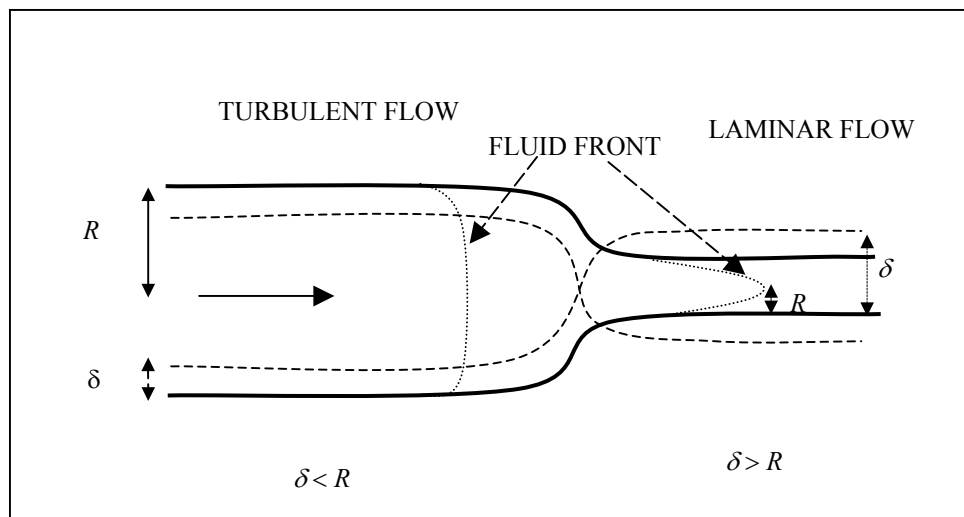


Figure 2.5: Illustration of the two different cases of fluid flow. R is the pore radius.

Due to the dependence of the viscous skin depth on frequency, high frequencies result in a low value of skin depth and the pore fluid-motion lags behind the motions of the solid part, corresponding to the inertia of the pore fluid. For low

frequencies, the skin depth is larger and the pore fluid motion is almost in phase with the solid part.

Following Johnson et al. (1987) the transition frequency is expressed by the oscillating flow change character

$$\begin{aligned} f_{c1} &= \frac{\phi \eta_f}{2\pi a_{21} \rho_f \kappa_1}, \\ f_{c3} &= \frac{\phi \eta_f}{2\pi a_{23} \rho_f \kappa_3}, \end{aligned} \quad (2.26)$$

where f_{c1} and f_{c3} are critical frequencies related to the sand and clay matrix, respectively.

The friction functions b_{ii} in the three-phase model [Appendix A (A-23)] describe the viscous damping due to the relative motion between the solids (sand/clay) and the fluid. By implementing the viscoelastic operator (or viscoelastic function) in the theory, the friction functions are replaced by

$$b_{ii} = \frac{\eta_f \phi^2}{\kappa_i} F_i(\omega), \quad i = 1, 3, \quad (2.27)$$

where F_1 and F_3 are viscodynamic functions, corresponding to the interaction between the sand and clay matrices with the fluid, respectively (Biot, 1962). Johnson et al. (1987) obtained the viscodynamic function F_i by introducing a dynamic tortuosity, which provides a good description of both the magnitude and phase of the dynamic tortuosity. Thus, substituting this tortuosity yields

$$a_{2i} \rightarrow a_{2i} + ix_i F_i(\omega), \quad (2.29)$$

where a_{2i} is the static tortuosity. The viscodynamic function is of the form

$$F_i(\omega) = \sqrt{1 - \frac{4ia_{2i}\kappa_i}{x_i\Lambda_i^2\phi}} \quad (2.30)$$

with

$$x_i = \frac{\eta_f \phi}{\omega \kappa_i \rho_f}, \quad (2.31)$$

where the quantities a_{2i} , κ_i , and Λ_i are related by

$$\frac{\xi_i a_{2i} \kappa_i}{\phi \Lambda_i^2} = 1. \tag{2.32}$$

ξ_i describes the shape of the pore network and is equal to 12 for a set of canted slabs of fluids, and is equal to 8 for a set of non-intersecting canted tubes. Λ_i is a geometrical parameter with $2/\Lambda_i$ being the surface-to-pore volume ratio of the pore-solid interface. In this study, $\xi_i = 8$ was used.

Figure 2.6a shows a viscodynamic F versus frequency plot with real and imaginary parts and with different values of ξ ($\xi = \xi_1 = \xi_3$) corresponding to the different shapes of the pore network. At low frequencies, the real part of viscodynamic F is equal to one, while the imaginary part of F is zero, i.e. F has no effect on friction term b_{ij} at low frequencies, but becomes significant at the high frequencies. Figure 2.6b shows the viscodynamic effect on attenuation of wave propagation for the whole range of frequencies for two different cases; $\xi = 8$ and $\xi = 12$. Here, a clean sandstone model ($C = 0$) is considered, where the other properties are the same as the example in section (2.5).

The physical interpretation of the viscodynamic operator is that it describes the induced pore pressure gradient when a fluid flow is imposed on the porous rock, and it gives a better physical description of the frequency-dependent energy dissipation.

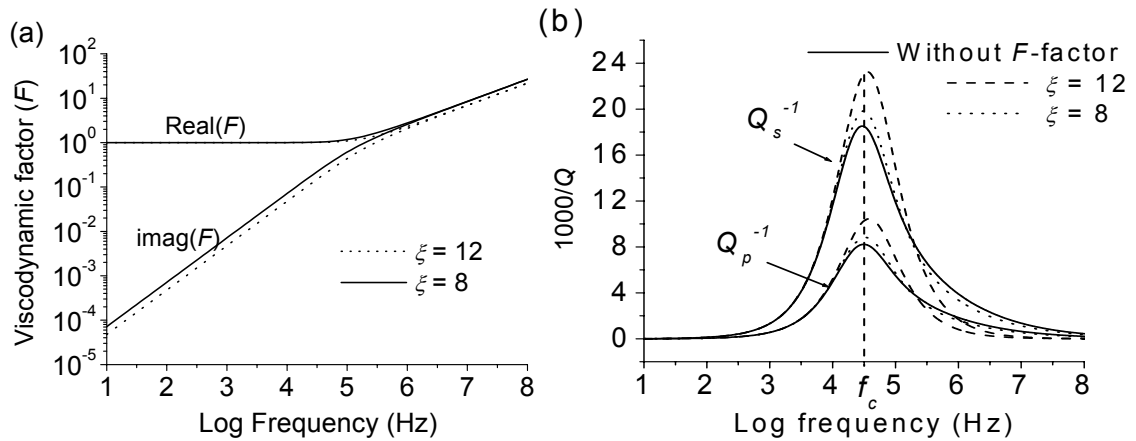


Figure 2.6: The viscodynamic operators as a function of frequency (a) and attenuation versus frequency with different values of viscodynamic factor (b).

2.5 Case study

To illustrate the behaviour of the wave velocities and attenuation versus frequency and clay content, and to study the effect of permeability on the wave responses, the following example is given. A water-saturated shaley sandstone with porosity $\phi = 0.25$ was used. Table 2.3 shows the properties of the different constituents. The other quantities are; empirical parameters of dry-rock moduli, $A = 2$ and $a = 0.5$ (the same values used in Carcione et al., 2000), and permeability model parameter B , equal to 15 in keeping with the calibration of permeability model with the experiments of Klimentos et al. (1990).

Figures 2.7 show the phase velocities (a) and attenuations (b) of three compressional waves (P-waves) and two shear waves (S-waves) at low frequency (30 Hz). Figures 2.7c and 2.7d show the same at high frequency (1 MHz). At the low frequency, the velocities of two P-slow waves (P2 and P3) and one S-slow wave (S2) are zero and are high in attenuation. This observation is in good agreement with the physical theory. At the low frequency, there is no dynamic interaction between solid parts and fluid part. The wave motions of all parts (sand, clay, and fluid) move in the same phase in porous media, as in Gassmann's theory, where no slow waves are induced. On the other hand, at the high frequency, the fluid is in an unrelaxed state and does not move in phase with the solid parts. This different movement of solids and fluid induces slow waves. This phenomenon is characteristic of Biot's theory.

Solid grain	bulk modulus, K_s	39 Gpa
	shear modulus, μ_s	39 Gpa
	density, ρ_s	2650 kg/m ³
	average radius, R_s	50 μ m
Clay	bulk modulus, K_c	20 GPa
	shear modulus, μ_c	10 GPa
	density, ρ_c	2650 kg/m ³
	average radius, R_c	1 μ m
Fluids	bulk modulus, K_w	2.4 GPa
	density, ρ_w	1000 kg/m ³
	viscosity η_w	1.798 cP

Table 2.3: Material properties of the clay-bearing sandstone (Carcione et al., 2000).

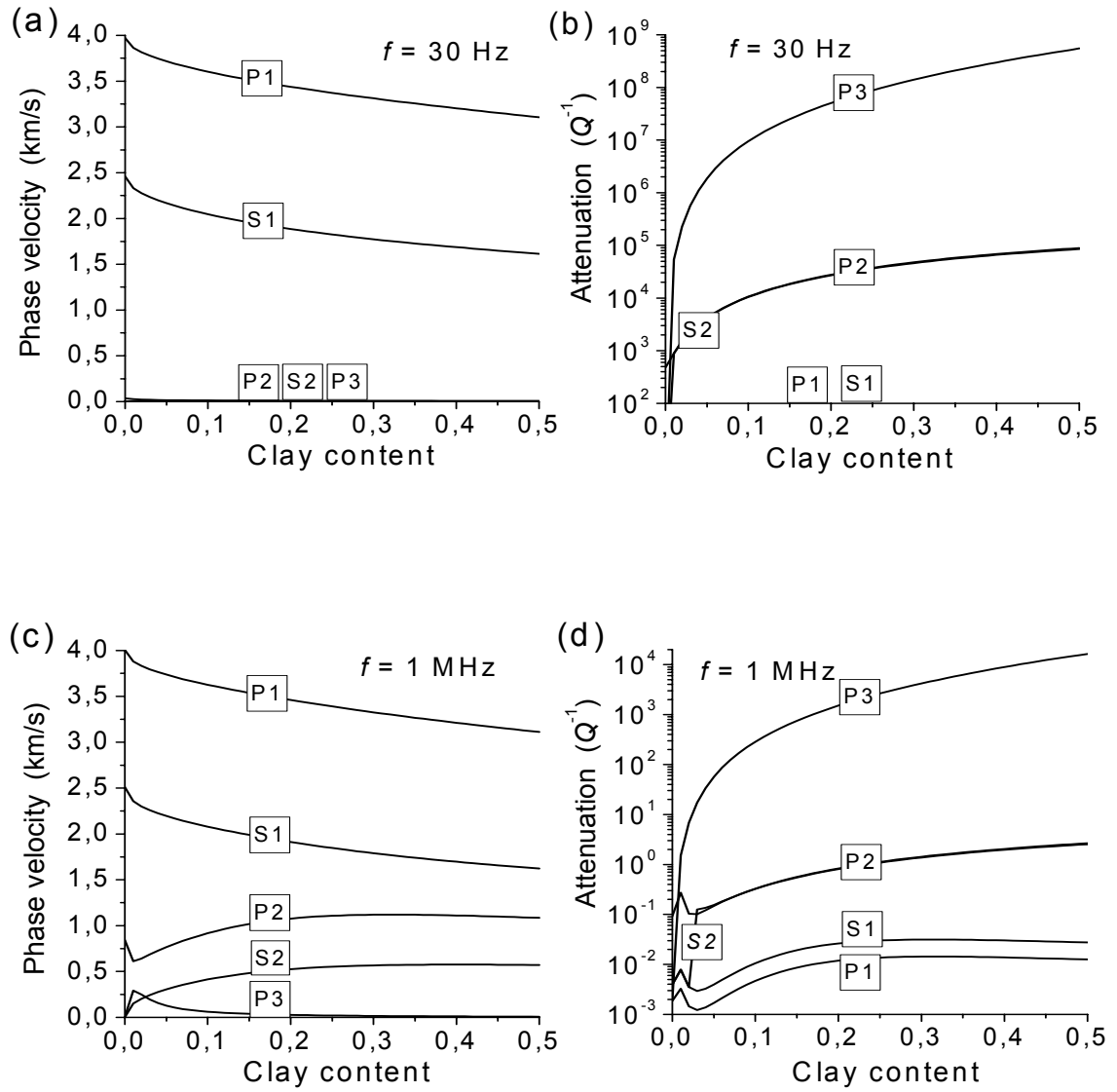


Figure 2.7: The phase velocities (a) and the attenuation (b) of different wave modes as the function of clay content at $f = 30$ Hz. Similarly, (c) and (d), but at $f = 1$ MHz.

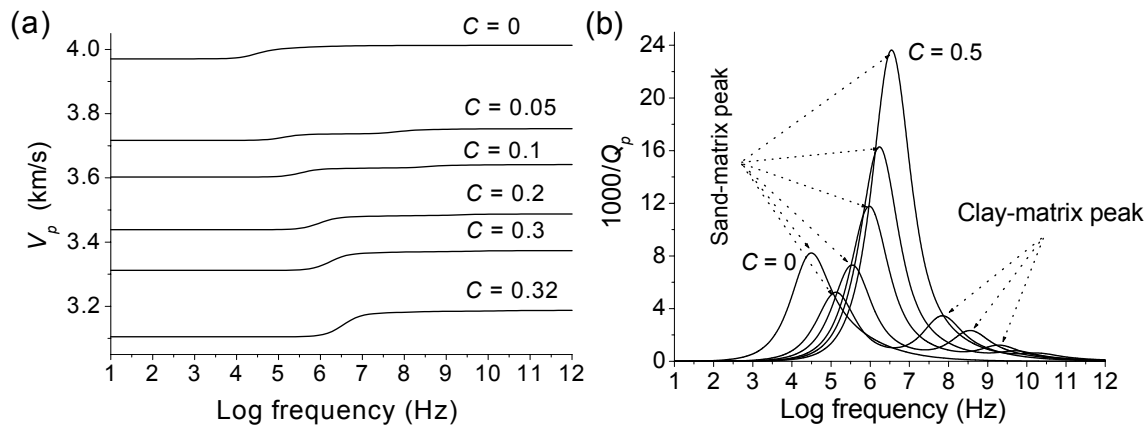


Figure 2.8: P-wave velocity (a) and its attenuation (b) versus frequency with different clay content.

Figures 2.8a and 2.8b show P-wave velocity (fast P-wave) and attenuation versus frequency and clay content. The velocity has a transition zone and attenuation has a peak (Biot peak or relaxation peak) at critical frequency f_c , which separates relaxed state and unrelaxed state of fluid. The unrelaxed state of fluid induces stiffening of the pore material, thus giving a higher velocity, while a lower velocity range relates to the relaxation state of fluid. When clay is present in sandstones, there are two transition velocity zones and two Biot peaks of attenuation, one at critical frequency f_{c1} , corresponding to sand matrix with fluid content, and another at f_{c3} , corresponding to clay matrix with fluid content. The critical frequencies f_{ci} move to higher frequencies with increasing clay content.

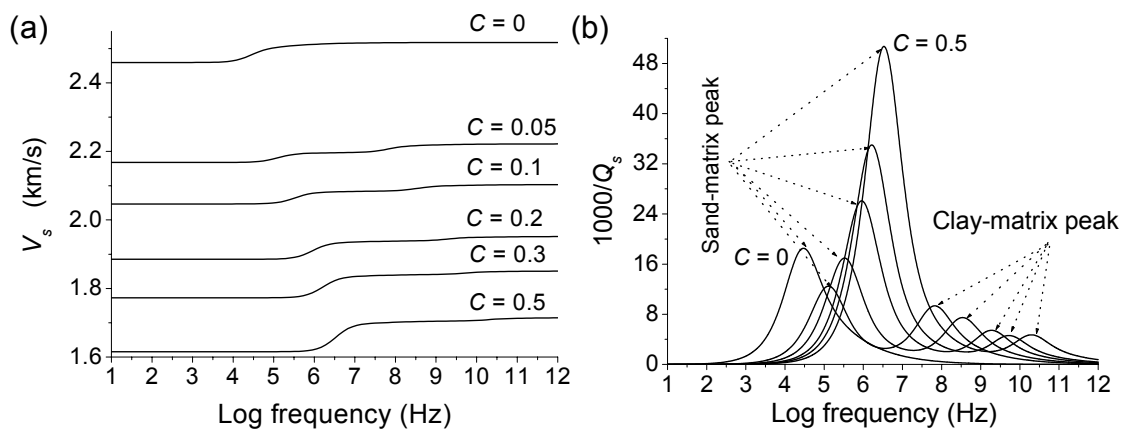


Figure 2.9: S-wave velocity (a) and its attenuation (b) versus frequency with different clay content.

This phenomenon is in good agreement with the physical theory that increasing clay content contributes to decreased permeability, and then more energy (i.e. higher frequency) is required to approach an unrelaxed state. Increased clay content increases the value of the Biot peak and transition zone of the sand matrix. This is due to a smaller stiffness in the sand matrix. Figures 2.9a and 2.9b show S-wave velocity (fast S-wave) and its attenuation versus frequency and different clay content, which show the same behaviour as in the P-wave.

2.6 Summary

In this section, the three-phase Biot-type theory applied for shaley sandstones has been presented. In addition, the Biot dynamic effect has been improved by including some physical effects. i.e. 1) an empirical permeability model depend on porosity and clay content and based on theory and experimental data and 2) viscodynamic effects of the fluid in the natural rocks at a high frequency range when the fluid motion behaviour is no longer laminar.

The three-phase Biot-type theory illustrates that three P-waves (one fast and two slow) and two shear waves (one fast and one slow) can be obtained. The shaley sandstone model characteristics show two attenuation peaks (Biot peaks) at different frequencies, corresponding to fluid in the sand matrix, and fluid in the clay matrix. At low frequencies, the fluid has enough time to achieve pressure equilibration (relaxed regime), therefore, there is no conversion from fast waves to slow waves, i.e. neither slow P- nor slow S-waves exist (Figure 2.7a and 2.7b). On the other hand, at high frequencies (from sonic to ultrasonic), the fluid cannot relax. This unrelaxed state induces the energy loss of the primary waves, i.e. the conversion from fast waves to slow waves (Figure 2.7c and 2.7d). The slow waves, however, are small in amplitude compared to fast waves. In the petroleum industry, the application of the waves is normally focused on fast P-waves and fast S-waves, and the slow waves are regarded as noise or energy loss.

Chapter 3

Viscoelastic effects

3.1 Introduction

Biot's theory of dynamic poro-elasticity (Biot, 1962) successfully described wave propagation properties of synthetic porous media such as sintered glass beads. In natural porous media such as sandstone, Biot's effect alone is not enough to describe the dissipation of the rock. The discrepancies between Biot's theory and actual measurements are due to complex pore shapes, i.e. the microstructure. This complexity gives rise to a variety of different mechanics, which contribute to attenuation of different wave modes. Such rocks are called inelastic or viscoelastic.

The inelasticity of rocks usually depends on a large number of physical mechanisms, which can be modelled by different micro-structural theories. These effects include local fluid movements (squirt flow), intergranular friction, capillary forces, and thermal effects. A general way to include all these mechanisms is to use phenomenological models to describe the rheology of the medium.

Several models have been developed to describe various attenuation phenomena. It is customary to represent viscoelastic loss mechanisms by combinations of springs and dashpots. The Maxwell model is modelled with a spring, and a dashpot in series, and the Kelvin-Voigt model with a dashpot and spring in parallel. A series combination of a spring and a Kelvin-Voigt model gives a more realistic representation of viscoelastic materials. The resulting system is called the Zener model (Zener, 1948) or standard linear-solid. This model is characterised by a single relaxation peak at resonance frequency and is represented in Figure 3.1. The stress-strain relation of the spring is ideally elastic (no energy loss) following Hook's law: $\sigma = k\varepsilon$, where k is the elastic modulus of the spring. The dashpot represents the inelastic part with $\sigma = \eta\varepsilon$, where η is the viscosity.

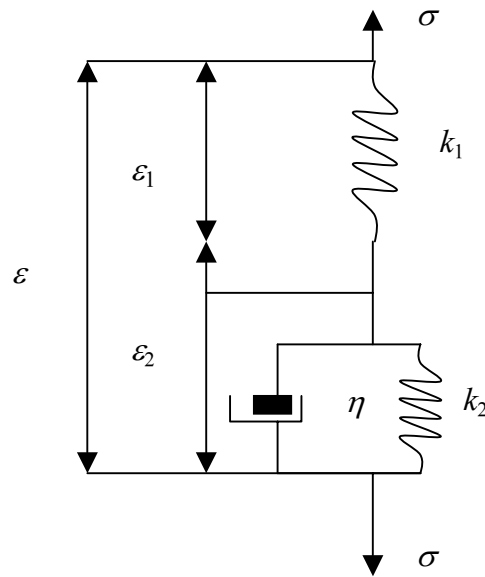


Figure 3.1: Schematic of a spring and dashpot system whose force displacement relation is described by the same equation as the standard linear-solid (Zener typer).

In natural rocks, the microscopic heterogeneity of the porous medium induces a complex macroscopic physical behaviour sensitive to slight variations in fluid content or of the solid structure and the shape of the pores. Beside Biot's theory (global flow), the squirt flow mechanism (local flow) is also one of the most important dissipation mechanisms at sonic and ultrasonic frequencies. It explains the energy losses due to interactions between fluid and solid components at the level of microstructure. Pointer et al. (2000) describe three distinct mechanisms of wave-induced fluid flow (see also Hudson et al., 1996); flow between cracks, flow within cracks, and diffusion from cracks to the background porous medium. These mechanisms can be incorporated into the present theory by using Zener models of attenuation. Stoll and Bryan (1970) show that attenuation is controlled by the inelasticity of the skeleton (friction at grain contacts) and by viscodynamic mechanisms. The latter involve local (squirt) flow and global (Biot) flow. Global flow is implicit in Biot's theory and squirt flow is modelled by using a single relaxation mechanism based on the Zener model (Bourbié et al., 1987, p. 227; Dvorkin et al., 1994; Carcione, 1998). In the present study, the squirt flow mechanism is implemented into the three-phase Biot-type model by substituting the fluid-solid coupling modulus with a time-dependent relaxation function, using a single relaxation mechanism, based on the Zener model, Pham et al., 2002c).

Apart from the squirt flow mechanism, the complexity of natural rocks induces other dissipation mechanisms at different frequencies including inter-granular friction and thermal effects. Experimental results (e.g. Murphy 1982) have shown that the quality factor remains constant, i.e. there is continuous dissipation over

wide frequency ranges. Spencer et al. (1982) shows strong non-constant Q . Kjartansson (1979) considered a model with constant quality factor, Q , strictly independent of frequency. The constant- Q model is very simple mathematically, and is completely specified by two parameters, a reference frequency ω_0 and quality factor Q_0 . Recently, Ursin and Toverud (2002) studied the seismic dispersion and attenuation by comparing algebraically and numerically eight different viscoelastic models; the power-law model, Kjartansson's model, standard linear-solid model and others. The result shows that all models except the standard linear-solid model behave similarly in the seismic frequency range.

In this study, in addition to the applied Zener model for squirt flow phenomenon, the constant- Q model applied for dry-rock moduli is also included in the theory (Pham et al., 2002c). The bulk of the remaining dissipation mechanisms, such as inter-granular friction and thermal losses, is modelled using the constant- Q model. It is assumed that the lower the frame modulus is, the lower the quality factor is (i.e. the higher the attenuation). Using this property a Q -factor is assigned to the sandstone bulk modulus, and the Q -factor associated to the shear modulus is obtained.

3.2 Viscoelastic concept

Viscoelastic behaviour is a time-dependent, mechanically non-instantaneous response of a material body to variations in applied stress deformation. Because the response is not instantaneous, the behaviour of the material is characterised by a time-dependent function. One can say that the material has memory. For a linear viscoelastic material the stress-strain relation can be described by

$$\sigma = \psi * \dot{\varepsilon} \quad (3.1)$$

or

$$\varepsilon = \chi * \dot{\sigma}, \quad (3.2)$$

where σ is the stress, ε is the strain and ψ and χ are the relaxation and creep functions, respectively. The symbol '*' denotes time convolution and the dot represents time differentiation. Transforming equations (3.1) and (3.2) to the frequency-domain yields

$$\tilde{\sigma} = M \tilde{\varepsilon} \quad \text{and} \quad \tilde{\varepsilon} = J \tilde{\sigma}. \quad (3.3)$$

The complex modulus and complex creep compliance, are given by

$$\begin{aligned}
M(\omega) &= \int_{-\infty}^{+\infty} \dot{\psi}(t) e^{-i\omega t} dt, \\
J(\omega) &= \int_{-\infty}^{+\infty} \dot{\chi}(t) e^{-i\omega t} dt,
\end{aligned}
\tag{3.4}$$

where ω is the angular frequency and t is the time variable. The inelastic effects are quantified by the quality factor and the phase velocity dispersion. The lower the Q factor, the larger the dissipation and the quality factor is then defined as the peak potential energy density divided by the loss energy density, and is given by

$$Q(\omega) = \frac{M_r(\omega)}{M_i(\omega)},
\tag{3.5}$$

where indices r and i denote the real and imaginary parts, respectively.

3.3 Squirt flow and the Zener model

Viscoelasticity is introduced into Biot's poroelastic equations for modelling a variety of dissipation mechanisms related to skeleton-fluid interaction. One of these mechanisms is the squirt-flow, by which a force applied to the area of contact between two grains produces a displacement of the surrounding fluid in and out of this area. Since the fluid is viscous, the motion is not instantaneous and energy dissipation occurs.

As in Carcione (1998), we have modelled the squirt flow mechanisms with a single relaxation peak based on the Zener mechanical model (Pham et al., 2002c). The generalisation of the coupling modulus M in Carcione (1998) is K_{av} in the present theory, where K_{av} is defined as the average modulus (see Appendix A). The relaxation is expressed as

$$\psi(t) = K_{av} (1 + \varphi)^{-1} \left[1 + \varphi e^{\left(\frac{-t}{\tau_\sigma}\right)} \right] H(t),
\tag{3.6}$$

where $H(t)$ denotes the Heaviside function, $\varphi = \tau_\varepsilon / \tau_\sigma - 1$, and where τ_ε and τ_σ denotes relaxation times of strain and stress, respectively.

Calculation of the phase velocity and the attenuation factor requires a Fourier transformation of the constitutive equations to the frequency domain, implying the following substitution,

$$K_{av} \rightarrow K_{av} (1 + \varphi)^{-1} \frac{1 + i\omega\tau_\varepsilon}{1 + i\omega\tau_\sigma}, \quad (3.7)$$

where the relaxation times, τ_ε and τ_σ can be expressed in terms of a Q -factor, Q_{0sq} , and a reference frequency, f_{0sq} , as

$$\tau_\varepsilon = \frac{1}{2\pi f_{0sq} Q_{0sq}} \left[\sqrt{Q_{0sq}^2 + 1} + 1 \right] \quad (3.8)$$

and

$$\tau_\sigma = \frac{1}{2\pi f_{0sq} Q_{0sq}} \left[\sqrt{Q_{0sq}^2 + 1} - 1 \right]. \quad (3.9)$$

Note that we do not introduce the squirt flow effect on the coupling modulus between clay and fluid since this is a case of shaley sandstone with primarily sand matrix. Moreover, it is assumed that the dynamic effect in the clay matrix is small due to the extremely small pores (clay particle radius, $R_c \approx 1\mu\text{m}$).

3.4 Constant- Q model

The constant- Q model is introduced into the theory for modelling the rest of mechanisms such as intergranular friction, thermal effect and others. Here the constant- Q model is implemented by making the frame bulk and shear moduli of sandstone viscoelastic.

The constant- Q model is based on a creep function of the form $t^{2\gamma}$ where $\gamma \ll 1$ for seismic applications. This model provides a simple parameterisation of seismic attenuation in rocks for use in oil exploration and in seismology. By reducing the number of parameters, it allows an improvement of seismic inversion. Moreover, there is physical evidence that attenuation is almost linear (i.e. Q is constant) with frequency in many frequency bands. Bland (1960) and Kjartansson (1979) discuss a linear attenuation model with the required characteristics. Keller (1989) has used the constant- Q theory to model frame inelasticity in Biot's theory for isotropic saturated media. He obtained a good fit of experimental P-wave attenuation and velocity of sediments.

The relaxation function is expressed as

$$\psi(t) = \frac{M_0}{\Gamma(1-2\gamma)} \left(\frac{t}{t_0} \right)^{2\gamma} H(t), \quad (3.10)$$

where M_0 is a bulk modulus at a reference time, t_0 , Γ is Euler's Gamma function. From equations (3.4), (3.10) and after some calculations, the complex modulus is obtained

$$M(\omega, Q) = M_0 \left(\frac{i\omega}{\omega_0} \right)^{2\gamma} = M_0 \left| \frac{\omega}{\omega_0} \right|^{2\gamma} e^{i\pi\gamma}, \quad (3.11)$$

where ω_0 is reference angular frequency and where $\pi\gamma$ is the phase angle between the stress and strain. Therefore, with Q determined by the ratio of real to imaginary parts of the complex moduli (equation 3.5), the relation between the stress/strain phase shift parameter, γ , and quality factor, Q , is obtained,

$$\gamma = \frac{1}{\pi} \tan^{-1} \left(\frac{1}{Q} \right). \quad (3.12)$$

In equation (3.12), it is observed that $Q > 0$ is equivalent to $0 < \gamma < 1/2$. Attenuation is modelled by making the frame (i.e. sandstone skeleton) bulk and shear moduli viscoelastic,

$$\begin{aligned} K_{sm} &\rightarrow K_{sm} \left(\frac{i\omega}{\omega_0} \right)^{2\gamma_K}, \\ \gamma_K &= \frac{1}{\pi} \tan^{-1} \left(\frac{1}{Q_K} \right), \end{aligned} \quad (3.13)$$

where K_{sm} is frame (dry) bulk modulus of sandstone which can be obtained from the (modified) expression of Krief et al. (1990) (eq. 2.5), and Q_K is the quality factor corresponding to the moduli of the sandstone skeleton. The lower the frame modulus (lower velocity) is, the lower is its Q -factor (i.e. the higher the attenuation) (e.g., Toksöz and Johnston, 1979; Pham et al. 2002a; see also eq. 3.5). Based on this fact, Q_K is defined following (Pham et al., 2002c)

$$Q_K = \frac{K_{sm}}{K_{sm0}} Q_0. \quad (3.14)$$

Here, Q_0 is the given loss parameter for the sand skeleton which can be obtained from laboratory measurement, and $K_{sm0} = K_{sm}$ for a reference rock with porosity ϕ_0 and clay content C_0 at the given pressure condition.

A similar relation is used for the shear modulus:

$$\begin{aligned}\mu_{sm} &\rightarrow \mu_{sm} \left(\frac{i\omega}{\omega_0} \right)^{2\gamma_\mu}, \\ \gamma_\mu &= \frac{1}{\pi} \tan^{-1} \left(\frac{1}{Q_\mu} \right),\end{aligned}\tag{3.15}$$

where μ_{sm} is frame shear modulus of sandstone can be obtained from equation (2.5). The corresponding Q_μ -factor for the shear modulus is given by

$$Q_\mu = \frac{\mu_{sm}}{K_{sm}} Q_K.\tag{3.16}$$

Note that we do not introduce the visco-elastic effect on the clay frame modulus, since this is a case of shaley sandstone with a primarily sand matrix.

3.5 Discussions

The limitation of the constant- Q model is that velocities go to infinity when frequencies go to infinity. This is physically not possible. All the frequencies of interest, therefore, must satisfy the condition:

$$\frac{1}{\pi Q} \ln \left| \frac{\omega}{\omega_0} \right| \ll 1.\tag{3.17}$$

To satisfy this condition, the highest value of the frequency range of interest should be used as the reference frequency. In the present study, the reference frequency of $f_0 = 1$ MHz was used in order to describe the viscoelastic effect in the frequency range of interest, i.e. from seismic frequency (10 Hz) to ultrasonic frequency (1 MHz).

Due to the complexity of natural rocks, there are several attenuation mechanisms present when the waves pass through porous media (e.g. squirt flow, intergranular friction, and thermal effect). Using the Zener solid model and the constant- Q model to address these behaviours gives a synthetic model that can describe the viscoelastic effects in natural rocks from low to high frequencies. The limitations of the model are mainly with regard to the use of the constant Q -model to describe attenuation mechanisms, which are not of viscodynamic nature. However, this limitation is a consequence of the absence of experimental data in the sonic and seismic bands. The constant- Q model could be substituted by a generalised Zener model (parallel or series connection of Zener elements), which can be used to fit a general functional behaviour of quality factor (and velocity dispersion). In this sense, the model is not a predicting tool. More details of the visco-elasticity will be discussed in chapter 4.

It is noted that losses due to scattering are not described by the present model, which is based on an effective-medium theory (i.e. the wavelength of the signal is much larger than the pore size). However, when laboratory measurements and sonic logs are used to infer the behaviour of acoustic properties at seismic frequencies, the frequency dependence of this property is a key factor. As demonstrated by White (1975), wave velocity and attenuation are substantially affected by the presence of partial (patchy) saturation, mainly depending on the size of the gas pockets (saturation), frequency and permeability. These effects are implicitly described by Biot-type theories, when using full-wave modelling codes to obtain synthetic seismograms in inhomogeneous media (chapter 6, 7).

The ideal model application is that laboratory measurements and sonic logs can be used to infer the behaviour of acoustic properties at seismic frequencies. The demonstration of visco-poroelasticity is presented in the next chapter, where the partial saturation effect is also considered.

Chapter 4

Partial saturation

4.1 Introduction

In porous media where both gas and liquid phases exist, the effect of partial saturation on velocity and attenuation depends on the frequency range. At low frequencies (seismic frequencies), the wave sees the medium as a fine-scale distribution of saturation, hence, the different wave-induced increments of pore pressure in each phase have time to diffuse and equilibrate. This is an iso-stress situation, and therefore the effective bulk modulus of the mixture of fluids is described well by the lower bound [Wood's average (Wood, 1955); Reuss's average (Reuss, 1929); Gassmann (Gassmann, 1951); Mavko and Mukerji (1998)]. On the other hand, at high frequencies (ultrasonic frequency), the differences in wave-induced pore pressure do not have time to flow and equilibrate among the various phases, and this state of unrelaxation induces a stiffening of the pore material, which increases the wave velocity considerably (Cadoret et al. 1995). In this case, Wood's model is not appropriate and, in general, a Hill's average is used to model the wave velocities at ultrasonic frequencies (laboratory frequencies). Alternatively, an approximation model of this case is the upper bound [Voigt's average (Voigt, 1928)].

Several investigations have been made to study the different effects on wave velocities and attenuation in partially saturated rocks. Murphy (1982) and Murphy et al. (1986) measured the acoustic wave velocities and attenuation in the sonic frequency band (1-10 kHz). Mavko and Mukerji (1998) studied the bounds on low-frequency seismic velocities in partially saturated rocks. The experimental results of Yin et al. (1992) display consistent peaks in resonance attenuation at high water saturation. A strong dependence on the saturation history is evident, with the attenuation peak located at 90 % water saturation in the drainage experiment, and 98 % during imbibition. King et al. (2000) measured

compressional and shear wave velocities at the ultrasonic frequency. For modelling, Brie et al. (1995) suggested an empirical model for the mixture of fluids. No micro-structural theory, however, is able to predict the behaviour at intermediate frequencies. However, in the present study, an empirical model for a partially saturated medium was derived. The model, which may be applied for all frequency ranges, is based on both physical theory and experimental data.

The approach to modelling the mixture of fluids in partially saturated rocks is to replace the collection of phases with a simple effective fluid. Here, the following mixing laws were applied to obtain the effective medium (Pham et al., 2002c): i) a modified empirical model for fluid bulk moduli of the mixture proposed by Brie et al. (1995), which gives the Wood modulus at low frequencies and the Voigt modulus at high frequencies, ii) viscosity of the mixture by Teja and Rice (1981a,b), iii) relative permeabilities of the mixture provided by Van Genuchten (1978), and iv) the density of the mixture estimated as the linear average of the phase densities.

4.2 Relative permeability

In a single-phase saturated medium, the (absolute) permeability does not depend on the fluid type and can be obtained by using Kozeny-Carman relation (see section 2.3). In multi-phase fluid medium, the different flowing capacities of the fluids interact with each other and induce a fluid-dependent flow. The relative permeabilities, which depend on the type of fluids and the fluid distribution are, therefore, defined to describe the different movements of the fluids in a partially saturated medium.

Relative permeability is defined as the ratio of the effective permeability of a given fluid at a fixed saturation to the permeability at 100% saturation (absolute permeability). Relative permeability depends on pore size distribution, fluid type, saturation history (drainage or imbibition), and saturation. Van Genuchten (1978) has derived an empirical relative permeability model as function of saturation,

$$K_{rw} = \sqrt{S_{we}} [1 - (1 - S_{we}^{1/m_w})^{m_w}]^2, \quad (4.1)$$

$$K_{rg} = \sqrt{S_{ge}} [1 - (1 - S_{ge}^{1/m_g})^{m_g}]^2 \quad (4.2)$$

and

$$S_{we} = \frac{S_w - S_{wi}}{1 - S_{wi}}, \quad S_{ge} = \frac{S_g - S_{gi}}{1 - S_{gi}}, \quad (4.3)$$

where S_{wi} and S_{gi} are irreducible water saturation and trapped gas, respectively (Bear and Bachmat, 1990, p. 344). m_w and m_g are free factors for water and gas. These free factors depend on the fluid type, saturation history, and geological properties of the rocks, which can be obtained by fitting to laboratory measurements.

Relative permeabilities were obtained from equations (4.1) and (4.2) where $S_{wi} = 0.2$, $S_{gi} = 0.1$, and the free parameters, $m_w = 1.1$, $m_g = 1.5$ were estimated by fitting the model to experimental data from a North Sea reservoir (Figure 4.1). Both permeabilities decrease for decreasing saturation of the corresponding fluid. In particular, there is practically no water flow below 20 % water saturation. This phenomenon is due to gas bubbles in the pores preventing water flow.

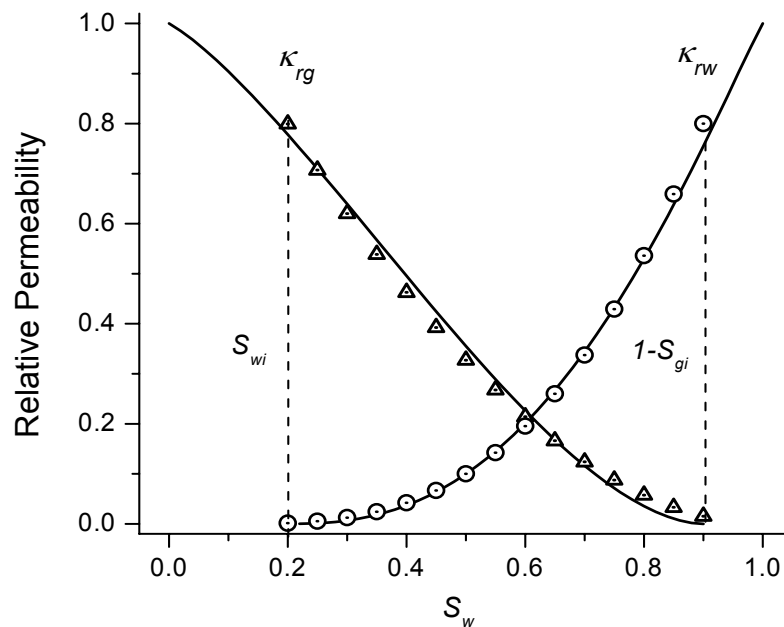


Figure 4.1: Fitted curves of relative permeabilities using data from a North Sea reservoir.

4.3 Mixing laws for multi-fluid model

For the permeability of the mixture, a simple weighted average was used to introduce effective permeability of the mixture including relative permeabilities of the fluids,

$$\kappa_e = \kappa(\kappa_{rw}S_w + \kappa_{rg}(S_w - 1)), \quad (4.4)$$

where κ is the (absolute) permeability and κ_e is the effective permeability of the gas/water mixture.

For the viscosity of the mixture, the method of Teja and Rice (1981a,b) was applied,

$$\eta_f = \eta_g \left(\frac{\eta_w}{\eta_g} \right)^{S_w}, \quad (4.5)$$

where η_w and η_g are viscosities of water and gas, respectively. Following Teja and Rice (1981a,b) the empirical relation for the viscosity of the mixture (eq. 4.5) is a good approximation for most values of the saturations. Figure 4.2 shows the comparison of this equation (solid line) to the linear law $\eta = S_w\eta_w + S_g\eta_g$ (dashed line). The linear relationship overestimates the viscosity of the mixture.

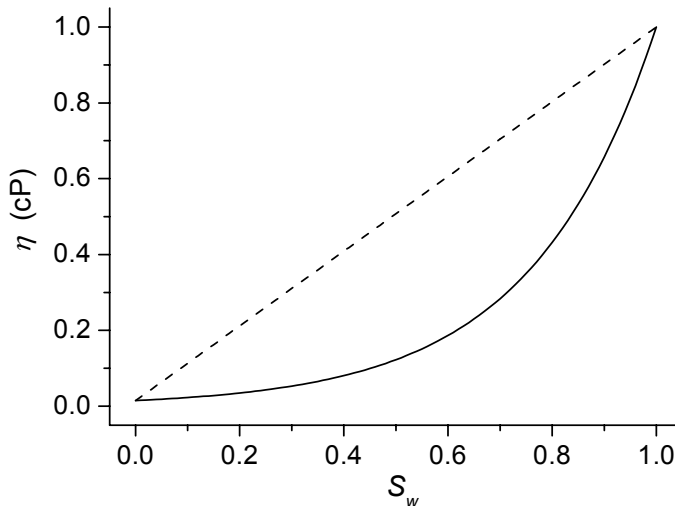


Figure 4.2: Viscosities as a function of water saturation, where the dashed line shows the linear mixing law and the solid line shows the mixing law of Teja and Rice (1981a,b).

The density of the mixture is estimated as a linear average of the phase densities (e.g., Carcione and Gangi 2000a,b),

$$\rho_f = \rho_w S_w + \rho_g S_g, \quad (4.6)$$

where ρ_w , and ρ_g are the densities of water and gas, respectively.

The effect of partial saturation (gas/fluid) on the compressibility of fluids depends on the frequencies. At low frequencies (long wavelength), the fluid phases are mixed at fine scales compared to the size of the wavelength. These pore pressure increments can equilibrate with each other to a single average value. This is an iso-stress situation, and hence the effective bulk modulus of the mixture of fluids is described well by Wood's average (Wood, 1955),

$$\frac{1}{K_f} = \frac{S_w}{K_w} + \frac{S_g}{K_g}. \quad (4.7)$$

At high frequencies (short wavelength), the wave sees the fluids of the mixture as a coarse scale mixture. In this case, these pore pressure increments cannot equilibrate with each other and thus induce a stiff modulus. This is a 'patchy' situation, and therefore the effective bulk modulus of the fluid mixture with partially varying bulk modulus but uniform shear modulus is described exactly by Hill (1963). Hill shows that when all of the phases or constituents in a composite have the same shear modulus, μ , the effective P-wave modulus, $M = K + 4/3\mu$ is given by

$$\frac{1}{K + \frac{4}{3}\mu} = \frac{S_w}{K_{sat-w} + \frac{4}{3}\mu} + \frac{S_g}{K_{sat-g} + \frac{4}{3}\mu}, \quad (4.8)$$

where K_{sat-w} and K_{sat-g} are effective bulk moduli, saturated with 100 % water and gas, respectively. By extension of equation (4.8), the P-wave velocity is expressed as

$$\frac{1}{(\rho V_P^2)} = \frac{S_w}{(\rho V_P^2)_{sat-w}} + \frac{S_g}{(\rho V_P^2)_{sat-g}}, \quad (4.9)$$

where the P-wave velocity is given by $V_P = (M/\rho)^{1/2}$. It can be shown, however, that an approximation to 'patchy' saturation upper bound can be found by Voigt's (1928) average of the fluid modulus,

$$K_f = K_w S_w + K_g S_g. \quad (4.10)$$

In attempting to introduce the empirical mixing law to obtain a better fit with laboratory measurements and field observations, we modified the model of Brie et al. (1995),

$$K_f = (K_w - K_g)S_g^e + K_g, \quad (4.11)$$

where $e = (f_{0B}/f)^{0.34}$ is an empirical parameter, with f_{0B} being a reference frequency. In this study, f_{0B} was set equal to 1 MHz and the exponent 0.34 fits data from seismic to the ultrasonic band. In particular, in the sonic band the value is approximately [2-5] (Brie et al., 1995). Equation (4.11) gives Voigt's mixing law for $e = 1$ and approximation of Wood's average for $e = 40$. The use of the modified model of Brie et al., although empirical, allows us to model wave velocities and attenuation in the whole frequency range.

Figure 4.3 shows the bulk modulus of the water/gas mixture versus water saturation (a) and frequency (b) based on equation (4.11). The modified model of Brie et al. is in good agreement with the Voigt's and Wood's bounds (upper and lower bounds).

4.4 Case study

Berea sandstone saturated with water and gas is considered. Table 4 shows the properties of the different constituents. The porosity is $\phi = 0.246$ (King et al., 2000). The other quantities are; the empirical parameters for dry-rock moduli (eq. 2.5) $A = 2.8$, $F_\mu = 1$; the percolation porosity, $\phi_p = 0.035$; the geometrical factor in Kozeny-Carman equation, $B = 15$ (section 2.3); $\xi_1 = \xi_3 = 8$ describing the shape of the pore network implied in the viscodynamic operator (section 2.4); the viscoelastic parameters in Kjartansson's equation $Q_0 = 60$ and $\omega_0 = 2\pi$ MHz (section 3.4). For partial saturation, the centre of the peak, used for squirt-flow modelling (section 3.3), is given by

$$f_{0sq} = f_{0sq}^{(\text{gas-filled})}(1 - S_w) + f_{0sq}^{(\text{water-filled})}S_w, \quad (4.12)$$

Following Dvorkin et al. (1994), we consider that, as the viscosity of the pore fluid decreases, the attenuation peak of squirt-flow mechanism shifts towards higher frequencies. We assume $f_{0sq} = 40$ kHz for gas filled rocks and $f_{0sq} = 3$ kHz for water filled rocks and Q_{0sq} equal to 10 for both fluids (see Carcione, 1998). There are, however, empirical constants f_{0sq} and Q_{0sq} can be obtained by fitting the Zener model to experimental data.

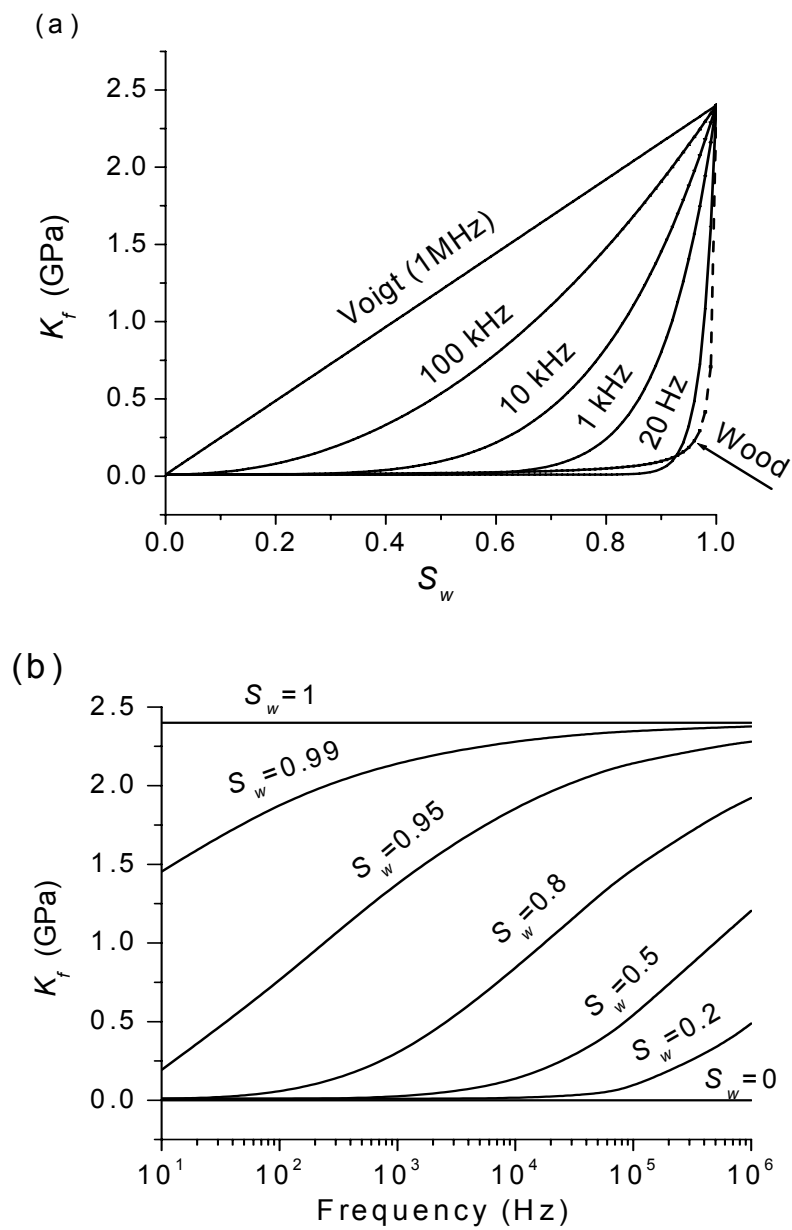


Figure 4.3: Bulk modulus of the water/gas mixture versus water saturation (a) and frequency (b).

Solid grain	bulk modulus, K_s	35 Gpa
	shear modulus, μ_s	35 Gpa
	density, ρ_s	2650 kg/m ³
	average radius, R_s	50 μ m
Clay	bulk modulus, K_c	20 GPa
	shear modulus, μ_c	10 GPa
	density, ρ_c	2650 kg/m ³
	average radius, R_c	1 μ m
Fluids	bulk modulus, K_w	2.4 GPa
	density, ρ_w	1030 kg/m ³
	viscosity, η_w	1.798 cP
	bulk modulus, K_g	0.01 GPa
	density, ρ_g	100 Kg/m ³
	viscosity, η_g	0.02 cP

Table 4: Material properties of the clay-bearing sandstone.

Figures 4.4a and 4.4b compare the P- and S-wave velocities, which are predicted by the model with experimental data obtained by King et al. (2000). The sharp drop in the velocities (King's data) is attributed to softening of cements (sometimes called chemical weakening), to clay swelling, and to surface effects when even a small amount of water is introduced. In (b), the velocities are represented for several frequencies, ranging from the seismic to the ultrasonic band. Also shown, is the P-wave velocity obtained by using Hill's equation (4.9).

Figure 4.5 shows a three-dimensional plot of P-wave velocity (a) and dissipation factor (attenuation) (b) versus frequencies and water saturation. The dissipation factor has a maximum value at the squirt-flow relaxation peak. A secondary maximum corresponds to the Biot peak. The losses at full water saturation are stronger than the losses at full gas saturation. The behaviour of attenuation agrees qualitatively with experimental data published by Yin et al. (1992). The relative permeability applied for the present model creates a slight shift in Biot peak towards higher frequency in partial saturation (see eq. 2.26). The critical (cross over) frequency for squirt flow decreases with increasing water saturation (increasing viscosity) which agrees with the relaxation function of squirt flow mechanism $\omega_c = K\alpha^3/\eta$ (Dvorkin et al., 1994; Batzle et al., 2001). Here K is frame modulus and α is crack aspect ratio. On the other hand, the critical frequency for Biot peak increases with increasing viscosity (see also eq. 2.26). However, for the magnitude of attenuation, the squirt-flow peak do not seem to show the decrease in attenuation at 100 % water saturation seen in Murphy (1982) and Yin et al. (1992). This affect is due to using the same value of Q_{0sq} for all saturation. The empirical parameter Q_{0sq} could be obtained by fitting the model with experimental data. However, the difficulty for analytical modelling is the lack of

micro-structure theory. In partial saturation, the heterogeneity of the fluids is the key factor for dissipation (see chapter 6, 7).

The S-wave velocity and S-wave dissipation factor as functions of saturation and frequency are shown in Figures 4.6a and 4.6b, respectively. The S-wave velocity increases with frequency and, generally, with decreasing water saturation. Attenuation has a maximum at approximately the location of the Biot peak and 100% water saturation. S-wave is unaffected by the squirt-flow mechanism.

Figure 4.7 shows the wave velocities (a) and dissipation factors (b) and (c) versus water saturation with different values of clay content C for a frequency of 10 kHz. The permeability corresponding to each value of C is indicated in the curves. In general, attenuation increases with increasing clay content. Following squirt flow theory the critical frequency should decrease with decreasing permeability. This effect is not observed in Figure 4.7, since we used a constant Q_{0sq} for Zener model.

Finally, the three-dimensional plots in Figures 4.8 and 4.9 show more clearly the effect of clay and saturation on the dissipation factors for the frequencies of 10 kHz (a), 100 kHz (b) and 1 MHz (c). In the sonic range (~ 10 kHz), it is observed that the Biot relaxation peak for high gas saturation and high clay content, and the squirt-flow peak at high water saturation (a). The Biot peak gradually moves towards higher water saturation as the frequency increases (b and c), while the squirt-flow peak disappears. Moreover, at higher frequencies (c) the attenuation reveals stronger dependency on the clay content at high water saturation. For a fully saturated rock ($S_w = 1$) at 1 MHz, i.e. at standard laboratory conditions, the attenuation increase monotonically with the clay content (c) in agreement with the experimental results of Klimentos and McCann (1990) and Best et al. (1994).

The presence of clay increases the surface area, decreases the permeability and increases the attenuation of the slow wave (Klimentos and McCann, 1988). Furthermore, the presence of the slow wave constitutes an attenuation mechanism for the fast P wave because of mode conversion at heterogeneities. This effect is implicit in the computation of synthetic seismograms when using a full-wave modelling method (e.g., Carcione, 1998, Pham et al., 2002a,b).

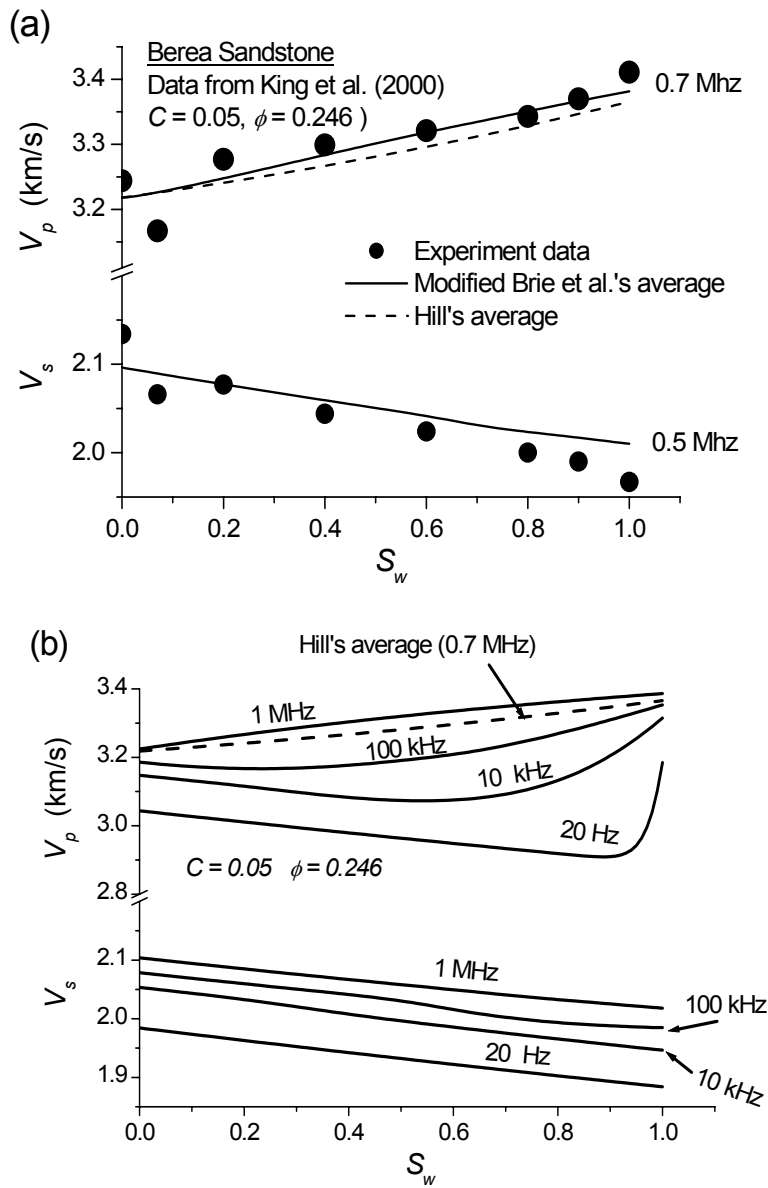


Figure 4.4: P- and S-wave velocities predicted by the present model compared to the experimental data of King et al. (2000) at ultrasonic frequencies (a). The same properties in (b), but for all frequencies. Also shown, is the P-wave velocity obtained by using Hill's equation.

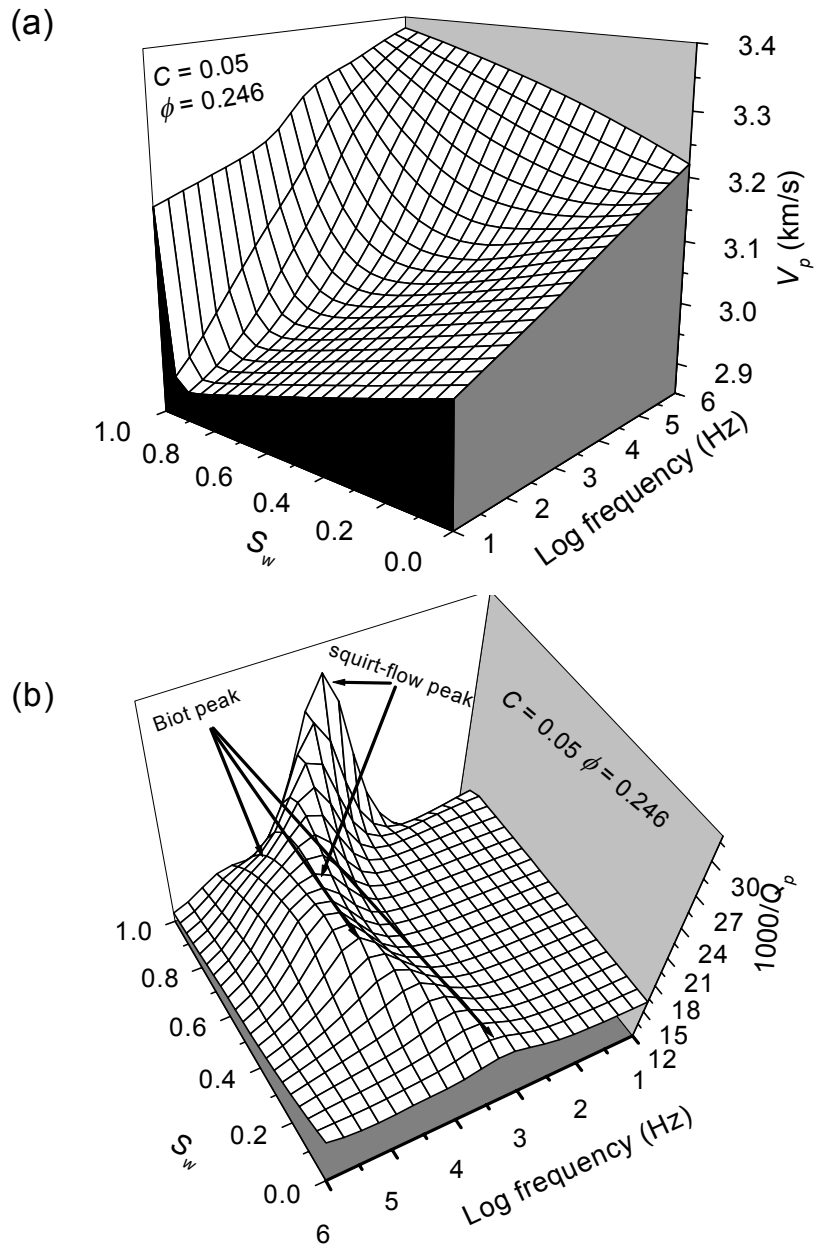


Figure 4.5: The P-wave velocity (a) and dissipation factor (b) as functions of water saturation and frequency.

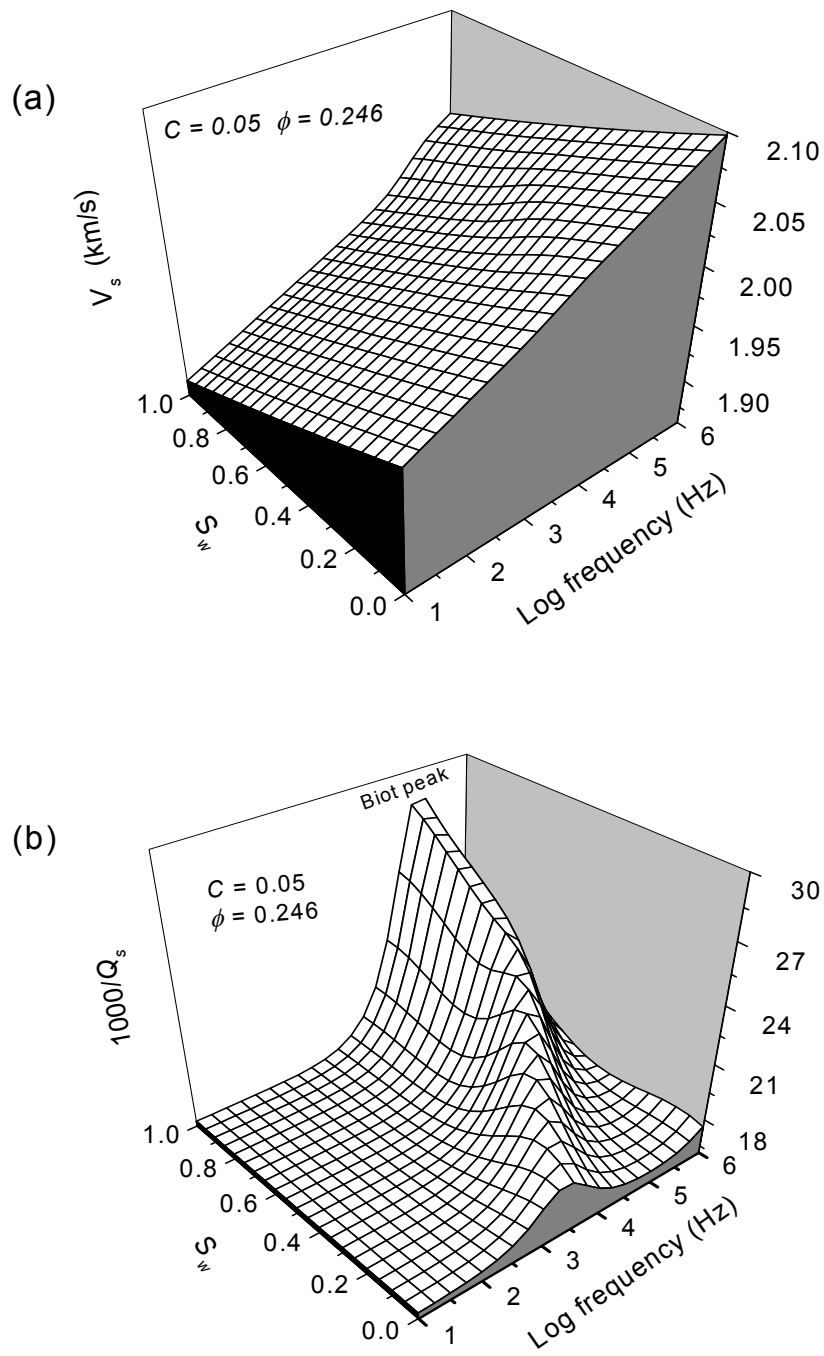


Figure 4.6: The S-wave velocity (a) and dissipation factor (b) as functions of water saturation and frequency.

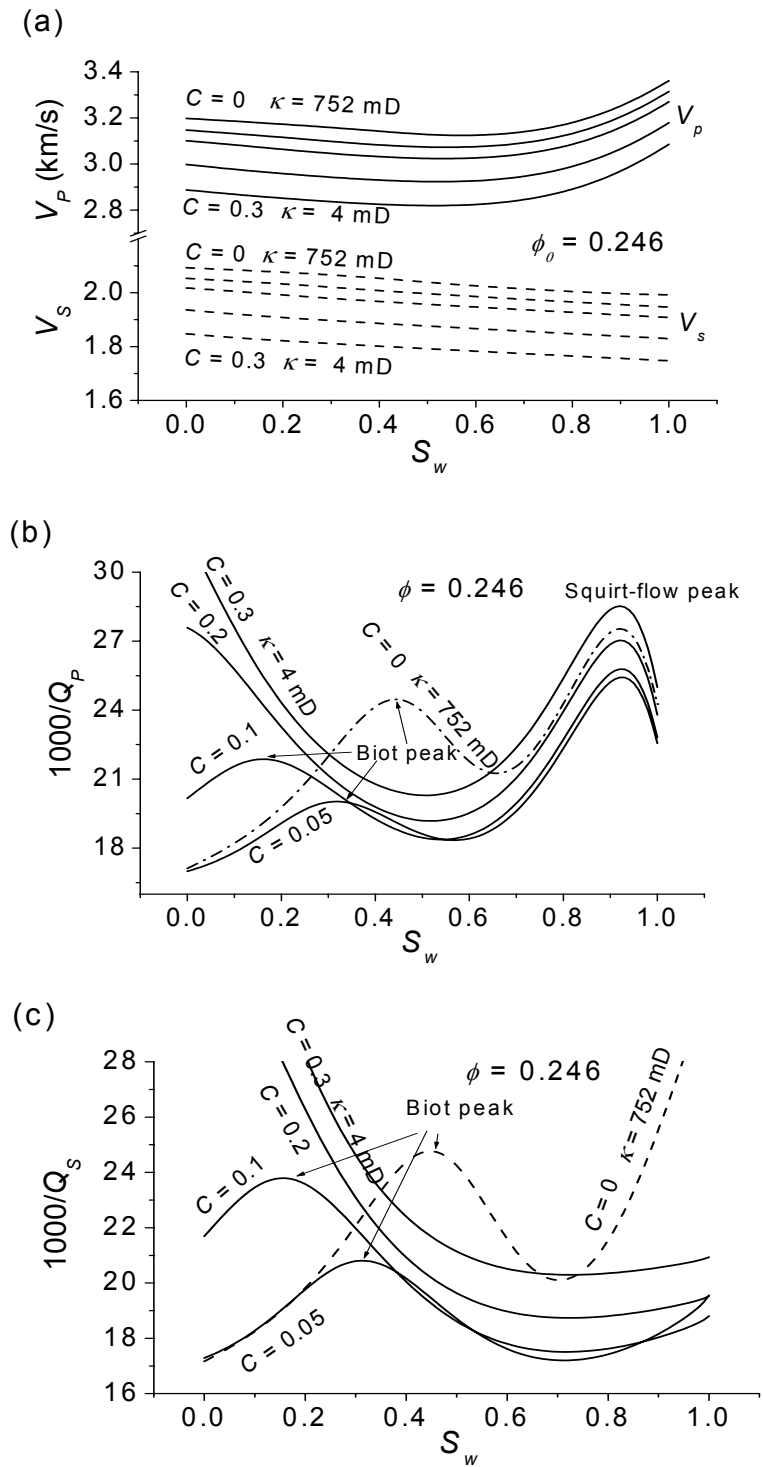


Figure 4.7: Wave velocities (a) and dissipation factors (b and c) versus water saturation for different values of the clay content C at a frequency of 10 kHz.

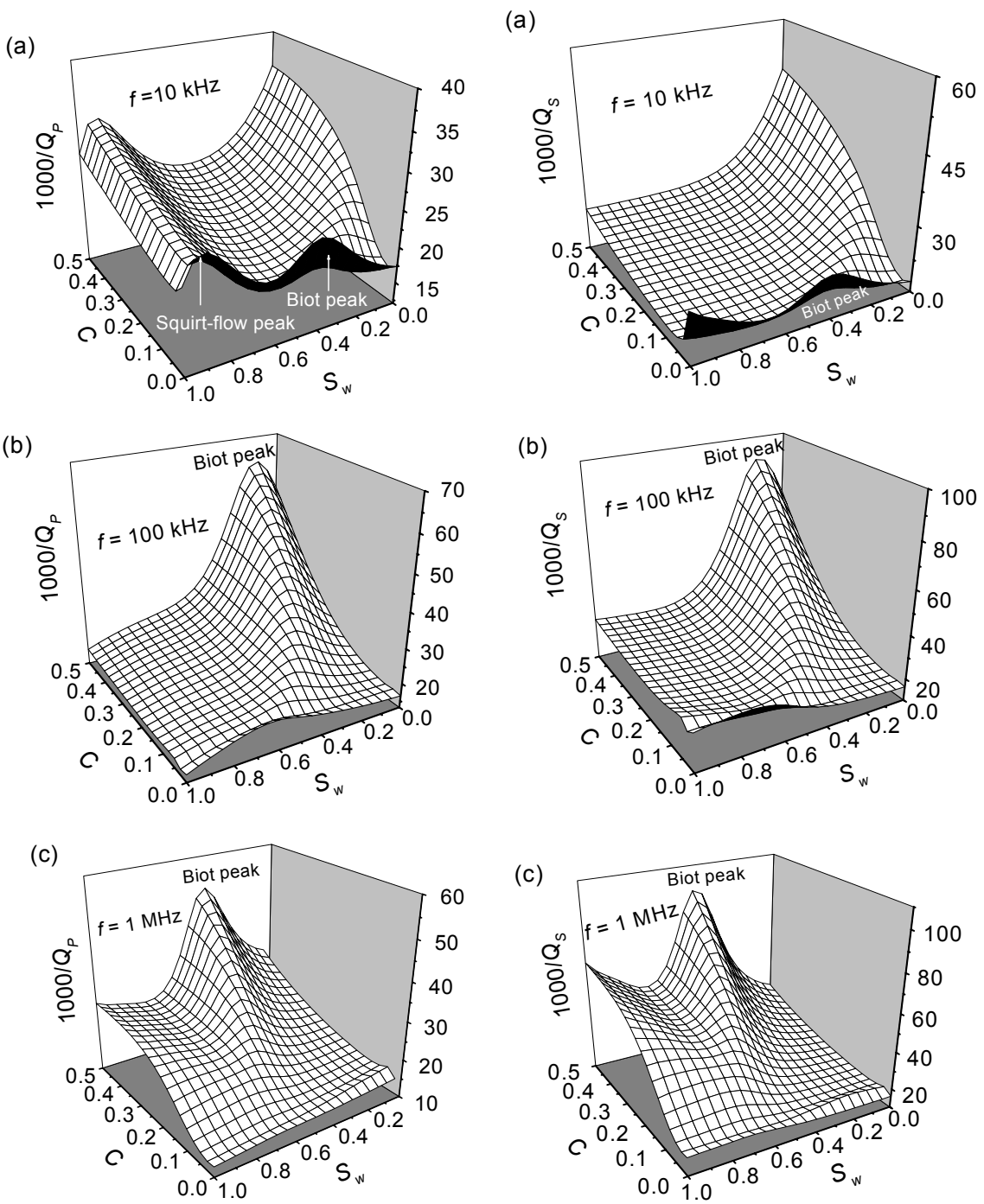


Figure 4.8: The P-wave dissipation factor as function of water saturation S_w and clay content C for 10 kHz (a), 100 kHz (b) and 1 MHz (c).

Figure 4.9: Same properties as in figure 4.8, but for S-wave.

4.5 Discussion and conclusions

The justification for the empirical relationships for the fluid mixture is mainly practical, for which the background models have been developed and applied. The main objective is to express the physical properties and mobility of the composite fluid within the porous rock in response to the imposed wavefield, for a range of wavelengths. Due to lack of a micro-structural theory, we consider here the affect on the bulk properties of rock containing the mixture rather than the detailed flow patterns at pore scale, which are invisible to the waves commonly applied in field and laboratory experiments. In the present study, strong velocity dispersion (Figure 4.5a) obtained in the partially saturated rock is mainly due to the fluid modulus of the mixture (eq. 4.11; Figure 4.3).

For instance, the two-phase effective permeability concept is based on the assumption that the transfer of momentum between the two fluid phases is negligible and can be used in a relation between effective fluid mobility and the geometrical parameters of void space (e.g., Kozeny-Carman relation). The only difference is that now, each of these parameters and hence the effective permeability is a function of saturation. The relative permeability model may not be valid for motion on a pore scale. In the present study the relative permeability model effects Biot flow (global flow), but not squirt flow (local flow).

Empirical mixing laws have been developed for the mixture of fluids (gas/liquid). The model for partial saturation, based on physical theory and experimental results (e.g., Murphy et al., 1982, Yin et al., 1991), shows good agreement with Voigt's and Wood's bounds (upper and lower bound). Additionally, the viscoelasticities of the rocks are included and modelled for the whole frequency range. The advantage of this theory is that the model can be applied and used for the whole frequency range, seismic, sonic, and ultrasonic.

The model displays the behaviour of sandstones in many respects. For instance; i) Wave velocities increase considerably with increasing frequency (at low frequencies, the fluid has enough time to achieve pressure equilibration, while at high frequencies, the fluid cannot relax and the bulk and shear moduli are stiffer), ii) For a Berea sandstone, the P- wave attenuation has a maximum at approximately the location of the squirt-flow peak and 90 % water saturation in sonic frequency band (10 kHz), and iii) In general, attenuation increases with increasing clay content. This effect is mainly due to the moduli (stiffness) of clay matrix being less than the moduli of the sand matrix.

The limitations of the model are considered to be mainly due to the modelling of the viscoelastic effects. For both the constant- Q model and the Zener model, we need a number of quantified input factors in order to fit a general functional

behaviour of quality factor and velocity dispersion versus frequency. Furthermore, Q -factor measurements are difficult to obtain with enough reliability.

As mentioned before, no micro-structural theory (e.g., the Zener model used for squirt-flow phenomenon), however, is able to predict the exact behaviour of intermediate frequencies. The problem with mixed fluid phases is that velocities and attenuation depend not only on frequency and saturation, but also on the partial distribution (micro-structural property) of the fluid phases in the rocks (Cadoret, 1995). In chapter 6, numerical experiments in partially saturated rocks will be presented to study the different physical mechanisms including the fluid distribution effect on the wave field, and to understand and locate the position of the relaxation peak, related to the dynamic behaviour of the hydrocarbons in reservoirs.

Chapter 5

Pressure effects

5.1 Introduction

First, I introduce some useful definitions of the different pressures considered in this work. Pore pressure, also known as formation pressure, is the in-situ pressure of the fluids in the pores. The pore pressure is equal to the hydrostatic pressure when the pore fluids only support the weight of the overlying pore fluids (mainly water). The lithostatic or confining pressure is due to the weight of overlying sediments, including the pore fluids. The pore pressure attains lithostatic pressure when fluid flow is restricted. However, fractures perpendicular to the minimum compressive stress direction appear for a given pore pressure, typically 70-90 % of confining pressure. When fracturing occurs, the fluid escapes from the pores and pore pressure decreases. A rock is said to be overpressured when its pore pressure is significantly greater than hydrostatic pressure (Figure 5.1). The difference between confining pressure and pore pressure is called differential pressure. Acoustic and transport properties of rocks generally depend on effective pressure, a combination of pore and confining pressure (see equation 5.3). Various physical processes cause anomalous pressures on an underground fluid. The most common causes of overpressure are compaction disequilibrium and cracking, i.e., oil to gas conversion (Mann and Mackenzie, 1990; Luo and Vasseur, 1996).

The overpressured zone is a well-known problem in the drilling process. In general, abnormally high-pressure in a well zone gives difficulty and delay in the drilling process. Therefore, knowledge of pore pressure will help in planning the well so as to avoid the overpressured zone. In addition, the abnormally high-pressure zone may relate to high potential hydrocarbon zone (gas zone). Thus, knowledge about the relation of wave velocities and attenuations corresponding

to pressure is an important task and a new challenge in geophysics in order to predict and detect the abnormal pressure zones from seismic data.

Several scientists have investigated pressure effects on the wave responses. Christensen and Wang (1985) measured how velocities were affected by pore pressure and confining pressure of Berea sandstone. Berryman (1992) introduced the effective stress for transport properties of inhomogeneous porous rock. Carcione and Gangi (2000a,b) studied the effect on velocities of abnormal pore pressure due to compaction and gas generation, respectively. In general, non-seismic methods to predict pore pressure are based on a relation between porosity or void ratio and effective stress (Bryant, 1989; Audet, 1996; Traugott, 1997; Holbrook et al. 1995). Indirect use of velocity information involves the estimation of porosity profile by using sonic-log data (Hart et al., 1995; Harrold et al., 1999). An MWD (measurement while drilling) technique is proposed by Lesso and Burgess (1986), based on mechanical drilling data [rock strength computed from ROP (rate of penetration), and weight on bit (DWOB) and torque (DTOR)] and gamma ray logs. Seismic data can be used to predict abnormal pore pressures in advance of drilling. In general, this prediction has been based on empirical models relating pore pressure to sonic and/or seismic velocity (Dutta and Levin, 1990; Foster and Whalen, 1966; Pennebaker, 1968; Eaton, 1976; Belotti and Giacca, 1978; Bilgeri and Ademenio, 1982; Keyser et al., 1991; Kan and Sicking, 1994; Bowers, 1995; Eaton B. A. and Eaton T. L., 1997; Sayers et al., 2000).

Unlike previous approaches, we use a Biot-type three-phase theory, two solids (sand and clay) and one fluid (see chapter 2). The theory includes the effects of pore pressure and confining pressure. Pressure effects are introduced by using an effective stress law. As is well-known, at constant effective pressure the acoustic (or transport) properties of the rock remain constant. The effective pressure depends on the difference between the confining and pore pressures, the latter multiplied by the effective stress coefficient (Christensen and Wang, 1985; Berryman G. J., 1992; Gangi and Carlson, 1996; Carcione and Gangi, 2000a,b). In general, this coefficient is not equal to one and, therefore, the Terzaghi effective pressure law (that is, the differential pressure) is not an appropriate quantity to describe the acoustic properties of the rock and varying pore pressure. However, a proper determination of the effective stress coefficients requires measurements of wave velocity as a function of confining and pore pressure. In order to estimate pore pressure from seismic data, the method requires high-resolution velocity information, preferably obtained from seismic inversion techniques. Interval velocities obtained from conventional seismic processing are not reliable enough for accurate pore pressure prediction (Sayers et al. 2000; Carcione and Tinivella, 2001). The model requires first calibration with regional data (well information) for quantifying the rock properties, and then the use of an inversion technique for pore pressure prediction from seismic data (P-wave velocity) (Cacione et al., 2002a; Pham et al., 2002c). Laboratory measurements of

P-wave and S-wave velocities on cores samples may further improve the calibration process (Carcione and Gangi, 2000a,b). If squirt flow is the dominant mechanism, then we could implement the Zener model or the other models (e.g., power-law model; see Ursin and Toverrud, 2002), but we must know in advance the rock properties in order to calibrate the model with region data.

The method was applied to the Tune field on the Viking Graben sedimentary basin of the North Sea (Carcione et al., 2002a). A high-resolution velocity map that reveals the sensitivity to pore pressure and fluid saturation in the Tarbert reservoir is obtained from 3-D pre-stack velocity by tomography and depth imaging. The pressure map predicted in Tabert Formation shows good agreement with local well data and the structural features of the Tarbert Formation and its known pressure compartments.

5.2 Method

As stated in previous work (Carcione and Gangi, 2000a,b), the large change in seismic velocity is mainly due to the fact that the dry-rock moduli are sensitive functions of the effective pressure, with largest changes occurring at low differential pressures. The major effect of porosity is implicit in the dry-rock moduli. Explicit changes in porosity and saturation are important but have a smaller influence than changes in the moduli. In fact, the variations of porosity for Navajo sandstone, Weber sandstone and Berea sandstone are only 1.7 %, 7 % and 4.5 %, respectively, for changes of the confining pressure from 0 to 100 Mpa (Berryman, 1992).

In order to use the theory to predict pore pressure, we need to obtain an expression for the dry-rock moduli versus effective pressure. The calibration process should be based on well data, geological and laboratory data, mainly sonic, density data, porosity and clay content inferred from logging profiles.

Let us assume a rock at depth z . The lithostatic or confining pressure p_c can be obtained by integrating the density log (Figure 5.1),

$$p_c = g \int_0^z \rho(z') z' dz', \quad (5.1)$$

where ρ is the bulk density and g is the acceleration of gravity. Furthermore, the hydrostatic pore pressure is approximately given by

$$p_h = g \rho_w z, \quad (5.2)$$

where ρ_w is the density of water.

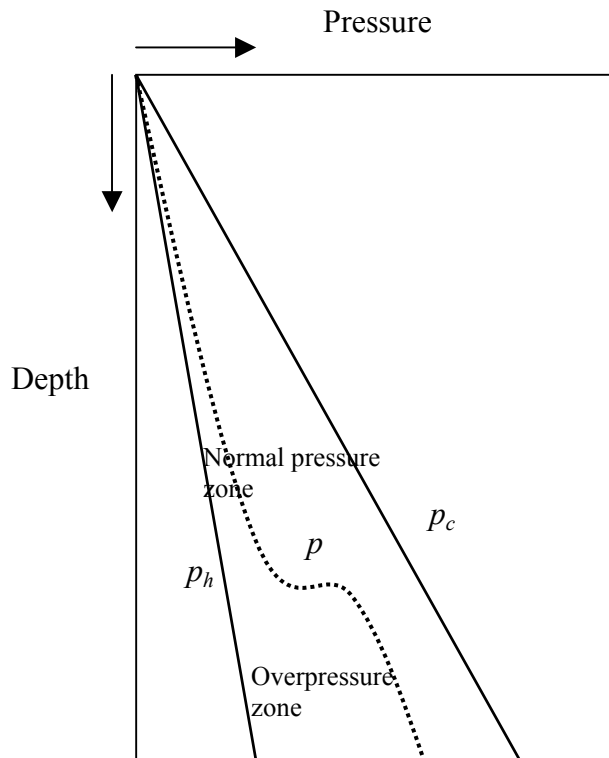


Figure 5.1: The schematic Figure of pressures versus depth.

5.2.1 Effective stress coefficients

Observations reveal that changes in velocities resulting from changes in confining pressure are not exactly cancelled by equivalent changes in pore pressure. Therefore, as a good approximation (Prasad and Manghnani, 1997), compressional and shear moduli depend on effective pressure,

$$p_e = p_c - np \quad (5.3)$$

where p is the pore pressure and n is the effective stress coefficient, which can be different for velocities and moduli (Christensen and Wang, 1985). Note that the effective pressure equals the confining pressure at zero pore pressure. It is found that $n \approx 1$ for static measurements of compressibilities (Zimmerman, 1991), while n is approximately linearly dependent on the differential pressure $p_d = p_c - p$ in dynamic experiments (Gangi and Carlson, 1996; Prasad and Manghnani, 1997). Therefore, we assume

$$n = n_0 - n_1 p_d. \quad (5.4)$$

This dependence of n versus differential pressure is in good agreement with the experimental values corresponding to the compressional velocity obtained by Christensen and Wang (1985) and Prasad and Manghnani (1997). It is clear that to obtain n_0 and n_1 , we need two evaluations of n at different pore pressures, preferably a normally pressured well and an overpressured well. Alternatively, n_0 can be assumed equal to 1, and only one evaluation is necessary in this case. If one well or equally pressured wells are available, the algorithm provides an average value for n .

5.2.2 Dry-rock moduli as function of effective pressure

As seen from equation (2.5), the (modified) model of Krief et al. (1990) can only describe the dependencies of bulk and shear moduli on porosity and clay content, but not on pressure. In fact, the dry-rock moduli are sensitive functions of the effective pressure. Experiments (Gangi and Carlson, 1996; Prasad and Manghnani, 1997) show that functional forms of the dry-rock moduli as a function of effective pressure:

$$M(z) = \alpha(z) \left[1 - \exp(-p_e(z)/p^*(z)) \right], \quad (5.5)$$

where $\alpha(z)$ is the maximum value of $M(z)$ when the effective pressure is extremely high, i.e., the confining pressure is much higher than pore pressure. $\alpha(z)$ is therefore, assumed equal to the Hashin-Shtrikman (HS) upper bounds (Hashin and Shtrikman, 1963, Mavko et al. 1998, p. 106), and $p^*(z)$ is obtained (for each modulus) by fitting the (modified) expressions of Krief et al. (eq. 2.5),

$$\begin{aligned} K_{sm}(z) &= \beta K_{HS}(z) \left[1 - \exp(-p_e(z)/p_K^*(z)) \right] \\ \mu_{sm}(z) &= \beta \mu_{HS}(z) \left[1 - \exp(-p_e(z)/p_\mu^*(z)) \right] \end{aligned} \quad (5.6)$$

where K_{HS} and μ_{HS} are Hashin-Shtrikman upper bounds, β is a constant weight factor to account for softening of the rocks, which can be obtained by fitting regional data.

5.2.3 Hashin-Shtrikman upper bounds

At any given volume fraction of constituents the effective modulus will fall between the bounds but its precise value depends on the geometric details. The best bounds, defined as giving the narrowest possible range for an isotropic rock, are the Hashin-Shtrikman (HS) bounds (Hashin and Shtrikman, 1963). The HS upper bound given by

$$\begin{aligned}
K_{HS}(z) &= \left\{ K_s + \phi(z) \left[(1 - \phi(z)) \left(K_s + \frac{4}{3} \mu_s \right)^{-1} - K_s^{-1} \right]^{-1} \right\} \\
\mu_{HS}(z) &= \left\{ 1 + 5\phi(z) \left[2(1 - \phi(z))(K_s + 2\mu_s) \left(K_s + \frac{4}{3} \mu_s \right)^{-1} - 5 \right]^{-1} \right\}.
\end{aligned} \tag{5.7}$$

Note that the HS lower bound is zero, and that the Voigt bounds are $(1-\phi)K_s$ and $(1-\phi)\mu_s$, respectively. For quartz grains with clay, $K_s = 39$ GPa and $\mu_s = 33$ GPa (Mavko et al., 1998, p.307). If the porosity limit is 0.2, the HS upper bounds for the bulk and shear moduli are 26 GPa and 22 GPa, compared to the Voigt upper bounds 31 GPa and 26 GPa, respectively. However, the HS bounds are still too large to model the moduli of in-situ rocks. These contain clay and residual water saturation, inducing a chemical weakening of the contacts between grains (Knight and Dvorkin, 1992; Mavko et al., 1998, p. 203). Therefore, these bounds are multiplied by the factor $\beta < 1$, which can be obtained by fitting regional data. Figure 5.2 shows the dry-rock bulk modulus of several reservoir rocks for different confining pressures (Zimmerman, 1991, p. 29, Table 3.1), compared to the HS upper bounds. The solid line represents the analytical curve. Based on these data we apply a constant weight factor $\beta = 0.8$ [$K(p_c=300\text{MPa})/K_{HS} \approx 0.8$ (see Figure 5.2)] to the HS bounds to account for the softening effects (Carcione et al., 2002a).

5.2.4 Gas dependencies on pressure and temperature

The densities and compressibilities of oil and water are less sensitive to pressure and temperature than those for gas. The isothermal gas bulk modulus K_g and the gas compressibility $c_g = K_g^{-1}$ depend on pressure and temperature. The latter can be calculated from the Van der Waals equation

$$(p + b\rho_g^2)(1 - c\rho_g) = \rho_g RT, \tag{5.8}$$

where p is the gas pressure (pore pressure), ρ_g is the gas density, T is the absolute temperature and R is the gas constant. Moreover, a good approximation can be obtained using $b = 0.225 \text{ Pa (m}^3/\text{mole)}^2 = 879.9 \text{ Mpa (cm}^3/\text{g)}^2$ and $c = 4.28 \times 10^{-5} \text{ m}^3/\text{mole} = 2.675 \text{ cm}^3/\text{g}$ (one mole of methane, CH_4 , corresponds to 16 g), then,

$$\frac{1}{K_g} = \frac{1}{\rho_g} \frac{d\rho_g}{dp} = \left[\frac{\rho_g RT}{(1 - c\rho_g)^2} - 2b\rho_g^2 \right]^{-1}. \tag{5.9}$$

5.2.5 Pore pressure prediction procedure

The method for pore pressure prediction from seismic data is that we first calibrate the model with the local area, where formation properties such as porosity, clay content, confining pressure, pore pressure and velocities are known. Then, using an inversion technique, we obtain the pore pressure by fitting the modelled P-wave velocity with seismic P-wave velocity at the target area.

Ideally, a precise determination of the effective stress coefficient, n , requires laboratory experiments on saturated samples for different confining and pore pressures. However, even using those coefficients, n does not reflect the behaviour of the rock at the in-situ conditions, due to two main reasons. Firstly, laboratory measurements of wave velocity are performed at ultrasonic frequencies, and secondly, the in-situ stress distribution is different from the stress applied in the laboratory experiments. Therefore, we proceed as follows:

1. The (modified) model of Krief et al. (1990) (eq. 2.5) is calibrated with regional area (laboratory data or well data) to quantify the empirical coefficients A and a of the rocks.
2. We compute the exponential coefficients p^* (eq. 5.6) using the dry-rock moduli from the (modified) expressions of Krief et al. (eq. 2.5) where A and a were obtained from step (1), the effective pressure p_e from equation (5.3), the confining pressure from equation (5.1), the pore pressure from well log, HS upper bounds from equation (5.7) and the effective stress coefficients $n = 1$.
3. Then, the in-situ effective stress coefficients are obtained by fitting the theoretical wave velocities [three-phase Biot-type model (chapters 2, 3 and 4)] to the sonic-log wave velocities, using the dry-rock moduli versus effective pressure [eq. 5.6 with p^* from step (2)], and n as a fitting parameter. The effective stress coefficient versus pore pressure, corresponding to the same geological unit, is obtained by using the linear law (eq. 5.4).
4. Finally, by applying three-phase Biot-type model including pressure-dependent dry moduli, the pore pressure can be predicted at the target area from seismic data (seismic velocity) by using an inversion technique. Here, the pore pressure is obtained by fitting the modelled P-wave velocities with the measured seismic P-wave velocities, assuming that the target area and calibrated area have the same type of rocks. The pore pressure prediction flow-chart is shown in Figure 5.3.

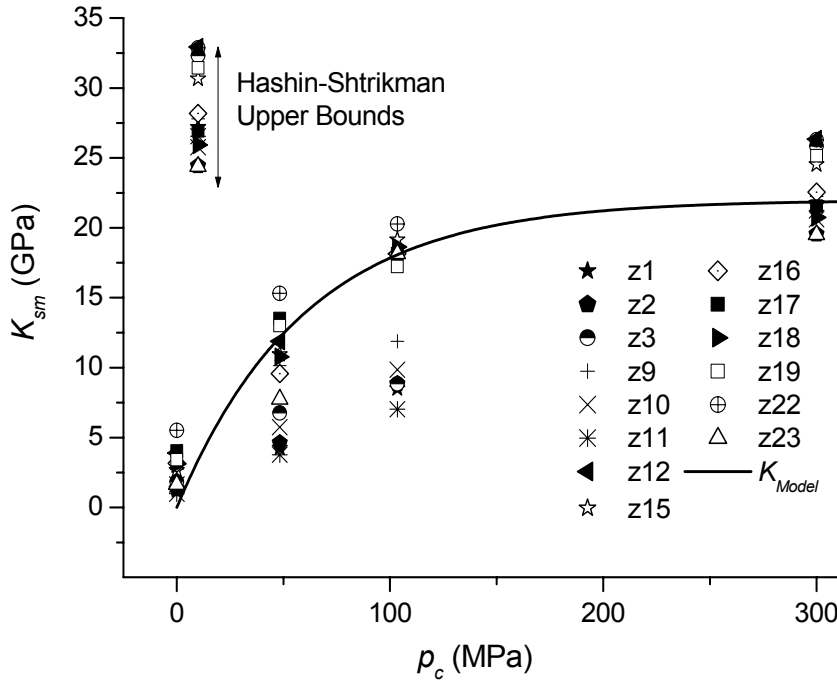


Figure 5.2: Dry-rock bulk modulus of several reservoir rocks for different confining pressure compared to the HS upper bounds. The solid line represents the analytical curve.

Note that in this study, the clay-matrix moduli are simply given by the (modified) expressions of Krief et al. (eq. 2.5), with no explicit dependence on pressure, since this is the case of shaley sandstones ($C < 0.5$). In the case of gas, the gas density and its bulk modulus is calculated by Van der Waals equations (5.8) and (5.9).

Let us perform an estimation of the error in determining p_K^* . Partial differentiation of p_K^* with respect to K_{sm} and p_e implies that the error in the determination of p_K^* is

$$\Delta p_K^* = \frac{p_K^*}{P_e} \left(\frac{p_K^* \Delta K_{sm}}{K_{HS} - K_{sm}} + \Delta p_e \right), \quad (5.10)$$

where ΔK_{sm} and Δp_e are the errors corresponding to K_{sm} and p_e , respectively. Consider the following example: $K_{HS} = 30$ GPa, $\Delta K_{sm} = 1$ GPa and $\Delta p_e = 1$ MPa. For $p_K^* = 15$ MPa (soft rock), the error is 4.5 MPa at $p_e = 50$ MPa, and 20 MPa at $p_e = 5$ MPa, while for $p_K^* = 40$ MPa (stiff rock), the error is 4.5 MPa at $p_e = 50$ MPa, and 5.1 MPa at $p_e = 5$ MPa. Therefore, the analysis indicates that a better

estimation of p_K^* is achieved at high effective pressures and stiff rocks, that is, using data from normally pressured wells.

An alternative derivation of the dry-rock moduli can be obtained from laboratory experiments. These experiments are based on sandstone or shaley sandstone cores, since dry measurement in shale is practically impossible to perform. The bulk and shear moduli K_{sm} , μ_{sm} versus confining pressure can be obtained from laboratory measurements in dry samples. Having the experimental compressional and shear velocities $V_P^{(dry)}$, $V_S^{(dry)}$, respectively, the moduli are given approximately by

$$\begin{aligned} K_{sm} &= (1-\phi) \rho_s \left(V_P^{2(dry)} - \frac{4}{3} V_S^{2(dry)} \right), \\ \mu_{sm} &= (1-\phi) \rho_s \left(V_S^{2(dry)} \right), \end{aligned} \quad (5.11)$$

where ρ_s is the grain density. We recall that K_{sm} is the rock modulus at constant pore pressure, i.e. the case when the bulk modulus of the pore fluid is negligible compared with the dry-rock bulk modulus, as for example air at room conditions.

For $C < 0.5$ and $C > 0.5$, the clay- and sand-matrix moduli are simply given by the (modified) expressions of Krief et al.. The effective stress coefficients can be measured from the laboratory experiments on wet-rock samples versus confining and pore pressures. In this way, the effective stress law can be obtained.

In some cases, velocity information alone is not enough to distinguish between a velocity inversion due to overpressure or due to pore fluid and lithology, e.g., base-of-salt reflections (Miley, 1999, Miley and Kessinger, 1999). There are cases, where overpressuring is not associated with large velocity variation, as in smectite/illite transformations. Best et al. (1990) use AVO analysis to treat these cases. Modelling analysis of AVO signatures of pressure transition zones are given in Miley (1999) and Miley and Kessinger (1999) and Carcione (2001c). This type of analysis should complement the present prediction method based on geological information of the study area.

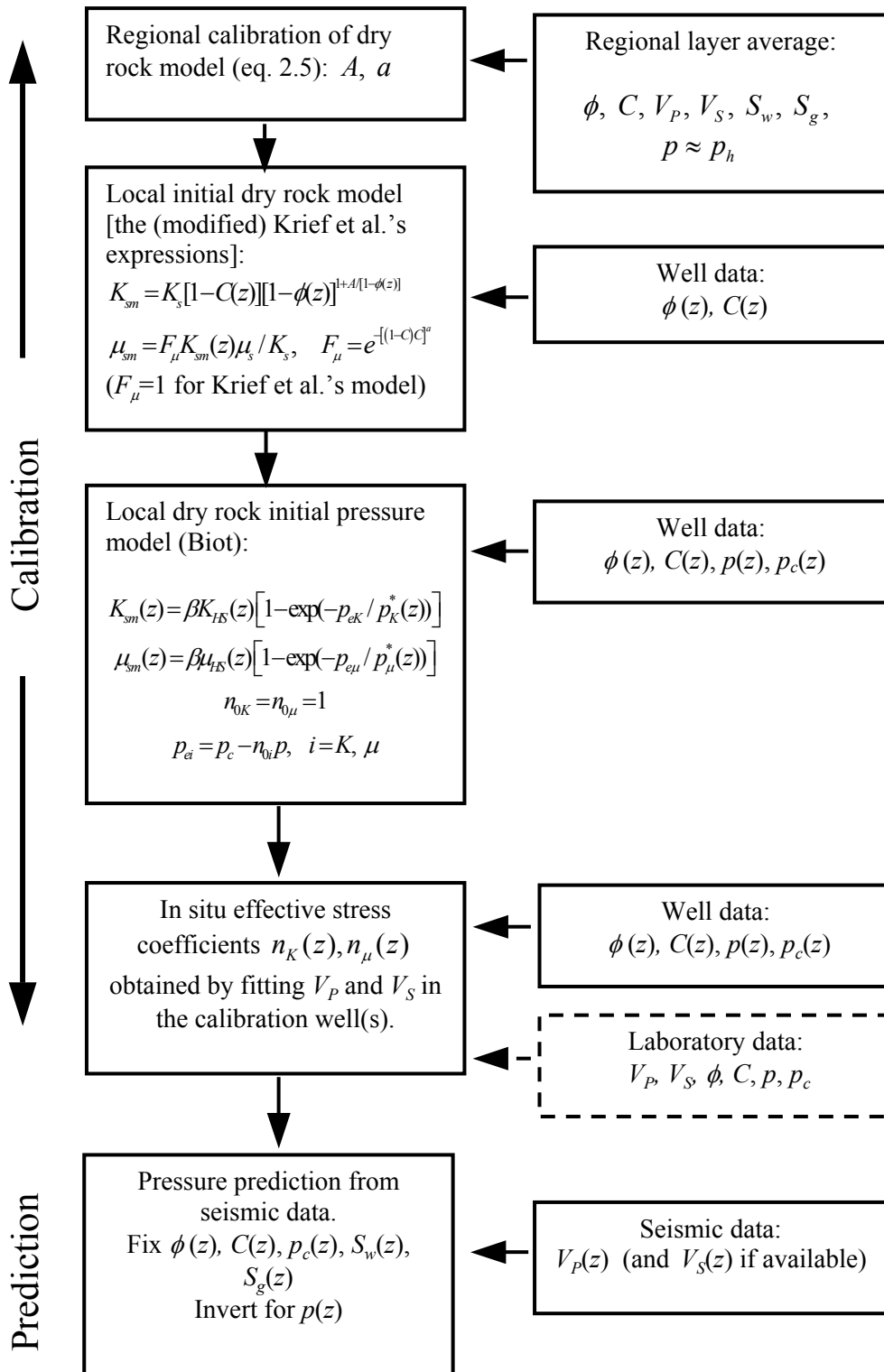


Figure 5.3: Flow chart illustrating the pore pressure prediction method from seismic data.

5.3 Case study

Let us continue with the example in chapter 4. The pressure effect is now included in the three-phase Biot-type model. We assume the reference value of differential pressure is 40 Mpa ($p_c = 70$ Mpa and $p = 30$ Mpa), and the temperature is 90 °C in Van der Waals equations (eqs. 5.8, 5.9), corresponding to a reservoir at 3 km depth. The dry rock moduli as a function of porosity, clay content, and pressure were obtained following steps 2 and 3 of the procedure described in section (5.2.5), while the empirical parameters are: $A = 2.8$ and $F_\mu = 1$, corresponding to the example in chapter 4 (Pham et al., 2002c).

Three-dimensional plots of the P-wave velocity (a) and dissipation factor (b) versus differential pressure - confining pressure minus pore pressure - and water saturation are displayed in Figure 5.4. The clay content is 0.05 (5 %) and the frequency is 30 Hz. The same is in Figure 5.5 but for S-wave velocity (a) and attenuation (b). For both P- and S-waves the velocities increase, while the attenuation decreases strongly with increasing differential pressure. This effect is mainly due to the dry-rock moduli being sensitive to effective pressure. The larger the differential pressure the greater is the stiffness of the rock, which leads to an increase in velocities and quality factors. In particular, at extremely low effective pressure, the rock becomes unconsolidated and the dry-rock moduli approach zero. The attenuation is not effected by saturation change, since this is a low frequency case (30 Hz).

In order to demonstrate the pressure effects on wave velocities at different rock porosities, we consider porosities of 0.1, 0.2, 0.246, and 0.3. Pore pressure is kept constant at 30 Mpa, while confining pressure varies from 30 to 200 Mpa. The results of P-wave (a) and S-wave (b) velocities are shown in Figure 5.6. For both P- and S-wave, the velocities increase with decreasing porosity. The advantage of the model is that, unlike previous work (Carcione and Gangi, 2000a,b), the dry-modulus upper bounds (HS) are also porosity dependent. At high porosity, the velocities reveal strong dependency on pressures. This behaviour is in good agreement with physical nature with the fact that the higher the porosity, the softer is the rock, inducing a more pronounced effect of pressures on the rock compressibility. For well-consolidated and cemented rocks, the simple eq. (5.5) may not be an accurate representation of the modulus around zero pressure. Here the model predicts zero modulus whereas the experimental data on sandstones reveal small but finite values (Figure 5.2). This gives trouble for low porosity rocks as shown in Figure 5.6 at low p_d .

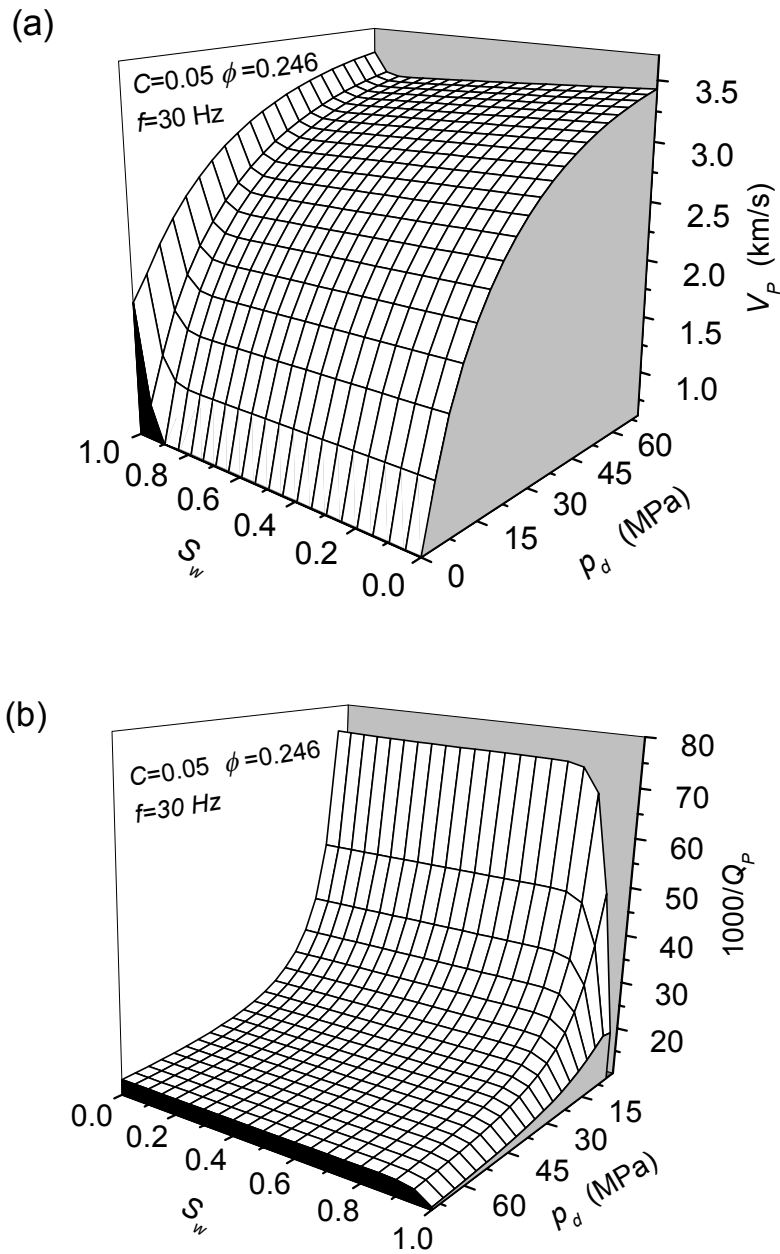


Figure 5.4: The P-wave velocity (a) and dissipation factor (b) as functions of differential pressure and water saturation.

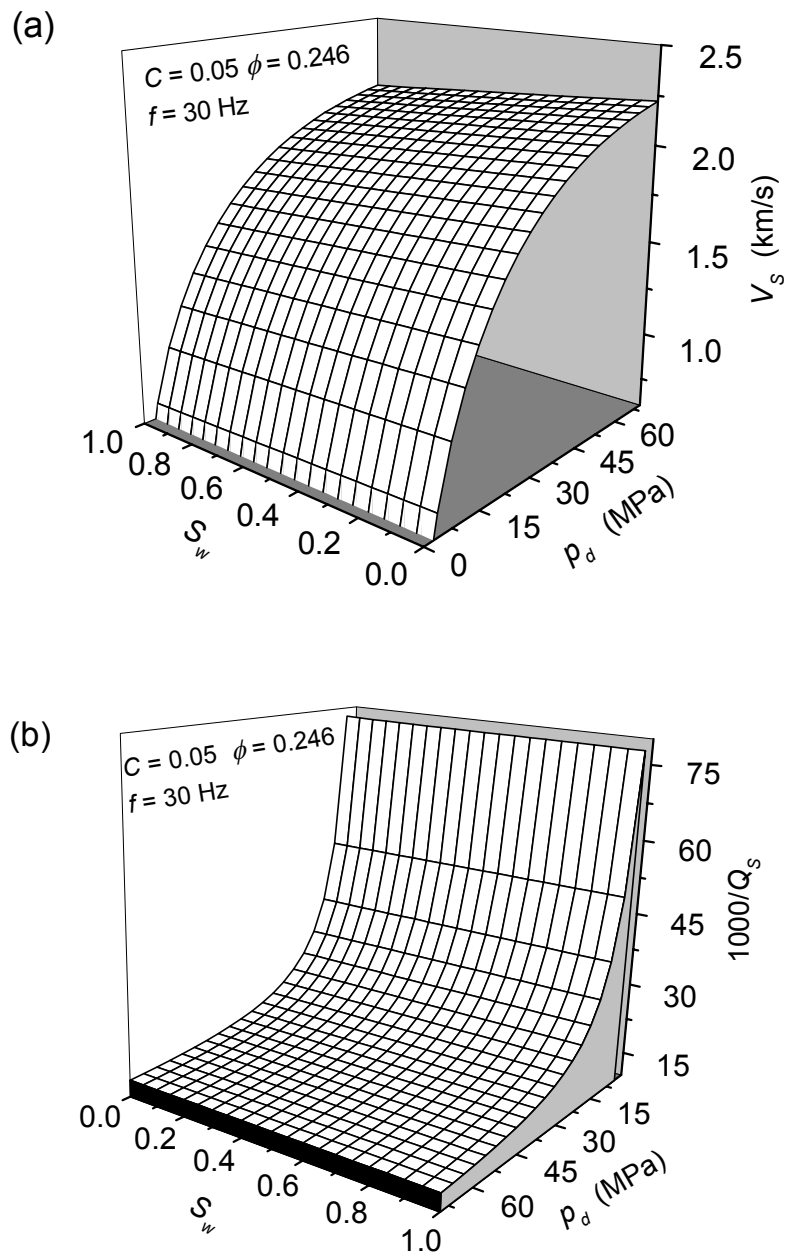


Figure 5.5: The S-wave velocity (a) and dissipation factor (b) as functions of differential pressure and water saturation.

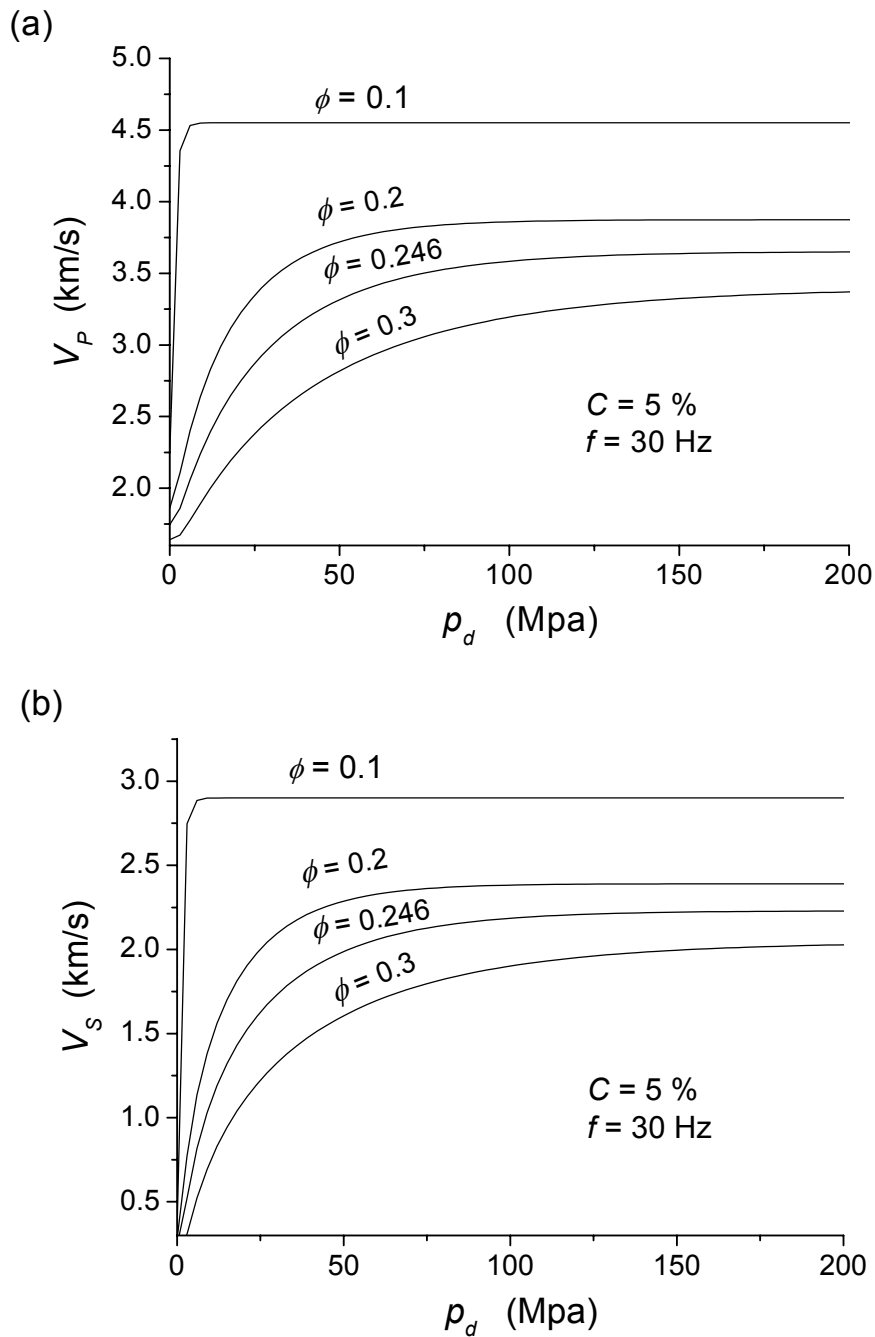


Figure 5.6: P-wave (a) and S-wave (b) velocities as functions of differential pressure with different porosities.

5.4 Pore pressure prediction on the Tune field

Using the pressure prediction method described in section 5.2.5, we are able to detect and predict the overpressured zones of the Tune field area in the Viking Graben sedimentary basin of the North Sea. The model is first calibrated against local wells and then using an inversion technique we predict pore pressure, while the input velocity field is determined by tomography of depth migrated gathers (Carcione et al., 2002a).

5.4.1 Application and analysis on the Tune field

We consider the Tune field area in the Viking Graben of the North Sea (Figure 5.7). This basin is 170-200 km wide, and represents a fault-bounded north-trending zone of extended crust, flanked by the mainland of western Norway and the Shetland platform. The area is characterised by large normal faults with north, north-east, and north-west orientations which define tilted blocks. Such blocks contain the same sequences as the wells that are used for this study. The main motivation for selecting this area is the fact that high overpressure compartments were identified by drilling, and that higher overpressure is expected in future wells at the down flank side towards the central Viking Graben. A detailed analysis of the fault sealing and pressure distribution in Tune field are given by Childs et al. (2001).

Figure 5.8 displays a time-structure map of Top Ness, showing the pressure compartments enclosed by faults and the locations of three wells. Well 2 and 3 are in the high pore pressure region with 15 Mpa overpressure and well 1 has almost normal (hydrostatic) pore pressure and is highly deviated. The dashed line indicates the location of the seismic section shown in Figure 5.9. The calibration well (well 1) is an exploration well drilled to a depth of 3720 m (driller's depth) to test the hydrocarbon potential of the Jurassic Brent Group. The well includes reservoir rocks of the Tarbert and Ness Formations. The Tarbert sands are the target units, which are considered in the present study.

The 3-D marine seismic data was acquired by using a system of 6 streamers of 3 km length with a group interval of 12.5 m and cross-line separation of 100 m. The shot spacing was 25 m and the sampling rate 2 ms. The conventional stacked section is displayed in Figure 5.9, where the locations of the wells are shown. Figures 5.10, 5.11, and 5.12 show pressure and formation data (porosity ϕ , clay content C , density ρ , water saturation S_w and sonic-log velocities V_p and V_s) for the Tune wells. The shear wave velocity in well 3 is obtained by using the empirical relation $V_s = -791.75 + 0.76535V_p$ (m/s), which was obtained by fitting data from near-by wells. Note that well 1 is water bearing with moderate pore pressures while wells 2 and 3 are gas bearing and overpressured.

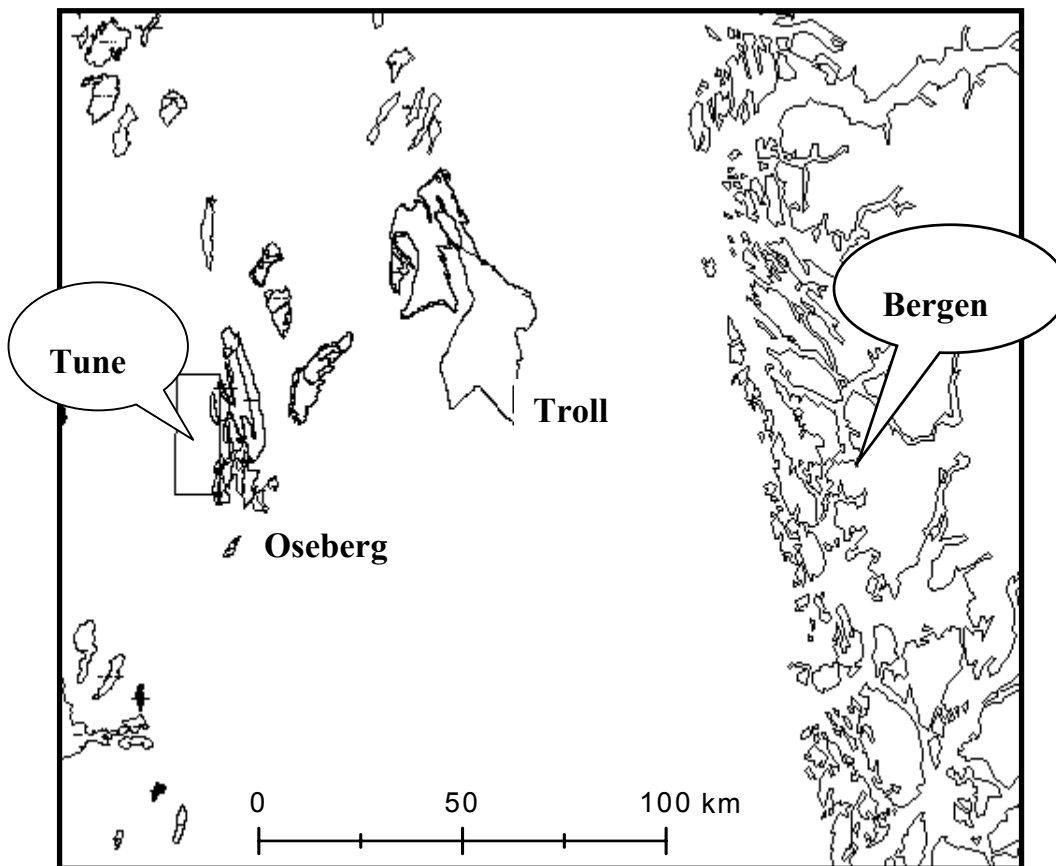


Figure 5.7: Location of the Tune field in the Norwegian sector of the North Sea.

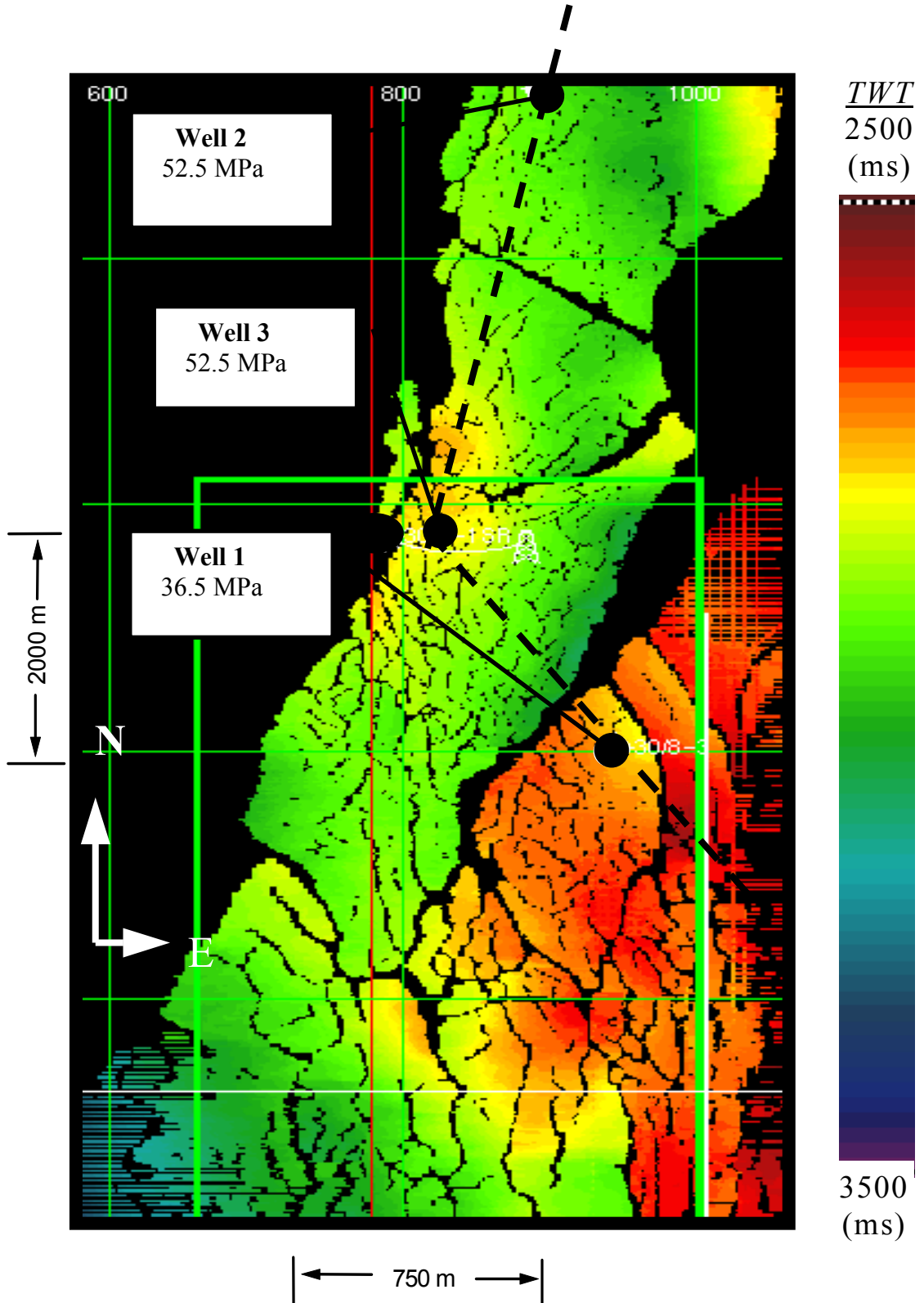


Figure 5.8: Time-structure map of Top Ness (base reservoir) showing the pressure compartments in the study area.

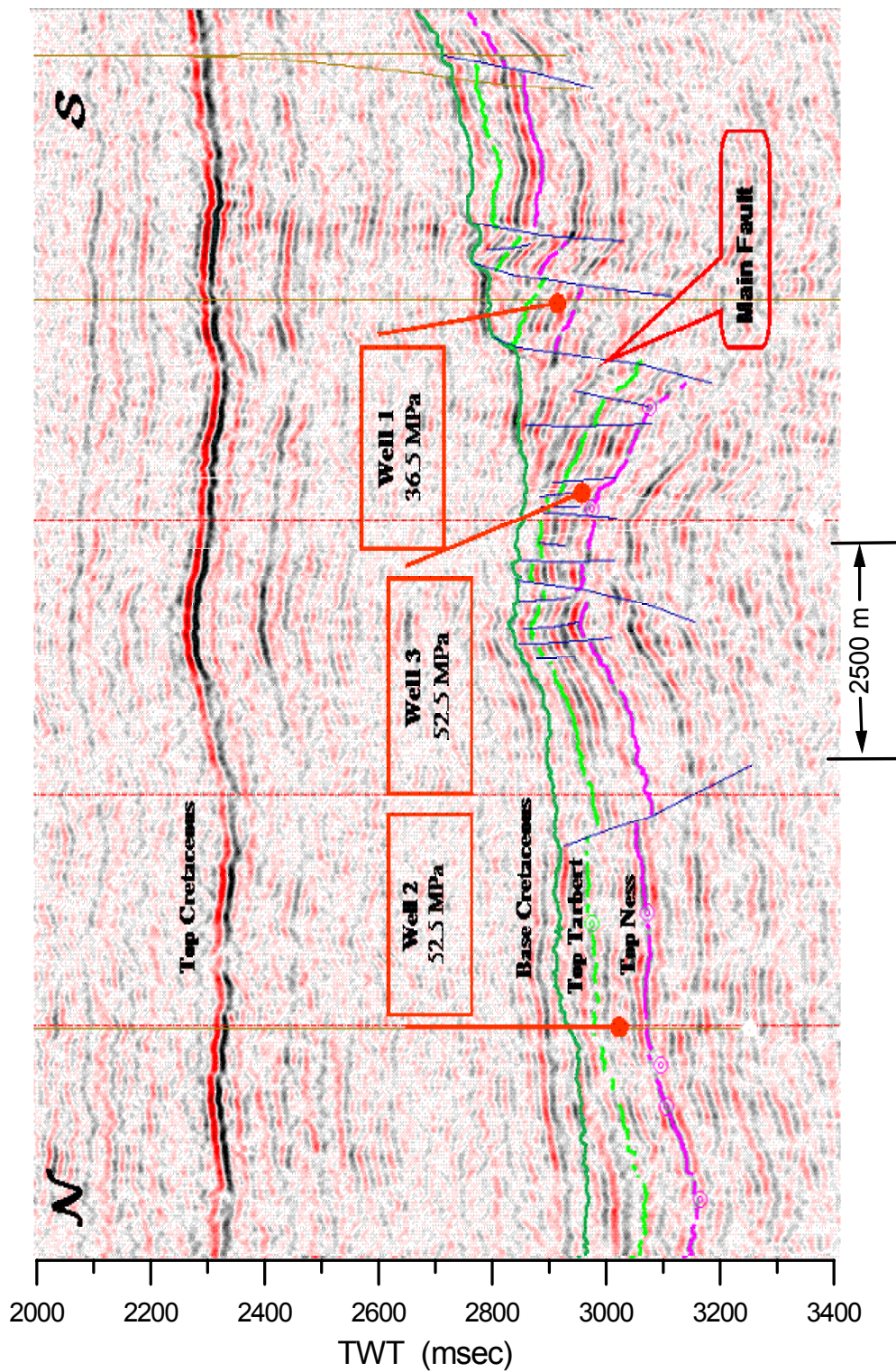


Figure 5.9: Seismic section through Tune wells showing the location of the Tarbert (Top Tarbert - Top Ness interval). The mean reservoir fluid pressures are indicated. The depths of interest are between Top Tarbert (green) and Top Ness (pink).

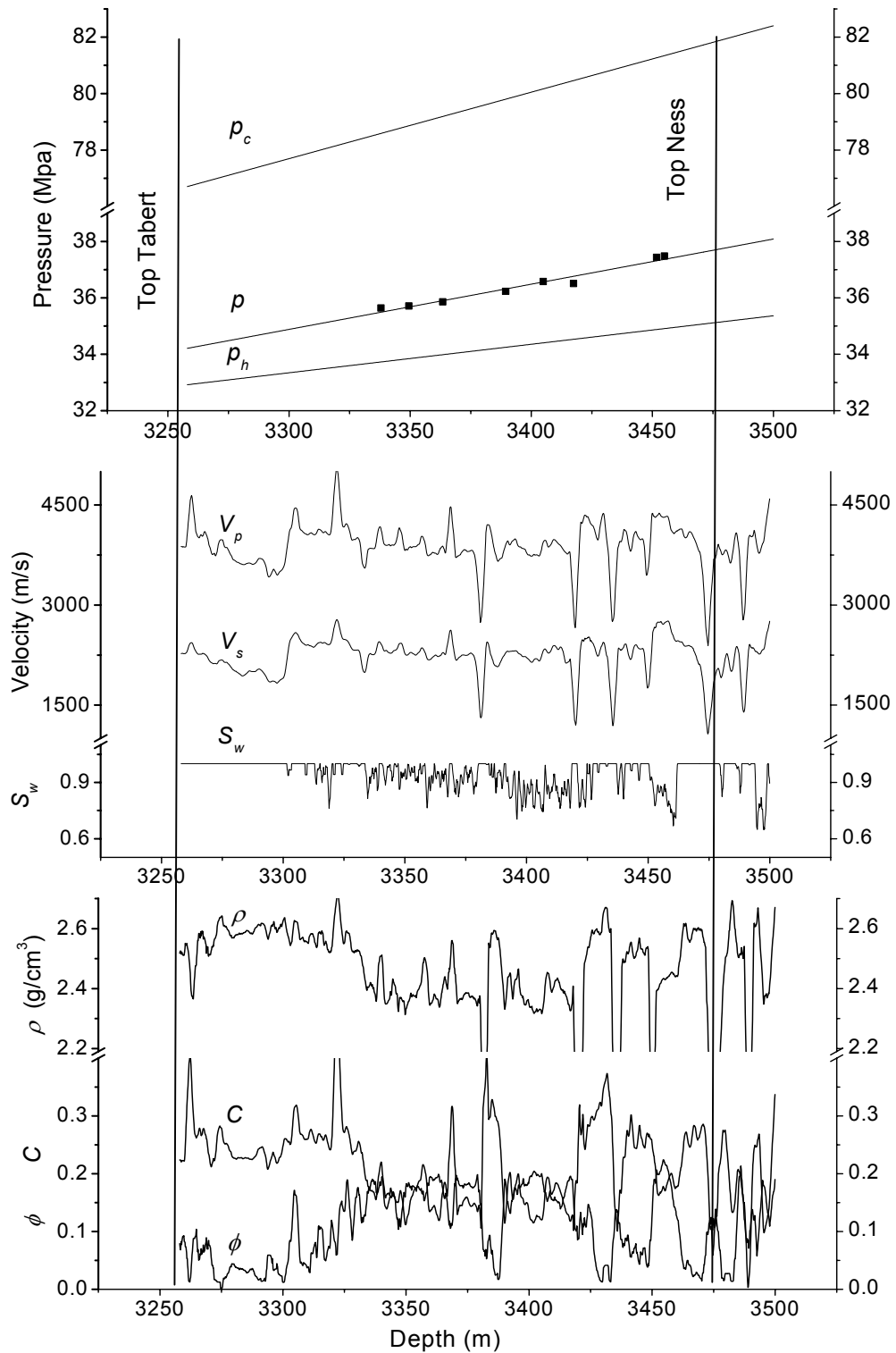


Figure 5.10: Pressure and formation data (porosity ϕ , clay content C , density ρ , water saturation S_w and sonic-log velocities V_p and V_s) for the well 1 (see Figures 5.2 and 5.3 for location).

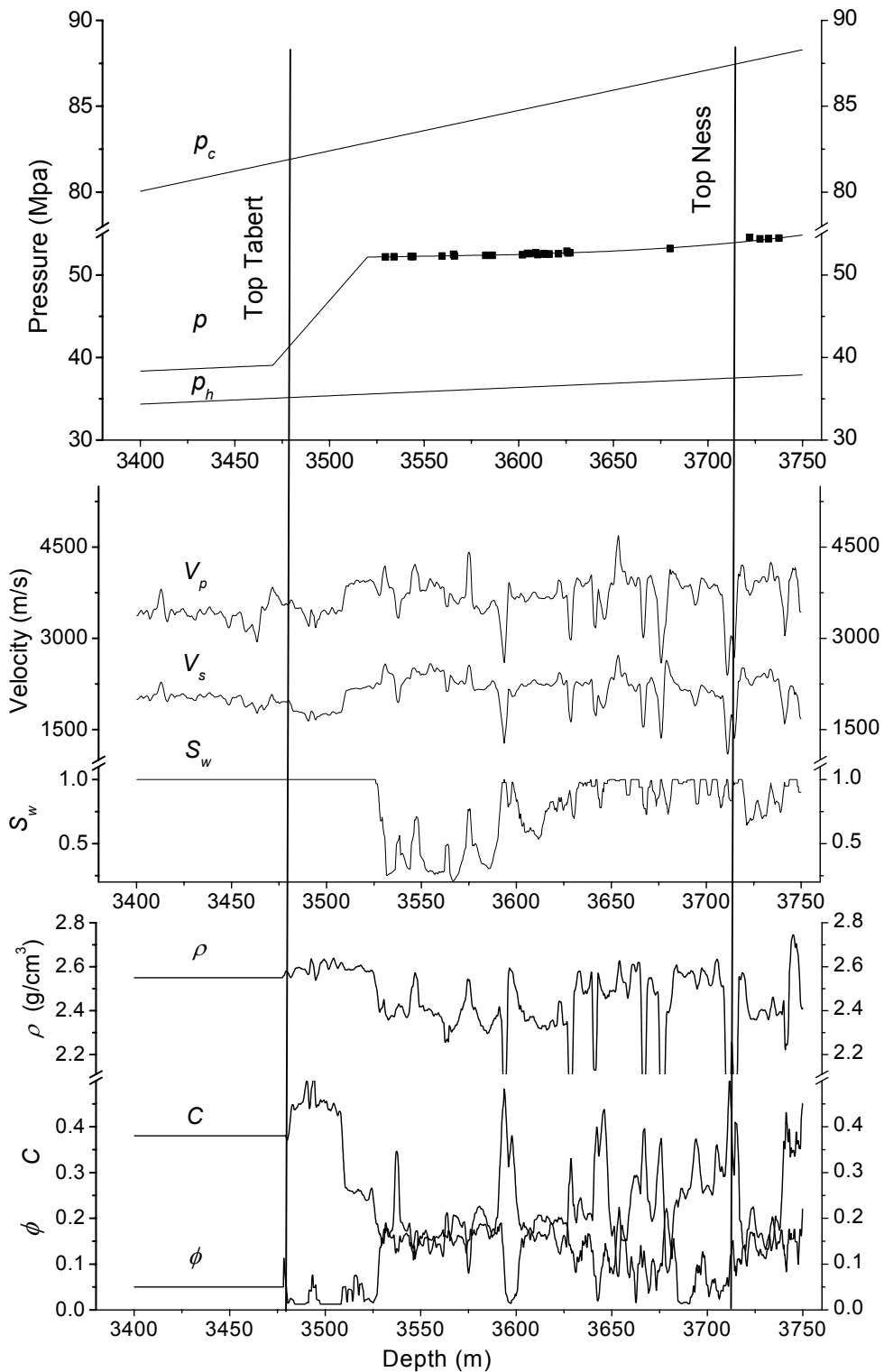


Figure 5.11: Pressure and formation data (porosity ϕ , clay content C , density ρ , water saturation S_w and sonic-log velocities V_p and V_s) for Tune well 2.

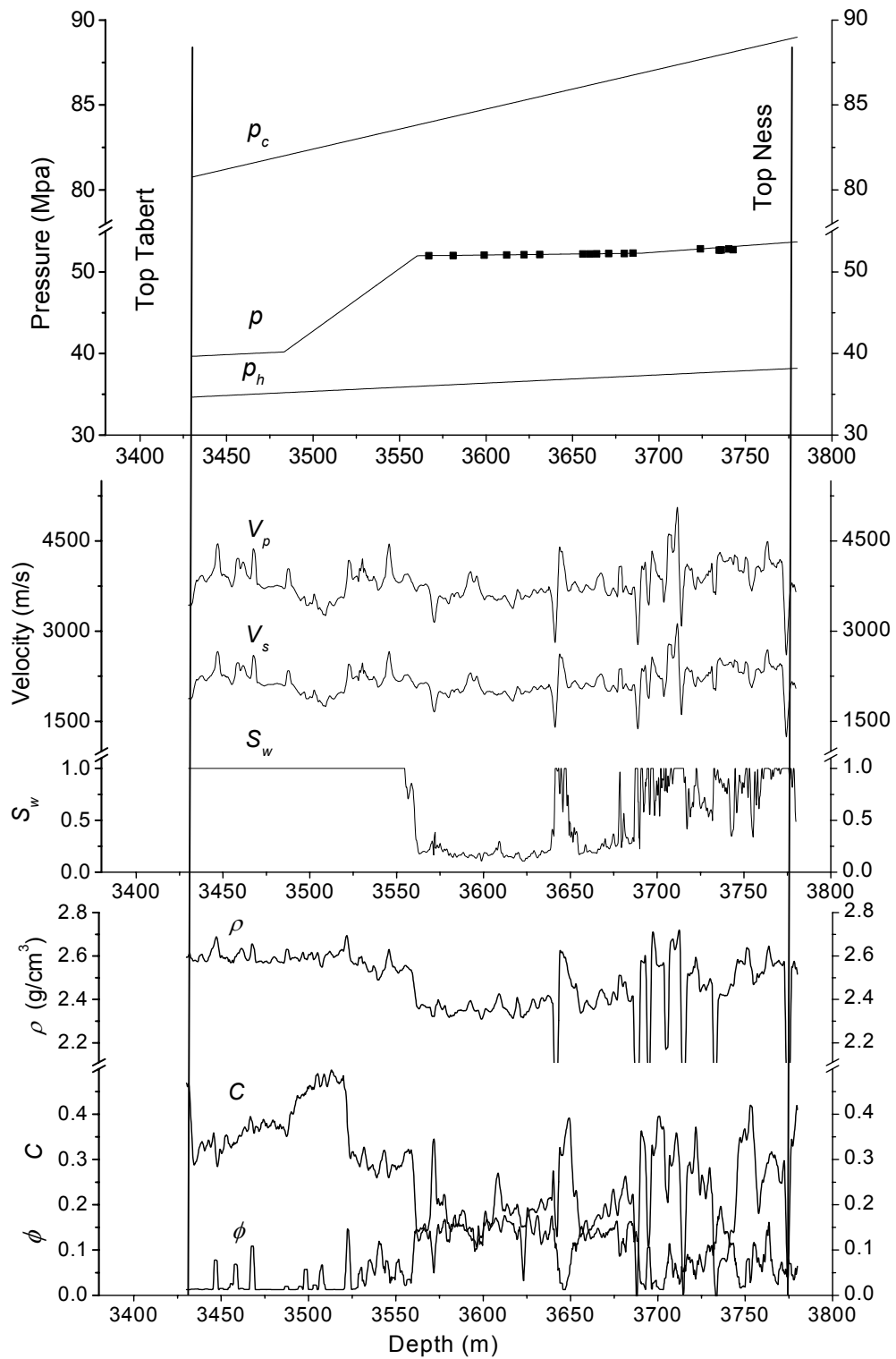


Figure 5.12: Pressure and formation data (porosity ϕ , clay content C , density ρ , water saturation S_w and sonic-log velocities V_p and V_s) for the Tune well 3.

5.4.2 Velocity determination by tomography of depth migrated gathers

Recent advances in depth migration have improved subsurface model determination based on reflection seismology. Subsurface imaging is linked to velocity, and an acceptable image can be obtained only with a highly accurate velocity field. It has been recognised that prestack migration is a powerful velocity analysis tool that yields better imaging results than poststack migration in complicated structures. The basic assumption underlying the velocity determination methods based on prestack migration is that when the velocity is correct, migrated data with different offsets must yield a consistent image.

In order to obtain the velocity field, we use the seismic inversion algorithm described by Koren et al. (1998). Figure 5.13 shows the flow chart of the velocity analysis procedure. We start with an initial model based on the depth converted time model, using a layer velocity cube based on conventional stacking velocities, and the interpreted time-horizons from the Tune project. Line by line, we perform the 3-D prestack migration using the initial velocity model and an appropriate aperture (3 km \times 3 km at 3 km depth) in the 3-D cube.

Through several iteration loops the model is gradually refined in velocity and hence depth. Each loop includes reinterpretation of the horizons in the depth domain, residual moveout analysis and residual moveout picks in the semblance volume. This is performed for each reflector of significance, starting at the seabed and successively stripping the layers down to the target. The tomography considers; 1) an initial velocity model and, 2) the errors as expressed by the depth-gather residual moveout and the associated 3-D residual maps. From these two inputs a new velocity model is derived where the layer depths and layer velocities are updated iteratively in order to yield flat gathers. The refined model is derived using a tomographic algorithm that establishes a link between perturbation in velocity and interface location, and traveltime errors along the common reflection point (CRP) rays traced across the model. CRP rays are ray pairs that obey Snell's law and emanate from points along the reflecting horizon, arriving at the surface with predefined offsets, corresponding to the offset locations for the migrated gathers. Each pair establishes a relationship between the CRP and the midpoint of the rays at the surface. The depth errors indicating the difference in depth of layer images and reference depth are picked on the migrated gather along the horizon and converted to time errors along the CRP rays.

The equations relating the time errors to changes in the model are solved by a weighted least squares technique. The final model consists of seven layers, i.e., the seawater layer, seabed-Top Diapir (clay diapirism is a characteristic feature of the Tertiary throughout the area), Top Diapir-Top Balder, Top Balder-Top

Cretaceous, Top Cretaceous-Base Cretaceous (Cretaceous layer), Base Cretaceous-Top Tarbert, and the target layer, Top Tarbert-Top Ness (Tarbert layer). Figure 5.14 shows the in-line (bottom) and cross-line (top) velocity models, intersecting the gas bearing high-pressured well 3. The velocity maps for Cretaceous, Base Cretaceous-Top Tarbert and Tarbert layers are shown in Figure 5.15, where the well locations are indicated. The Cretaceous layer velocity and the depth to Base Cretaceous reveal a remarkable similarity, i.e. where the Cretaceous is deep, the velocity is high, and where the Cretaceous is shallow, the velocity is low, indicating that the velocity of Cretaceous is essentially governed by the overburden (e.g. compaction). Whereas the structural features about Base Cretaceous are fairly smooth the geometry at Base Cretaceous and below is more dramatic as also apparent from the seismic section (Figure 5.9). In the northwest flank, the Base Cretaceous-Top Tarbert and Tarbert layers terminate against the regional fault plane. Also along the most significant local fault planes the layers are not defined, and hence the discontinuity in the velocity maps. Structural features are well displayed in the velocity maps of the Base Cretaceous-Top Tarbert and Tarbert layers. The Base Cretaceous-Top Tarbert velocity map reveals, however, a fairly scattered distribution, with small patches of highs and lows within the main fault blocks. For the reservoir itself, as represented by the Tarbert velocity map, the distribution is far more coherent. In the Tarbert Formation at wells 2 and 3 in the North fault block, there are consistently lower velocities than those at well 1 in the East block. This feature is fairly constant for several independent velocity analyses, with a velocity increase of about 200 m/s across the fault separating the gas-bearing reservoir in the North block from the water-bearing reservoir in the East block. A high-velocity ridge separates the lows at well 2 and 3. Distinct low-velocity zones are also seen to the south and south-east that are not correlated with the depth variations. On the other hand, the high-velocity zones in the south-west may be related to the Tarbert dipping down at the western flank. Table 5.1 shows the sonic velocities and the results of seven independent velocity analyses obtained in the three well locations, where the standard deviation indicates the error in the estimation. There are many factors (e.g., dip, raypath bending, short-spaced velocity changes and anisotropy) that has impact on the accuracy of the velocity estimates (e.g., Fagin, 1998), but the best approach to estimate resolution is to perform the test on the data at hand, as shown in table 5.1. Maximum difference between mean value of sonic velocity and tomography velocity is $\sim 1.8\%$ at well 1.

5.4.3 Application of the velocity model for pressure prediction

In order to estimate the pressure map in the Tarbert Formation, we follow the procedure described in section 5.2.5. Table 5.2 shows the values of the basic physical quantities used to compute the theoretical velocities. Calibrating with the data from Tune wells we obtained the empirical parameter of Krief et al.; $A = 3.15$ ($F_\mu = 1$). The three-phase Biot-type model (Pham et al., 2002c; see chapters

2, 3, and 4) was applied, excluding viscoelastic effect. The bulk density $\rho = 2.4 \text{ g/cm}^3$ is used to estimate the confining pressure (eq. 5.1). Here, well 1 (the normal pressured well) was used for calibration of the n -factors. Figure 5.16 shows the effective stress coefficients as a function of differential pressure, obtained for wells 1 and 2. We assume that $n_0 = 1$, i.e., that at zero differential pressure the frame bulk modulus vanishes. The same assumption has been used for the effective stress coefficient related to the frame rigidity modulus. With this assumption, the model requires only well 1 for calibration and the others wells can be used for checking the results. Figure 5.17 shows the velocity map (bottom) and the overpressure map assuming $S_w = 0.35$ and a gas saturation $S_g = 0.65$ (middle). The picture at the top represents the difference in pore pressure by assuming gas-bearing Tarbert (the middle picture) and water-bearing Tarbert ($S_w = 0.94$ and $S_g = 0.06$). An overpressure of about 15 MPa is predicted for well 2, while slightly higher overpressure (18 MPa) is predicted for well 3. Direct measurements indicate overpressures of about 15 MPa (see Figure 5.10, 5.11, and 5.12). Figure 5.17 (top) shows that the sensitivity of the model to fluid saturation is about 2.5 MPa. From the results in Figure 5.17 we may conclude that the three wells are drilled in three isolated pressure compartments. Although the pressures in wells 2 and 3 are similar, the apparent high velocity zone between those wells indicates the existence of an isolated compartment with lower pressure. A closer inspection of the faults in Figure 5.8 and 5.9 may support this interpretation.

Tomography	Well 1	Well 2	Well 3
1	4034	3883	3842
2	4025	3785	3825
3	4012	3777	3806
4	4004	3780	3791
5	3986	3797	3804
6	4012	3772	3803
7	4019	3782	3760
Mean	4013	3797	3804
St. Deviation	15	39	26
Sonic P-wave	3948	3735	3799

Table 5.1: Statistics of Tarbert tomography P-wave velocities (m/s) at the well locations and comparison with sonic velocities.

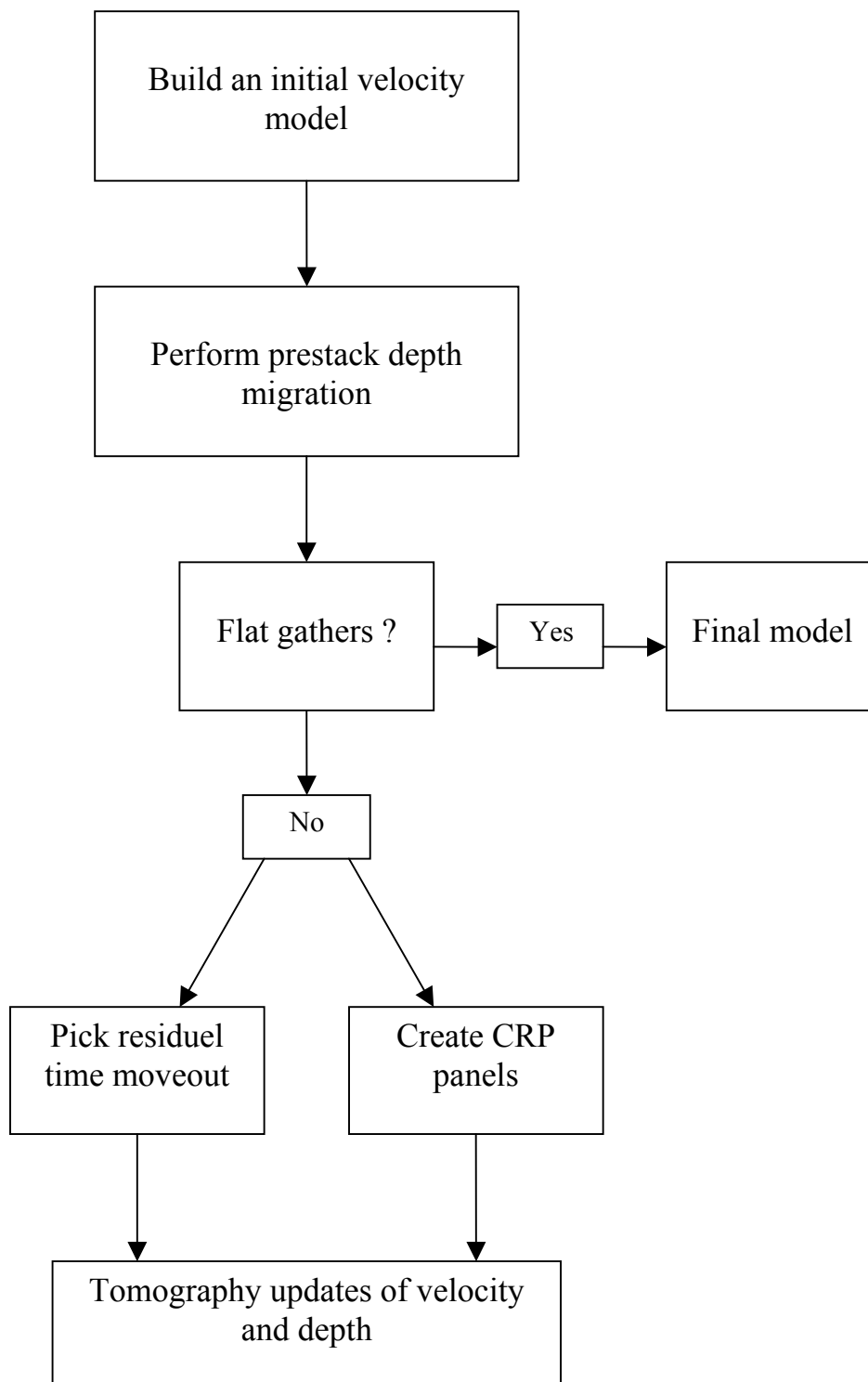


Figure 5.13: Reflection tomography flow chart.

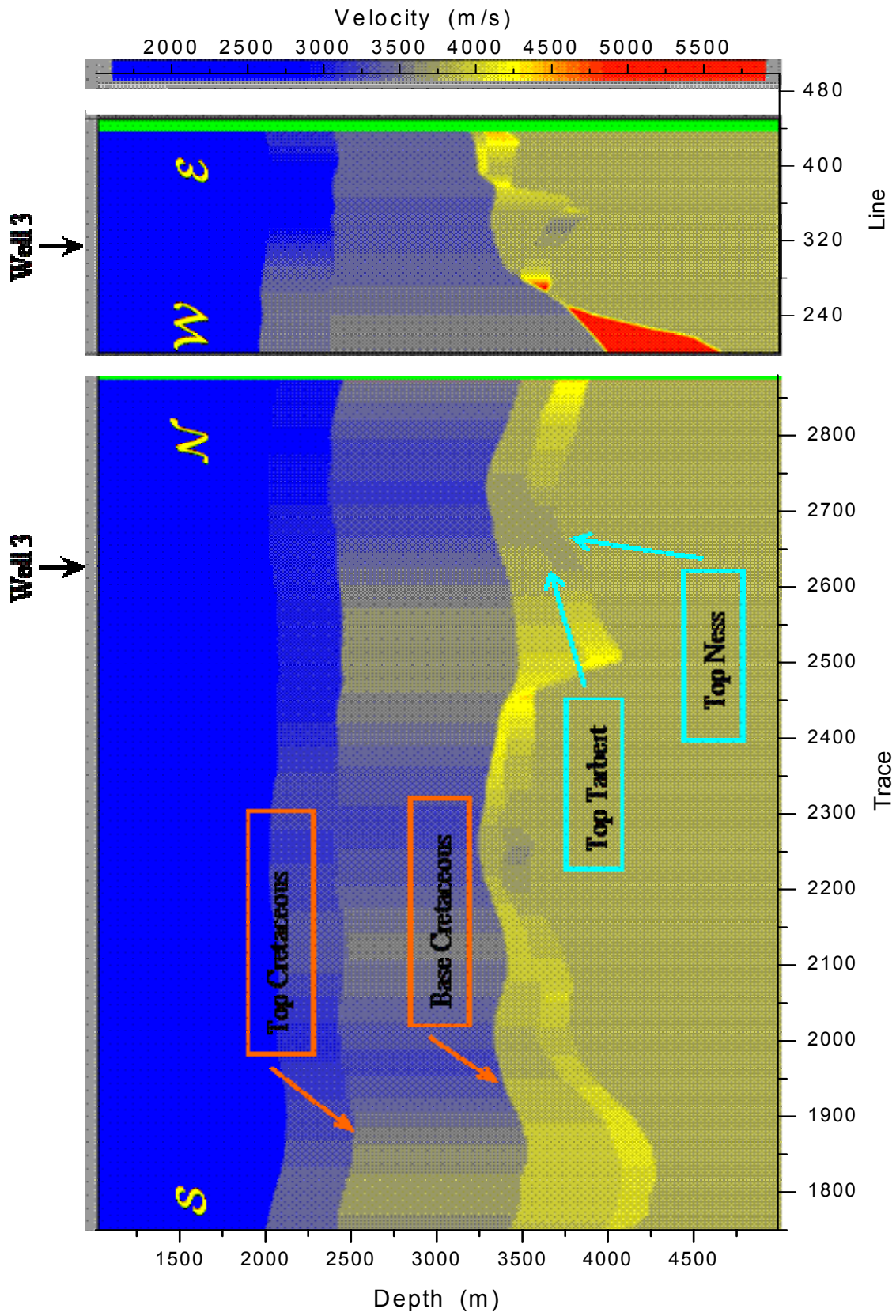


Figure 5.14: In-line (bottom) and cross-line (top) velocity models, intersecting the gas bearing high-pressure well 3.

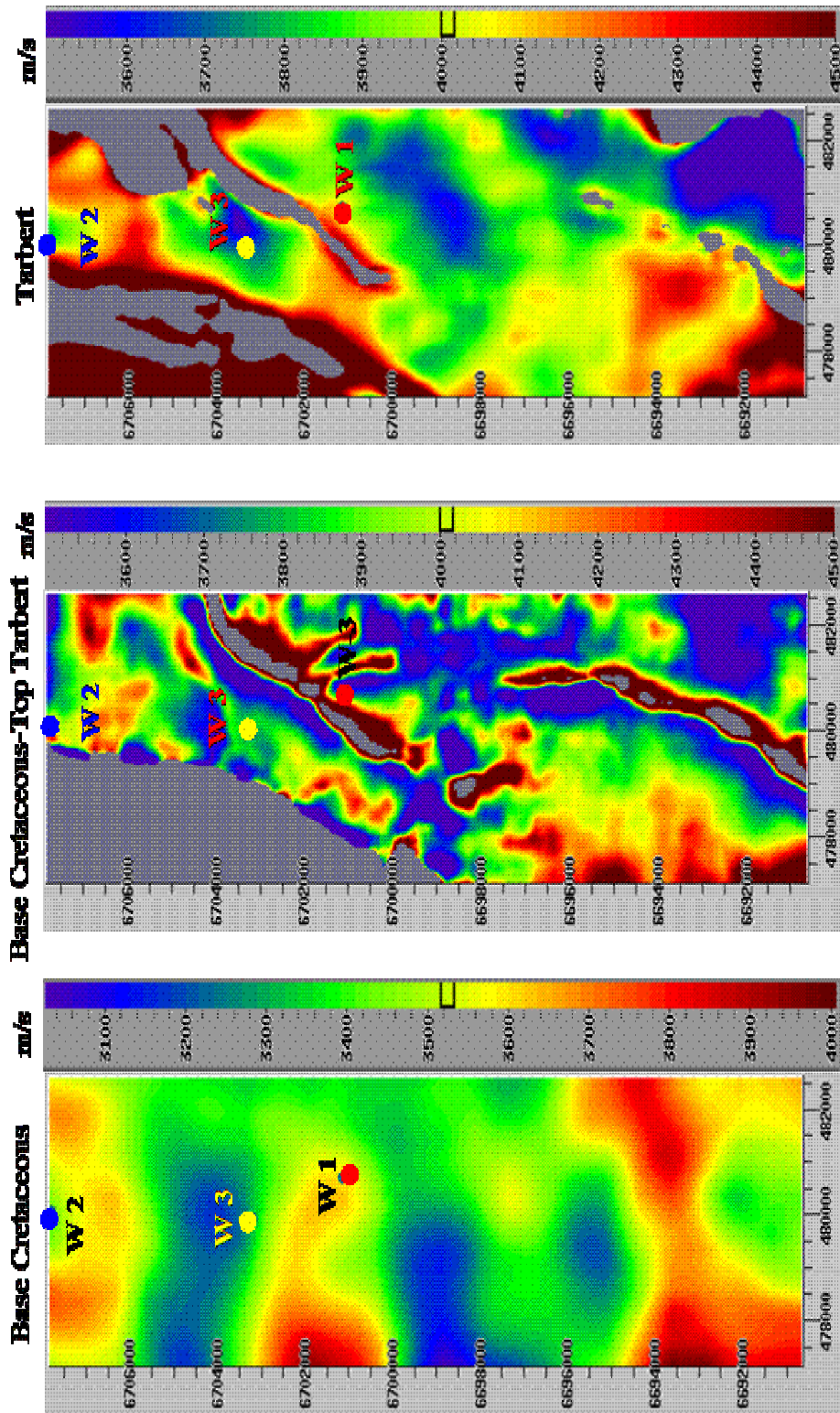


Figure 5.15: Velocity maps for Top Cretaceous to Top Ness layers with individual colour scale given in m/s. The velocity map represents the velocity of the layer between the given reflector and that above. The target for this study is the Tarbert Formation.

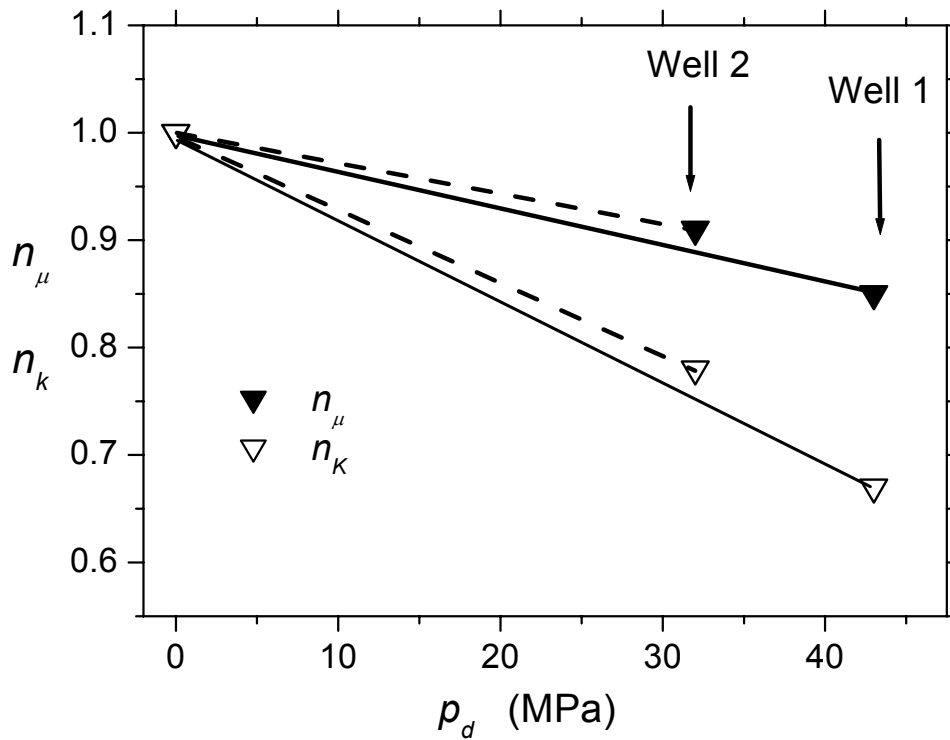


Figure 5:16: Effective stress coefficients as a function of differential pressure p_d .

Solid grain	bulk modulus, K_s	39 Gpa
	shear modulus, μ_s	33 Gpa
	density, ρ_s	2650 kg/m ³
	average radius, R_s	50 μm
Clay	bulk modulus, K_c	20 GPa
	shear modulus, μ_c	10 GPa
	density, ρ_c	2650 kg/m ³
	average radius, R_c	1 μm
Fluids	bulk modulus, K_w	2.4 GPa
	density, ρ_w	1.798 cP
	viscosity, η_w	0.01 GPa
	bulk modulus, K_g	1030 kg/m ³
	density, ρ_g	100 Kg/m ³
	viscosity, η_g	0.02 cP

Table 5.2: Material properties of the clay-bearing sandstone.

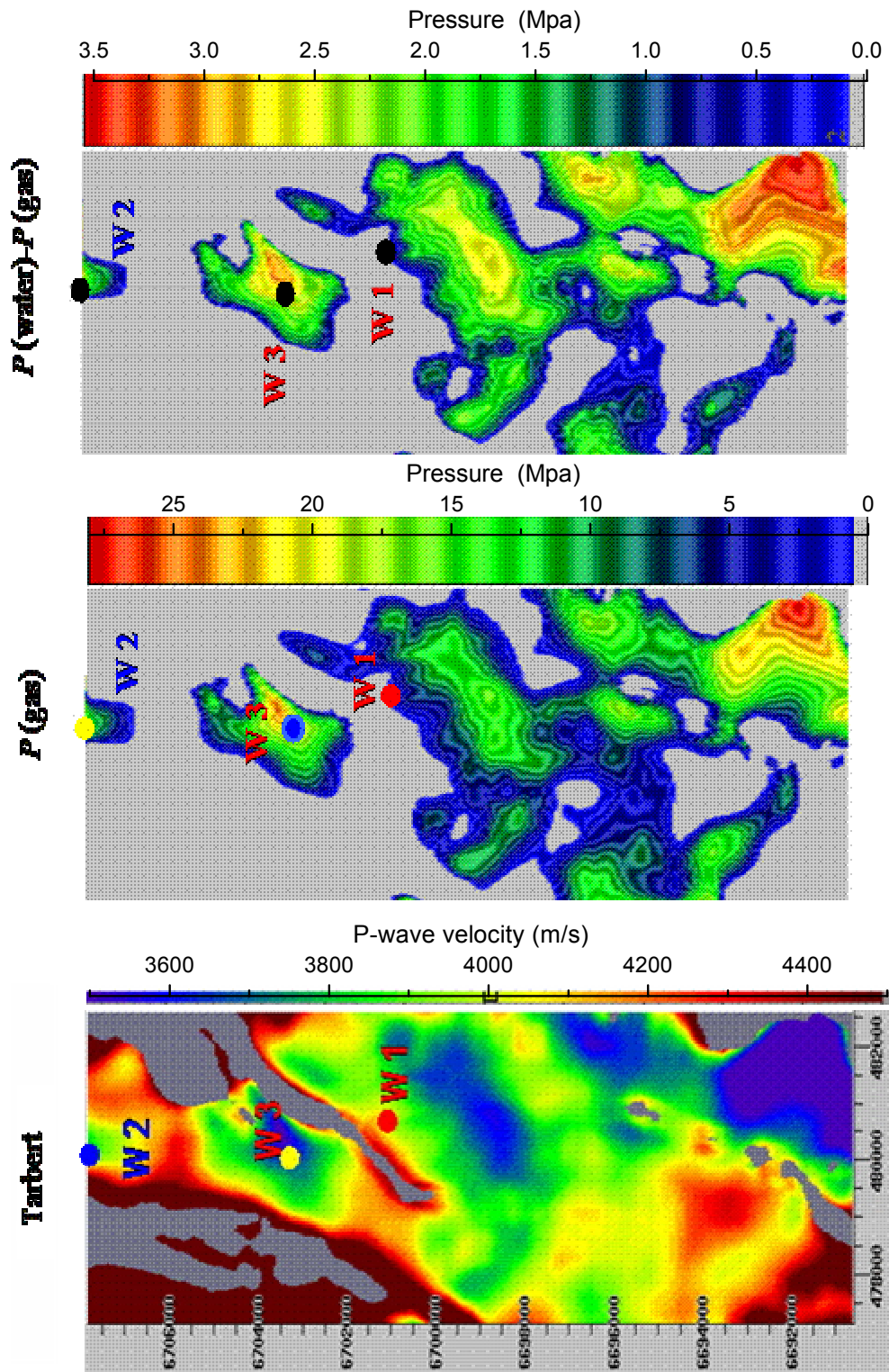


Figure 5.17: Seismic velocity map (bottom), overpressure prediction (middle) and difference in overpressure due to gas-bearing Tarbert and water-bearing Tarbert (top).

5.5 Discussion and conclusions

We have developed a model of the acoustic properties - wave velocity and quality factor - of shaley sandstone, which are not only functions of clay content, partial saturation, frequency, but also of pore pressure. Unlike previous theory, by combining the (modified) model of Krief et al. (1990) and the exponential law for dry rock moduli, we are able to obtain the dry bulk and shear moduli of the rock as functions of porosity, clay content, pressures and also of rock texture. The limitation in using exponential function is that the pressure prediction is less accurate when p_d is close to zero for a well-consolidated rock (as discussed in section 5.3).

The model reveals a strong decrease of the velocity and Q -factor with decreasing differential pressure (or increasing pore pressure). This effect is mainly because the dry-rock moduli are sensitive functions of the effective pressure. The effect of pressure on velocities depends also on porosity. A low porosity induces more stiffness of the rock, and therefore, gives rise to a smaller effect of pressure on the wave responses (velocities). In general, the model shows an effect of pressure on wave responses that has good agreement with physical theory and with experimental data (Christensen and Wang, 1985; Berryman, 1992).

The model has been applied to the Tune field in the Viking Graben sedimentary basin of the North Sea. Here, the velocity obtained by careful analysis of prestack 3-D data from the deep and complex Tarbert reservoir in the Tune field is sufficiently sensitive to pressure and pore fluid to perform a meaningful analysis. The velocity and pressure distribution complies well with the structural features of the target and the general geological understanding of the pressure compartments in the Tune field. The partial saturation model used for pressure prediction can conveniently be calibrated against well data, provided that a complete set of logging data is available for the zone of interest. The most important part of the prediction process is the determination of the effective stress coefficients and dry-rock moduli versus effective pressure, since these properties characterise the acoustic behaviour of the rock. The inversion method based on the shaley sandstone model must fix some parameters while inverting for others. For instance, assuming the reservoir and fluid properties (mainly, the saturation values), formation pressure can be obtained by inversion. Conversely, assuming the pore pressure, the saturation can be obtained. The latter implies that this method may be used in reservoir monitoring where the pressure distribution is known while saturation, i.e., the remaining hydrocarbon reserves, are uncertain. We have neglected velocity dispersion, which is not easy to take into account, since Q -factor measurements are difficult to obtain with enough reliability. When using laboratory data for the calibration, the effect of velocity dispersion can be significant (Pham et al., 2002c).

Chapter 6

Numerical experiments-Velocity and attenuation in partially saturated rocks

6.1 Introduction

The primary goals of seismic exploration are the identification of the pore fluids and the mapping of hydrocarbon deposits. In the area of hydrocarbon reservoir management the recent developments in borehole acoustic measurements and seabed geophones make it feasible to conduct high-resolution surveys to detect pockets of unswept reserves, and to monitor the progress of enhanced recovery by gas and liquid injection. Understanding the physics of elastic waves in porous rocks partially filled with gas and liquid is thus important for exploring and exploiting hydrocarbon reservoirs.

Microstructural properties of reservoir rocks and their in-situ rock conditions can be obtained, in principle, from seismic properties, such as travel times, amplitude information, and wave polarisation. In particular, although it is known from the early 80s that the dominating mechanisms of wave attenuation are oscillating flow of the viscous pore fluids and grain boundary friction (e.g., Winkler and Nur, 1982), the use of attenuation to characterise the rock properties is still under-exploited.

Regions of non-uniform patchy saturation occur at gas-oil and gas-water contacts in hydrocarbon reservoirs. Also, during production gas may come out of solution and create pockets of free gas. When laboratory measurements and sonic logs are used to infer the behaviour of acoustic properties at seismic frequencies, the frequency dependence of these properties is a key factor. As demonstrated by White (1975), wave velocity and attenuation are substantially affected by the presence of partial (patchy) saturation, mainly depending on the size of the gas pockets (saturation), frequency, permeability and porosity of the rocks.

Patchy saturation effects on acoustic properties have been observed by Murphy (1984), and Knight and Nolen-Hoeckesma (1990). Cadoret et al. (1995) have observed the phenomenon in the laboratory in the frequency range 1-500 kHz. Two different saturation methods result in different fluid distributions and produce two different values of velocity for the same saturation. Imbibition by depressurisation produces a very homogeneous saturation, while drainage by drying produces heterogeneous saturations at high water saturation levels. In the latter case, the experiments show considerably higher velocities, as predicted by White's theory (White, 1975). The experimental results of Yin et al. (1992) display consistent peaks in resonance attenuation (sonic range) at high water saturation. A strong dependence on the saturation history is evident, with the attenuation peak located at 90% water saturation in the drainage experiment, and 98% water saturation for imbibition techniques. Similar results are reported by Bourbié and Zinszner (1984) at 500 kHz and Cadoret et al. (1998) at 1 kHz.

A number of theories have predicted the effects of fluids on attenuation and seismic velocities at full saturation (e.g. Biot, 1962; O'Connell and Budiansky, 1977) while fewer theories address partial saturation (e.g. White, 1975). Although attenuation still remains poorly understood, and underexploited, it is believed by many investigators that in the seismic and sonic-frequency range (10 Hz–20 kHz) the dominating mechanisms of wave attenuation are oscillating flow of the viscous pore fluid and the grain boundary friction (Winkler and Nur, 1979; 1982). The role of pore fluid in controlling the velocity was well established in the low-frequency (seismic) limit by Gassmann (1951), and for ultra-sonic frequencies (0.5 MHz and above) by the experimental studies of Gregory (1976), Domenico (1977) and others. The few published results obtained in the sonic-frequency band (1-20 kHz), e.g., by Murphy (1984) and by Cadoret et al. (1995) are usually in relatively good agreement with the Gassmann model. For higher frequencies (50 kHz and above) the velocity versus water saturation relationship is more complex and strongly depends on rock type and porosity (Gregory, 1976). Heterogeneity of the rock material (Lucet and Zinszner, 1992) and fluid distribution (Cadoret et al., 1995; 1998; Endres and Knight, 1989, 1991) seem to be important factors in explaining the observed behaviour of elastic waves at sonic and ultrasonic frequencies.

However, since appropriate analytical expressions for the velocity and attenuation in partially saturated rocks are not at hand we circumvent the theoretical difficulties by using the direct numerical approach. In the present investigation, a more realistic situation is considered, where an arbitrary (general) pore scale fluid distribution is modelled. By using computerised tomography (CT) scans (Cadoret et al., 1995) it is possible to visualise the fluid distribution in real rocks (Figure 6.1). Fractal models, such as the von Kármán autocovariance function (Frankel and Clayton, 1986), calibrated by the CT scans, are used to model realistic fluid distributions. We introduce a numerical rock sample with homogeneous rock

properties, but with alternately uniform and patchy fluid distributions, based on a fractal model utilising the CT scans of Cadoret et al. (1995). From numerical simulations of poro-elastic wave propagation in the frequency range 10-500 kHz, we investigate the effect of varying the fluid distribution patterns and effective saturation. By analysing the recorded wave arrivals, we obtain values of P-wave velocity and attenuation versus effective fluid saturation that are consistent with published laboratory measurements (Yin et al. 1992; Cadoret et al., 1995, 1998; Murphy et al., 1982). Visual inspection of the numerical wavefield reveals that the attenuation of the primary wave can be explained by slow-wave conversion at the saturation heterogeneities. Furthermore, we observe that P-wave velocity and attenuation are sensitive to permeability in partially saturated rocks and show the same behaviour as predicted in White's model (White, 1975). For comparison, we substitute the gas pockets with material inclusions of equivalent seismic contrast, but otherwise the same homogeneous permeability and porosity fully saturated with water. Finally, we include patches of low permeability rock coinciding with the gas pockets, imbedded in a high-permeability water saturated background. Heterogeneities in gas/fluid distribution are shown to be more effective in attenuating the primary wavefield than those of equivalent heterogeneities in rock material and permeability (Helle et al., 2002a, Pham et al., 2002a,b).

We solve the poroelastic equations with an algorithm developed by Carcione and Helle (1999), which uses a 4th-order Runge-Kutta time-stepping scheme and the staggered Fourier method for computing the spatial derivatives. The stiff part of the differential equations is solved with a time-splitting technique, which preserves the physics of the slow quasi-static wave at low frequencies (Appendix B).

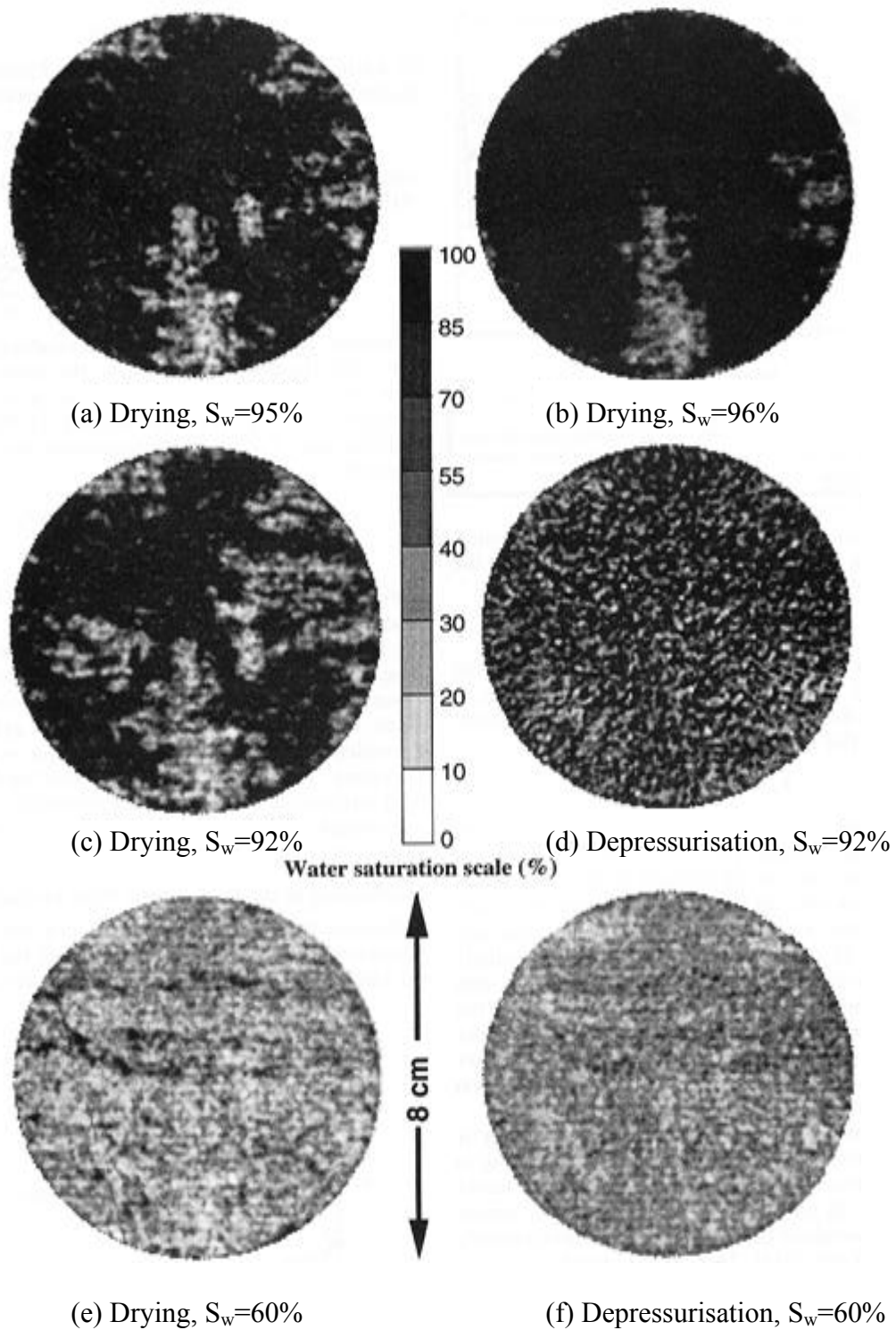


Figure 6.1: Saturation maps obtained with the Estailades limestone sample in different saturation states). The pictures are introduced by using CT scan images, provided by Cadoret et al. (1995).

6.2 Fractals and saturation distribution

Statistically, seismic heterogeneity is often characterised by the so-called von Kármán self-similar correlation function commonly cited in turbulence theory,

$$N(r) = \frac{1}{2^{m-1}\Gamma(m)} \left(\frac{r}{l}\right)^m J_m\left(\frac{r}{l}\right), \quad (6.1)$$

where J_m is a modified Bessel function of order m and Γ_m is the gamma function, r is the (spatial) lag and l is the correlation length. Following Frankel and Clayton (1986) we consider a specific type of von Kármán function where $m = 0$ and then equation 6.1 reduces to

$$N(r) = J_0\left(\frac{r}{l}\right). \quad (6.2)$$

The Fourier transform of the correlation function represents the power spectrum of the fluctuations of the medium. The two-dimensional power spectrum $P(k_r)$ is

$$P(k_r) = \Lambda \frac{l^2}{(1+k_r^2 l^2)^{\nu+E/2}}, \quad (6.3)$$

where $k_r = (k_x^2 + k_z^2)^{1/2}$ is the radial wave number, Λ is a normalisation constant, ν ($0 < \nu < 1$) is a self-similarity coefficient, the fractal dimension D is given by $D = E+1-\nu$, where E is the Euclidean dimension. For a 2-D model (e.g. $E = 2$) D thus lies between 2.0 for very smooth fluctuations and 3.0 for very complex fluctuations. Here, we set $D = 2$ and vary the fractal correlation parameter l to generate models with uniform and patchy fluid distribution, using small values of l for uniform and larger values for patchy fluid distributions.

For modelling the patchy distribution we set the correlation length $l = l_p$ expressed by

$$l_p(S_w) = \gamma_1 + \gamma_2 \exp\left[\gamma_3 (|S_w - 0.5| + 0.5)\right], \quad (6.4)$$

to account for the fact that patches are more pronounced at high and low values of saturation S_w than in the intermediate range. The factors γ_i are estimated from the CT scans, and to estimate the correlation length in the case of a uniform distribution $l = l_u$, we simply determine the ratio l_u/l_p by comparing the corresponding CT images. For model used in this study, we have determined the

following values for the coefficients of equation (6.4): $\gamma_1 = 0.0003$, $\gamma_2 = 6 \times 10^{-7}$, $\gamma_3 = 10$ and $l_u/l_p = 0.3$.

To construct the fluid distribution of a given effective water saturation $S_w \in [0,1]$ on the 2-D numerical grid, we adopt the following procedure: Firstly, a random number generator assigned the value between zero and one, sequentially to each point. The random factor field is then transformed to wave number domain and filtered (multiplied) by equation (6.3) to obtain the desired spectrum, then, transformed back to the spatial domain, and normalised to the interval $P \in [0,1]$. Secondly to obtain effective saturation values for the numerical rock, where each point on the mesh presents pure water or pure gas, we introduce a control number $\Omega \in [0,1]$ such that for each grid point, we assign water if $P < \Omega$ and gas if $P \geq \Omega$. For example, for 100% gas saturation ($S_w = 0$), $\Omega = 0$ and for 100% water ($S_w = 1$), $\Omega = 1$. For $\Omega = 0.5$ we obtain S_w around 0.5, but the exact value remains to be determined by point-counting the grid as done for the CT scans by Cadoret (1995). An example of the resulting distribution of gas and water for uniform and patchy saturation at different saturation, $S_w = 0.2$ and 0.9 are shown in Figure 6.2. In Figure 6.2a grid size is 0.5 mm, fractal correlation length $l_u \approx 0.3$ mm and patch dimension in the range is 1-5 mm. Figure 6.2b shows the same parameters as in (a) but for patchy distribution, fractal correlation length $l_p \approx 0.9$ mm and patch dimension in the range is 1-12 mm.

6.3 Phase velocity and attenuation estimation

Determination of velocity and attenuation is based on the recorded wave arrivals at three equidistant receiver arrays as shown in Figure 6.3. While recordings from R_1 and R_3 are the main data for the analysis, the middle receiver R_2 is used for checking the consistency. The phase velocity obtained in the numerical experiments is computed from the centre of gravity of $|\psi|^2$ versus propagation time, where ψ is the bulk particle-velocity field (Carcione, 1996; see also Appendix B, B-36). More details about this calculation are given in Carcione (2001b, p. 145). The determination of phase velocity in terms of the location of the energy is justified from the fact that for isotropic media and homogeneous viscoelastic waves, the phase velocity is equal to the energy velocity (Carcione, 2001b, p. 99).

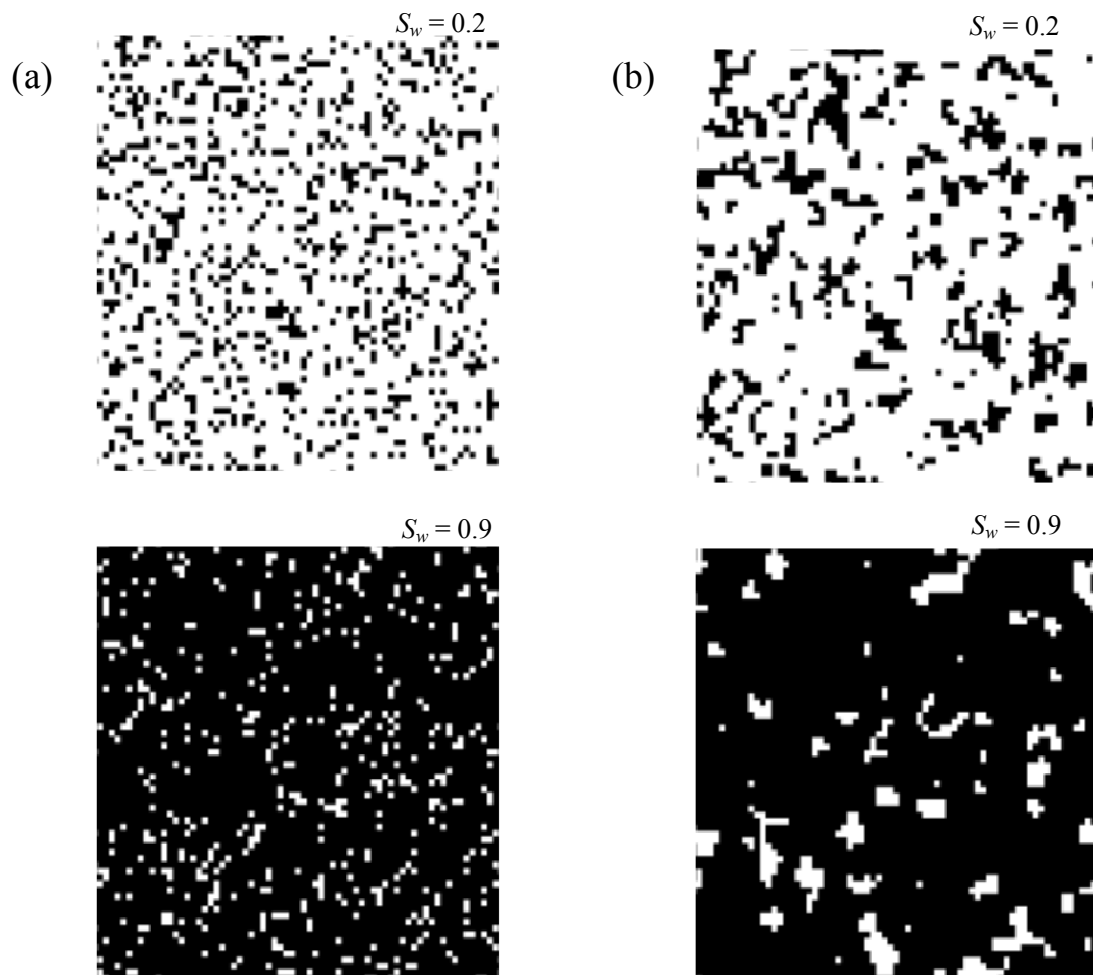


Figure 6.2: a) Examples of uniform distribution of fluid for $S_w = 0.2$ (top) and $S_w = 0.9$ (bottom) in a 68.5×68.5 mm numerical rock sample. Water and gas are indicated by black and white colour, respectively. The same parameters in (b), but for patchy distribution.

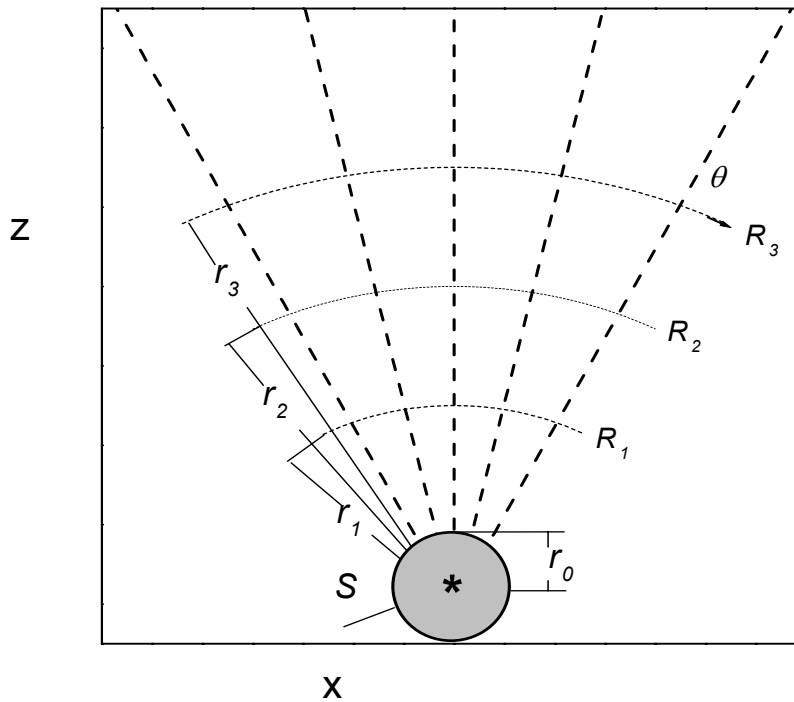


Figure 6.3: Source (S) and receiver (R_i) geometry used for recording the transmitted wavefield. A circular region of radius r_0 surrounding the source is fully water saturated to assure a uniform initial wavefront.

Accurate measurement of intrinsic attenuation is a difficult task since the acoustic waves are strongly affected by scattering due to heterogeneity of the media. The method for estimation of attenuation is based on the analysis of transmissions by comparing the signals recorded for two different distances between the source and receiver. In fact, one of the most reliable techniques for obtaining the attenuation from the recorded signals is by comparing the spectral amplitudes at different frequencies. Because attenuation implies a preferential loss of the amplitude of a wave, the amplitude of the wave at a given frequency f in a distance r from the source can be expressed by (Toksöz et al., 1979):

$$A(f, r) = S_0(f)G(r)e^{-\alpha_p(f)r}, \quad (6.5)$$

where $S_0(f)$ is the source amplitude spectra, $G(r)$ is the corresponding geometrical spreading and α is the attenuation coefficient. The ratio of spectral amplitudes for two different distances r_1 and r_3 along the wave path is therefore given by

$$\ln \frac{A_1(f, r_1)}{A_3(f, r_3)} = \alpha_p(f)[r_3 - r_1] + \ln \frac{G_1}{G_3}, \quad (6.6)$$

Note that index p denotes the (primary) fast P-wave and sometimes is written as $p+$, while $p-$ presents for slow P-wave. It is also known that, the relation of attenuation coefficient and quality factor is defined

$$\alpha_p(f) = \frac{\pi f}{Q_p(f)V_p}. \quad (6.7)$$

For a given source, the width of the frequency spectrum of the transmitted signal is relatively limited, so that Q_p can be considered independent of frequency. Equation (6.7) can be therefore written as a linear function of f ,

$$\ln \frac{A_1(f, r_1)}{A_3(f, r_3)} = \frac{\pi}{Q_p V_p} [r_3 - r_1] f + \ln \frac{G_1}{G_3}. \quad (6.8)$$

The term $\ln(G_1/G_3)$ is independent of frequency, therefore the inverse quality factor Q_p^{-1} can be found from the slope of the line fitted to $\ln(A_1/A_3)$ versus frequency as shown in Figure 6.5. The seismograms of Figure 6.4 show examples of recorded P-waves arrival in three receiver locations R_1 , R_2 , and R_3 for 250 kHz and 500 kHz.

Note that this spectral comparison techniques requires a signal as uncontaminated as possible by other arrivals. For slightly attenuating materials, the spectral ratio method is inaccurate, since the slope of the regression line is too low. Therefore, we carefully picked the window time of the signals as uncontaminated by noise as possible, before transforming to frequency domain for ratio spectral analysis.

In the present study, we estimated velocity and attenuation by estimating the travel time of the bulk particle velocity-field, but we also made some tests by analysing wave-induced bulk pressure. The results show are very similar. In order to obtain optimal results, the velocity and attenuation were estimated by averaging the velocities and attenuation obtained at the set of receivers R_1 , R_3 over five different directions θ (see Figure 6.3).

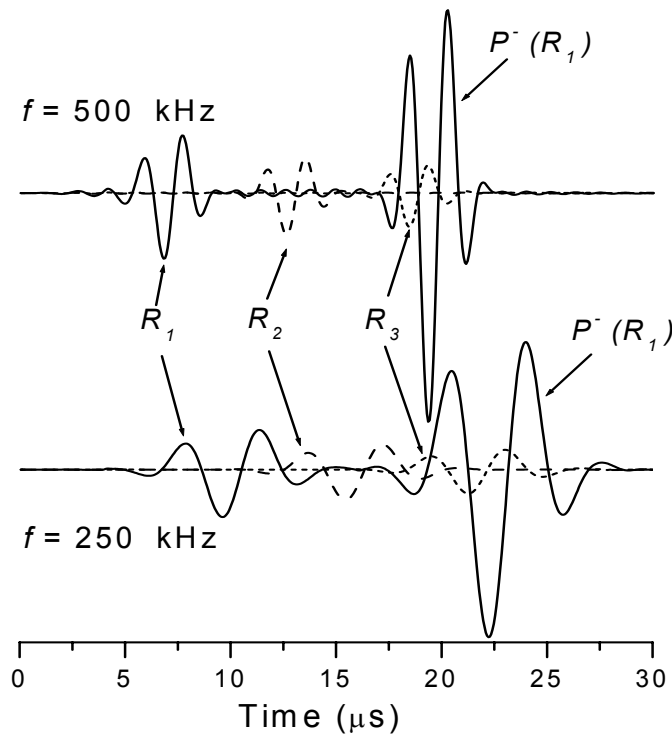


Figure 6.4: Examples of recorded fast P-wave (P^+) arrivals in the three receiver locations R_1 , R_2 and R_3 (Figure 6.3) for 250 kHz and 500 kHz. The slow P-wave (P^-) recorded in R_1 is the dominating event. Rock is fully water saturated ($S_w = 1$).

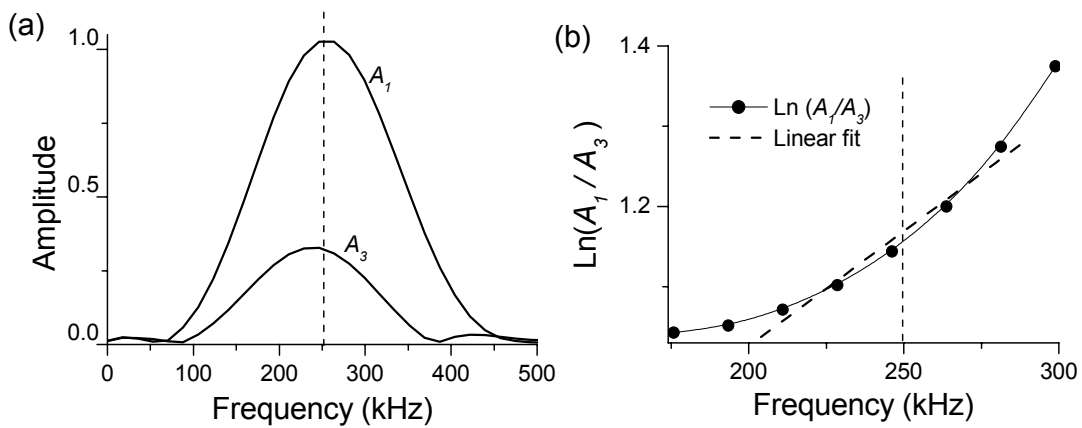


Figure 6.5: Examples of amplitude spectra of the 250 kHz fast P-wave arrivals in the receiver locations R_1 and R_3 (a) and the corresponding spectral ratio (b) for estimating the attenuation.

6.4 Wave simulation and analysis of the wavefields

For analysis of the wavefields, the propagation of wave-induced pressure is normally presented, since the pressure is related to energy loss to the medium (e.g., Mavko et al., 1998, p. 204). By using 2-D poro-elastic model for simulation, the wavefield is obtained in terms of the stress components of the solid (τ_{xx} , τ_{zz} , τ_{xz}) and the fluid pressure (p_f). Therefore, we have to convert the component stresses to the total stress (or bulk pressure).

Following Ben-Menahem and Singh (1981) we write the stress in the form of a tensor and determine the principle directions by

$$\begin{bmatrix} \tau_{xx} & \tau_{xz} \\ \tau_{xz} & \tau_{zz} \end{bmatrix} \Rightarrow \begin{bmatrix} \lambda_1 & 0 \\ 0 & \lambda_2 \end{bmatrix}, \quad (6.9)$$

where λ_1 and λ_2 are eigenvalues, which are the roots of equation

$$\text{Det}[\boldsymbol{\tau} - \lambda \mathbf{I}] = 0 \quad (6.10)$$

The total stress τ_t is also known as the isotropic part of the tensor, given by

$$\tau_t = \frac{1}{2}(\lambda_1 + \lambda_2), \quad (6.11)$$

where the total stress is defined as a weighted sum of solid and fluid pressure (Biot, 1962)

$$\tau_t = p_s + \phi p_f. \quad (6.12)$$

6.4.1 Wave responses in partially saturated rocks

The numerical rock sample is a homogeneous, isotropic Berea-sandstone with a porosity of 24.6 % and permeability of 550 mD (King et al., 2000), partially filled with water and gas. The table 6.1 shows the properties of the different constituents. The numerical simulations were carried out following the procedure explained in section 6.2. Table 6.2 shows the quantified properties of water and gas saturated rocks. Because of the wave attenuation, it is impossible to keep the same mesh length for measurements in difference frequencies. Therefore, four samples with different sizes were considered for experiments with varying frequencies from 10 kHz to 500 kHz. The table 6.3 shows the properties of

different models. In the high frequency cases (250 and 500 kHz), we consider a small block size, $\Delta x = 0.5$ mm to avoid the numerical error, while at 10 kHz, we choose $\Delta x = 2$ mm in order to reduce the run time of simulation. The source is a Ricker-type wavelet applied to the solid skeleton and the fluid phase (a bulk source without shear components). A circular region of radius r_0 (Figure 6.3) surrounding the source is fully water saturated to assure a uniform initial wavefront. Since the source is radially symmetric and the matrix is homogeneous and isotropic, no S-waves energy is generated. The wavefield is computed with a time step Δt varying from 62 to 444 ns within the limits of numerical stability for the grid size used. n_t denotes the number of times step used for simulation. Absorbing boundaries of width, n_a points have been applied at all edges, using a simple exponential damper to prevent wave-field wraparound due to Fourier transformation.

Solid	bulk modulus,	K_s	35 Gpa
	shear modulus,	μ_s	35 Gpa
	density,	ρ_s	2650 kg/m ³
Matrix	bulk modulus,	K_m	9.25 Gpa
	shear modulus,	μ_m	9.25 Gpa
	porosity,	ϕ	0.246
	permeability,	κ	550 mD
	tortuosity,	T	2.5
Water	bulk modulus,	K_w	2.4 Gpa
	density,	ρ_w	1000 kg/m ³
	viscosity,	η_w	1.0 cP
Gas	bulk modulus,	K_g	0.01 Gpa
	density,	ρ_g	100 Kg/m ³
	viscosity,	η_g	0.02 cP

Table 6.1: Material properties.

	Water-filled	Gas-filled
ρ	2244 kg/m ³	2023 kg/m ³
$V_P^+(0)$	3418 m/s	3268 m/s
$V_P^+(\infty)$	3434 m/s	3275 m/s
$V_P^-(0)$	44 m/s	23 m/s
$V_P^-(\infty)$	813 m/s	195 m/s
$f_{\text{peak}}(P^+)$	27.79 kHz	5.56 kHz

Table 6.2: Quantified properties of water and gas saturated media

f (kHz)	$\Delta x = \Delta z$ (mm)	n_x, n_z	n_a	Δt (ns)	n_t	r_0	R_1	R_2	R_3
500	0.5	198	30	62	500	23	28	68	108
250	0.5	198	30	62	500	23	28	68	108
125	1	208	30	124	550	30	32	70	108
100	1	208	30	124	550	30	32	70	108
75	1	420	60	163	850	60	64	172	220
50	1	420	60	163	850	60	64	142	220
10	2	495, 840	120	444	1800	150	152	280	410

Table 6.3: Models desired for numerical experiments, corresponding to different frequencies from 10 khz to 500 khz.

Receivers are located in a fan shaped distribution along five rays, centred at the source (Figure 6.3), distances r_1 , r_2 , and r_3 given in terms of grid points in table 6.3.

Comparison of the wavefields (bulk and fluid pressure) after 300 time steps for the uniform and the patchy model, with $S_w = 0.9$ and $f = 500$ kHz, are shown in Figure 6.6. We identify the primary P-wave front at the top edge of the model and the dominant slow-wave front encircling the source location. In the uniform model, we see cascades of small-scale events displaying the character of scattering diffractions. In the patchy model, we identify the majority of these diffracting events as slow waves generated when the primary P-wave front intersects the fluid discontinuities. The latter is well expressed by the details displayed in Figure 6.6c (right) where the primary P-wave is seen to excite slow waves when intersecting the gas pockets, leaving a cascade of slow waves in its tail. Multiple scattering within the gas pockets also constitute important events affecting the primary wavefield as discussed in more detail by Carcione et al. (2002b). Significant events identified as mode conversion from slow to fast P-waves can also be seen (Figure 6.6c, left). Snapshots at the same instant and with the same models, but for $f = 250$ kHz, are shown in Figure 6.7. Here, the above features are essentially repeated but with twice the wavelength of the former simulation. Moreover, the primary wavefront has travelled a shorter distant during the same time interval as it is apparent in the micro-seismograms of Figure 6.4.

The velocity and attenuation estimated as a function of saturation, for a range of frequencies, are shown in Figures 6.8 and 6.9, respectively. In general, the velocities for the patchy models are significantly higher than those for the uniform models, in qualitative agreement with White's theory (Carcione et al., 2002b). For the lower frequencies range, the values of P-wave velocity are

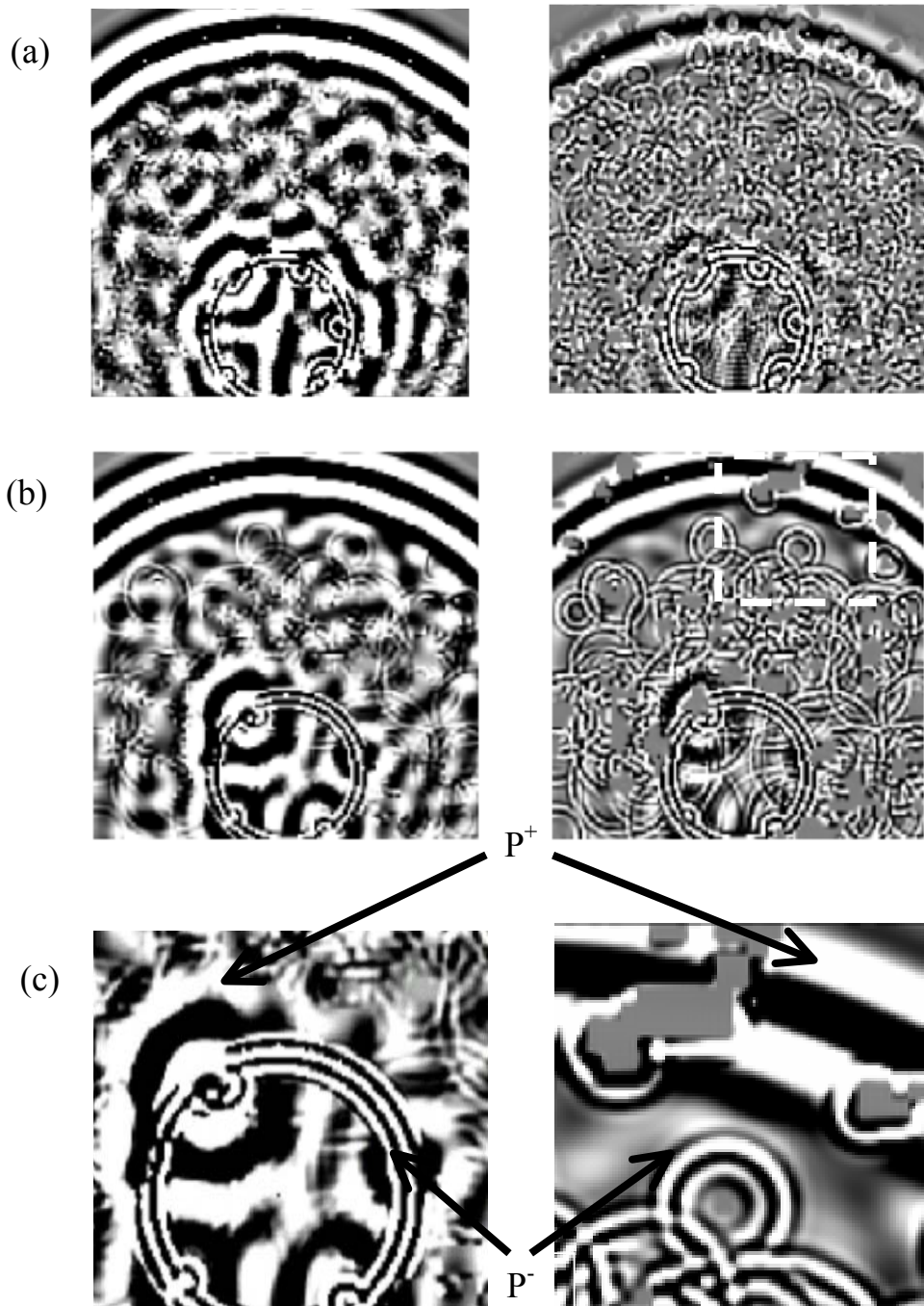


Figure 6.6: Snapshots (68.5×68.5 mm) after 300 time-steps ($18.6 \mu\text{s}$) showing total bulk pressure τ (left) and fluid pressure p (right) for uniform (a) and patchy fluid distribution (b). $S_w = 0.9$, $f = 500$ kHz. Details of fast and slow wave conversions at the gas pockets are shown in (c).

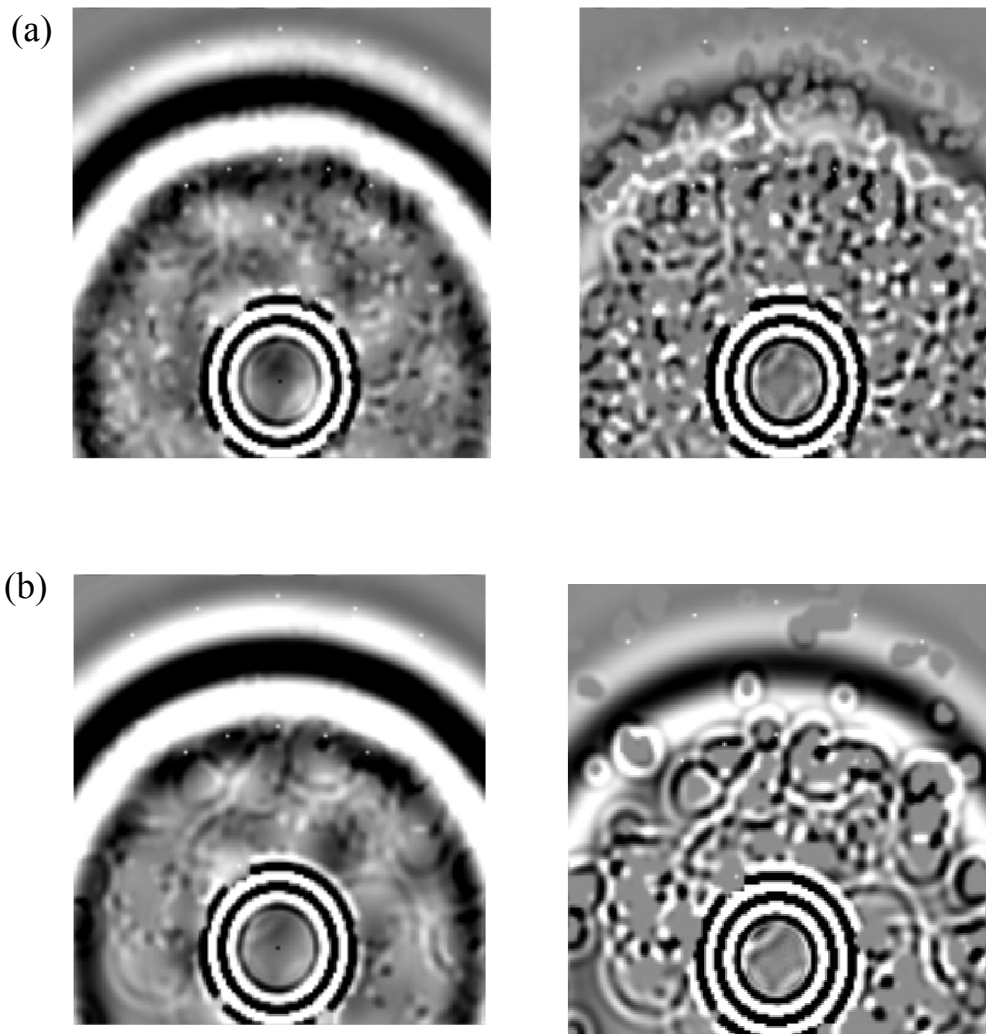


Figure 6.7: Same properties as in Figure 6.6, but for frequency $f = 250$ kHz.

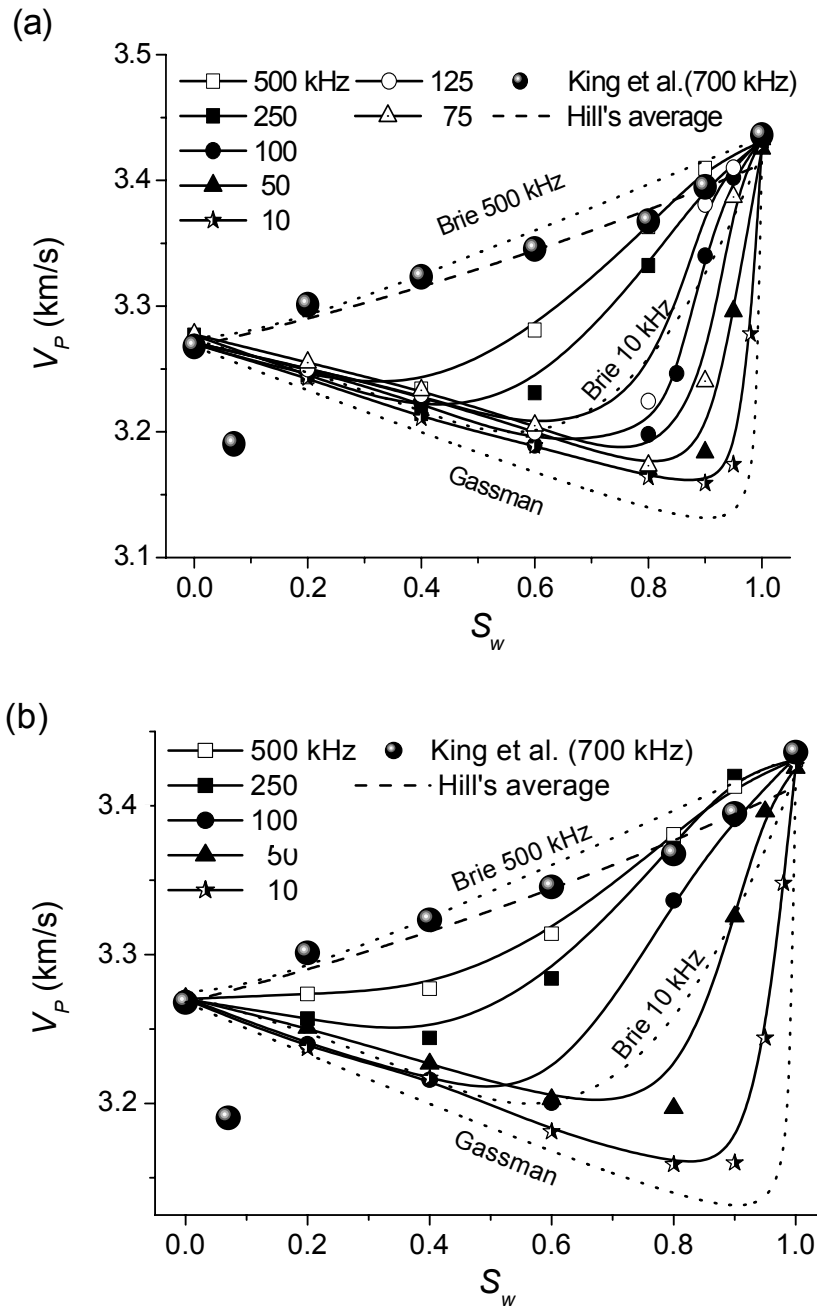


Figure 6.8: V_p versus S_w data as a function of frequency determined from the numerical simulation in uniform (a) and patchy models (b). The models of Gassmann (1951) and the modified Brie et al. (Pham et al., 2002c) and the data of King et al. (2000) are shown for comparison.

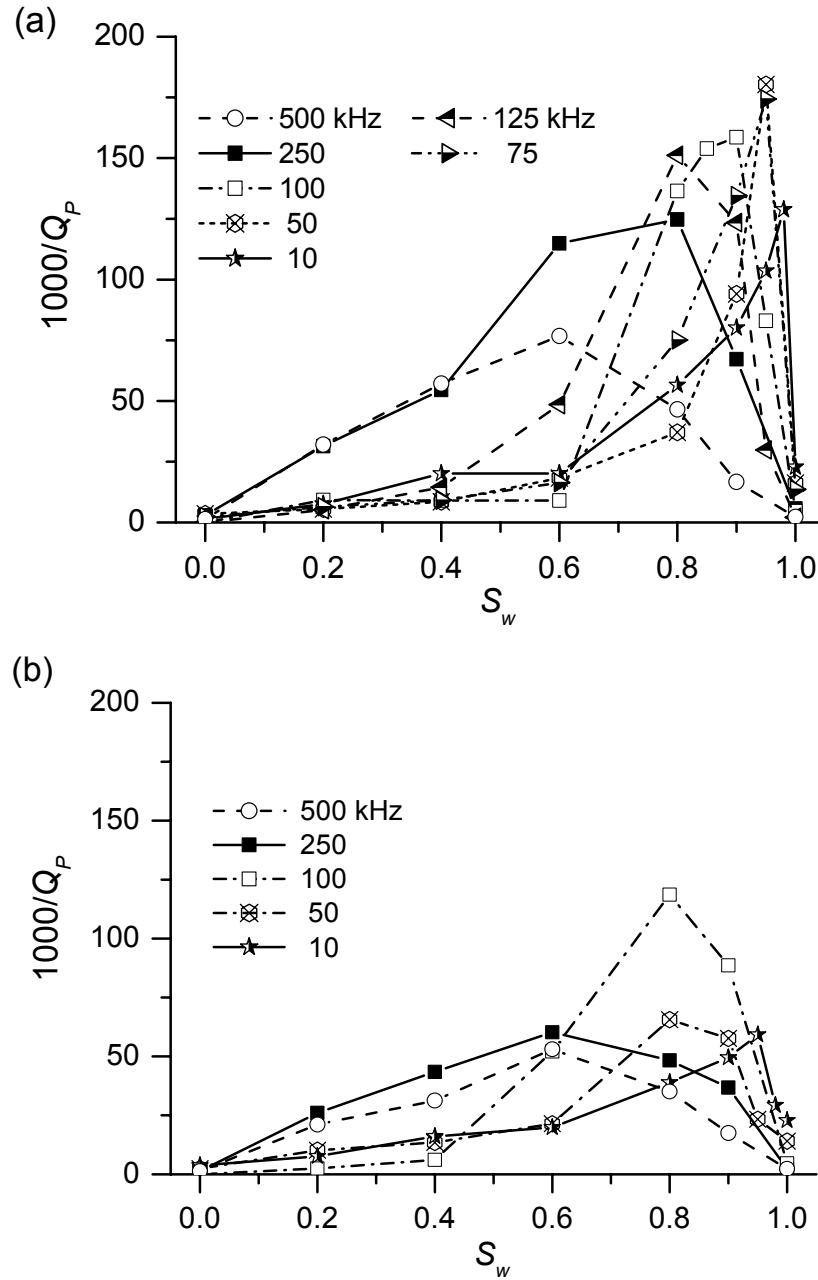


Figure 6.9: Q_P^{-1} versus S_w data as a function of frequency determined from the numerical simulation in uniform (a) and patchy models (b).

slightly above the lower bound (Gassmann; Reuss's average). For the high frequencies, the velocity reaches Hill's average. The modified model of Brie et al. (1995) (eq. 4.11) is also plotted for comparison. In general, behaviour of V_p versus S_w is in fair agreement with the published laboratory data. The initial decline in V_p at low S_w for all frequencies in the case of uniform saturation, agrees with the results in Cadoret et al. (1995). The opposite tendency for patchy saturation at ultrasonic frequencies is also consistent with the observation of Cadoret et al. for Estailades limestone. The result at 500 kHz in the patchy case seem to be closest to the Berea sandstone data of King et al. (2000) and the small mismatch can in general be attributed to the higher frequencies (500 - 700 kHz) applied by King et al..

The results of P-wave attenuation display the characteristic features of published experimental data (e.g., Yin et al., 1992; Murphy, 1982; Cadoret et al. 1998) with low attenuation when the rock is fully saturated with gas or water, and higher attenuation at intermediate values of S_w , and with a peak attenuation when approaching 100% water saturation. In general, Q_p^{-1} in the uniform models is higher than that of the patchy saturation model by a factor of nearly two. The reason for the latter becomes obvious when comparing the different levels of slow-wave intensity apparent from the snapshots in Figures 6.6 and 6.7. Since the quasi-static slow waves dissipate over a much shorter distance than the fast waves (Figure 6.10) and since the slow-waves extract energy from the primary wavefield, this mode conversion constitutes an efficient loss mechanism. Apparently, the more secondary slow waves are generated the greater is the loss of primary P-wave energy. Since the wavelength of slow waves is much smaller (1-15 %) than for the fast waves (1 mm and 7 mm at 500 kHz, 4 mm and 340 mm at 10 kHz), small-scale heterogeneities, far below the wavelength of the fast wave, may be equally important in the loss of the primary wavefield. The population density of saturation heterogeneities thus seems to be the key factor in attenuating the primary wavefield.

As well-known from published laboratory data, attenuation is strongly dependent on water saturation S_w and frequency f . A consistent feature apparent from Figure 6.9 is the shift in the attenuation peaks towards higher S_w with decreasing f . While the 500 kHz wave in the uniform model has its peak attenuation for $S_w = 0.6$, the 10 kHz has its attenuation peak at $S_w = 0.98$. Maximum attenuation occurs for $f \sim [50-100]$ kHz at $S_w \approx 0.95$. Apparently, a resonance phenomenon exists around 100 kHz as shown by the three snapshots of fluid pressure shown in Figure 6.11. Here the small-scale pressure perturbations in the tail of the primary wavefront are insignificant at $S_w = 0.6$ but increase to a high intensity and amplitude at $S_w = 0.9$, indicating remarkably strong pressure variations (and fluid flow) at a scale much smaller than the wavelength of the primary wavefield. Experimentally, such peaks in attenuation are frequently observed. These include peaks in attenuation versus permeability (Klimentos and McCann, 1990; Akbar et

al., 1993), versus frequency and viscosity (Murphy et al., 1986; Vo-thang, 1990), versus porosity (Ogushwitz, 1985) and versus saturation (Winkler, 1979; Murphy, 1982; Yin et al., 1992; Cadoret et al., 1998). Following Carcione et al. (2002b), the relaxation peak (also called critical saturation) is given

$$S_{wc} = 1 - \left(1 + \sqrt{\frac{\kappa K_{E2}}{\pi \eta_2 f a_1^2}} \right)^{-3}, \quad (6.13)$$

where a_1 is the radius of spherical gas pocket and is constant, η_2 is viscosity of water. κ is the permeability and K_{E2} is the effective modulus (more details in chapter 7). In general, the numerical results shown in Figure 6.9 are in good agreement with critical saturation (eq. 6.13). The higher the frequency f , the lower is the critical saturation. Also, the uniform fluid distribution (smaller a_1) gives higher value of critical saturation than in case of patchy distribution.

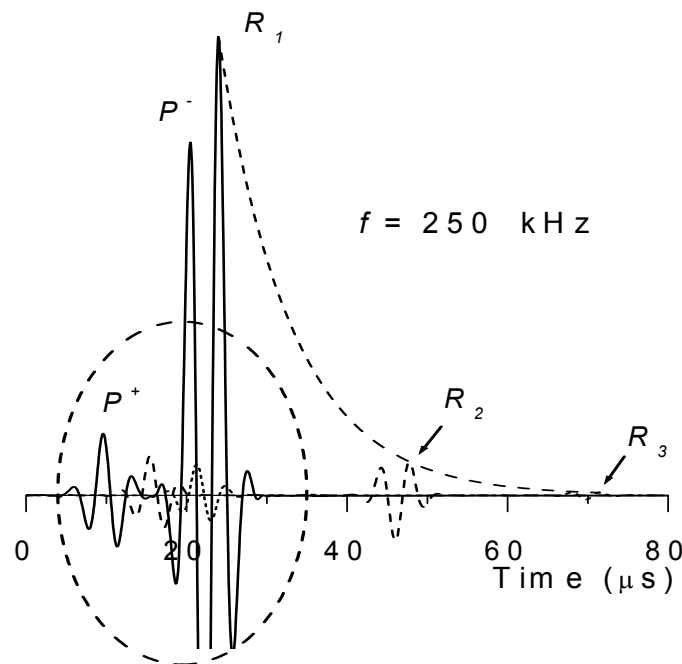


Figure 6.10: Slow wave attenuated during travel time, recorded at different distance.

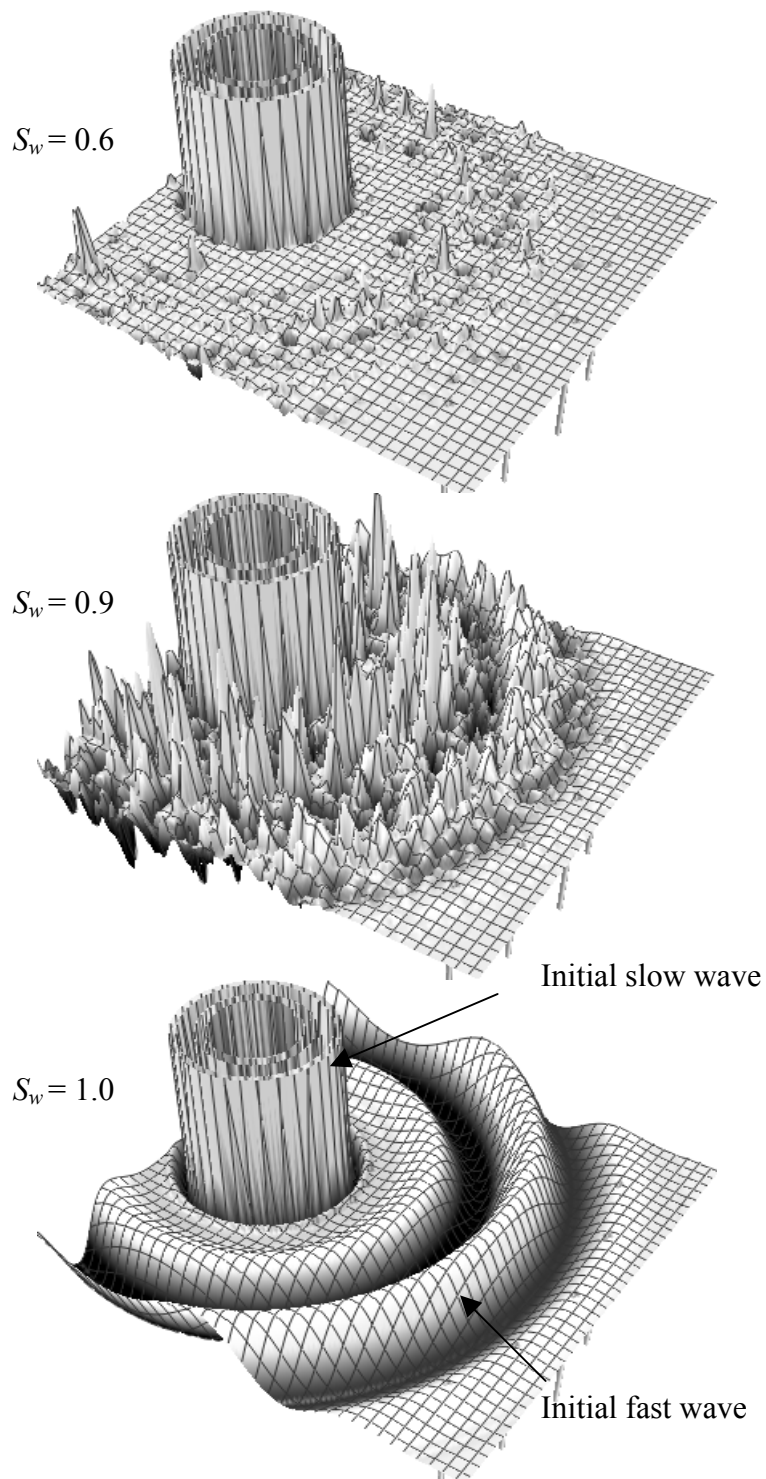


Figure 6.11: Perspective view of low-frequency (100 kHz) snapshots (14.7×14.7 cm) at 300 time steps ($37.2 \mu\text{s}$) showing the fluid pressure p wavefield for uniform fluid distribution with saturation, $S_w = 0.6$, 0.9 and 1.0 .

Figure 6.12 shows velocity and attenuation as a function of S_w and permeability. Here, we fix the frequency at 100 kHz and vary the permeability. The results show a strong response in velocity and attenuation related to permeability in partially saturated rocks, while in fully saturated rocks the permeability sensitivity is insignificant. On increasing the permeability from zero to 550 mD the velocity decreases, while the attenuation increases. The physical explanation is that with increasing permeability the fluid dynamics becomes dominant and the intensity of diffusive slow wave generation from fast P-wave increases, thus contributing more velocity dispersion and higher dissipation of the wave field. Moreover, with an increase in permeability, the attenuation peak (relaxation peak) seems to move toward higher water saturation, which is in good agreement with the critical saturation (eq. 6.13). Following Marko et al. (1998, p. 207) the critical fluid-diffusion relaxation-scale is proportional to the square root of the ratio of permeability to frequency. More details of the relaxation peaks corresponding to saturation, frequency, permeability and heterogeneity in partially saturated rocks will be discussed in chapter 7, where we compare the numerical results based on Biot's theory with the model of White (1975).

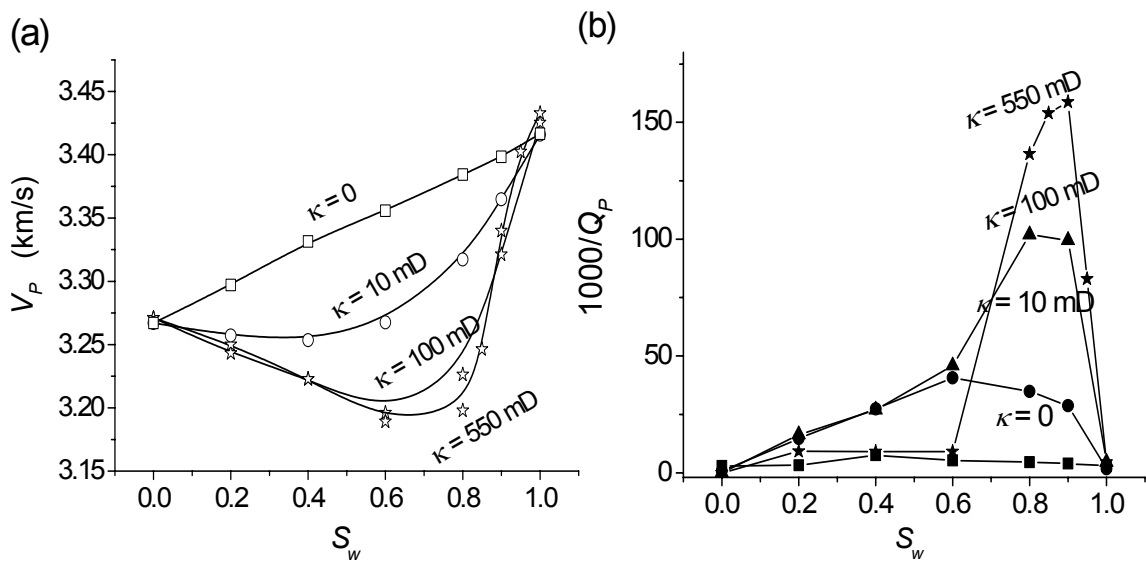


Figure 6.12: V_P (a) and Q_P^{-1} (b) versus S_w with different values of permeability determined from the numerical simulation at 100 khz

6.4.2 Heterogeneities in rock material versus fluid distribution

Heterogeneity of the rock material has also been an important factor in explaining the observed behaviour of elastic waves in rocks. Blair (1990) compared experimental attenuation measured in two frequency ranges (1-150 kHz and 1-50 kHz) on a dry granite block and concluded that grain clusters of the size (~ 10 mm) comparable to the wavelength rather than grains (~ 1 mm) themselves were responsible for the large ultrasonic attenuation. Supported by X-ray scans of the rock samples Lucet and Zinszner (1992) show similar results from sonic and ultrasonic laboratory data in saturated limestone, containing significant material heterogeneities. On the other hand, sandstone samples with more smoothly varying rock properties exhibit in general less ultrasonic attenuation. The proposed mechanism for the latter was the increased scattering (diffraction) of the waves when the wavelength is comparable with the size of heterogeneities. In the experiment shown in Figures 6.13 and 6.14 we investigate this phenomenon by substituting the gas with inclusions of low-velocity grain material (grain bulk moduli, $K_i = \mu_i = 24.4$ GPa embedded in a background of 35 GPa) such that P-wave impedance contrasts are approximately the same as in case of gas inclusions. Here we keep the porosity unchanged. The fractal distributions are identical with those of the corresponding gas-fluid models (Figure 6.2) and the rock is fully saturated with water.

We display the results for 100 kHz and 500 kHz and compare them with the corresponding models containing gas inclusions. Firstly, in the case of material inclusions there is minor velocity dispersion and negligible response to the patch size, compared to those of gas inclusions (Figure 6.13). Note that $S_i = 1$ presents for low-velocity (soft) grain material (or for gas saturated rock). For attenuation (Figure 6.14), on the other hand, we find a significant response both to frequency and patch size. In the patchy model, the relaxation peaks for material and gas inclusions coincide at 500kHz. For the magnitude of attenuation, the effects of patch size is opposite: While small gas patches (uniform model) favour high attenuation, the larger patch size (patchy model) seems more favourable in case of material inclusions, in particular at 500 kHz when the wavelength of the primary wave ($\lambda \sim 5$ mm) coincides with the dominant patch size (Figure 6.2b).

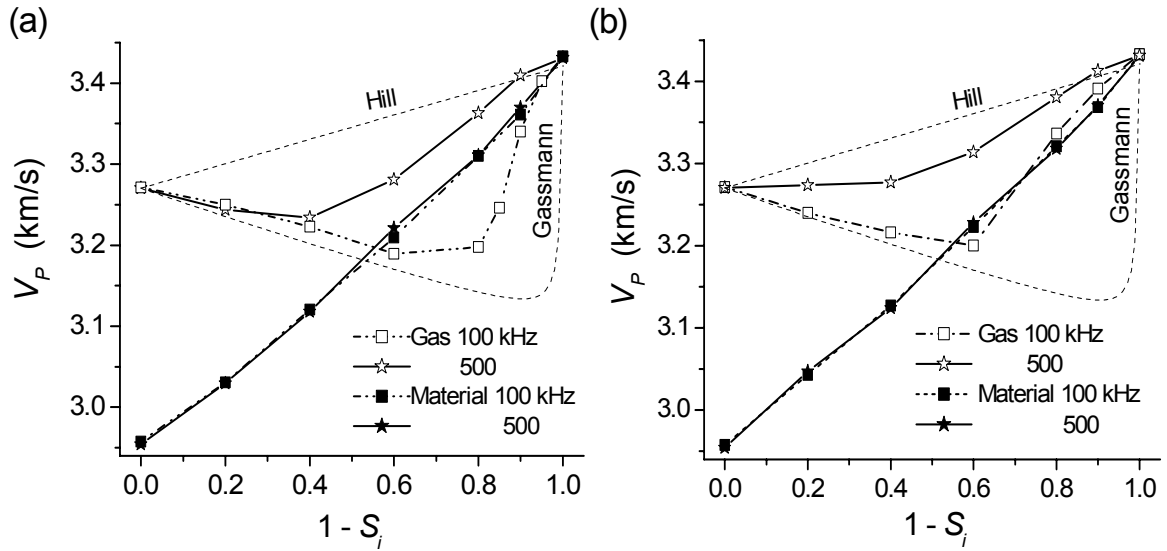


Figure 6.13: P-wave velocity versus gas or material inclusion S_i determined from the numerical simulation in uniform (a) and patchy models (b).

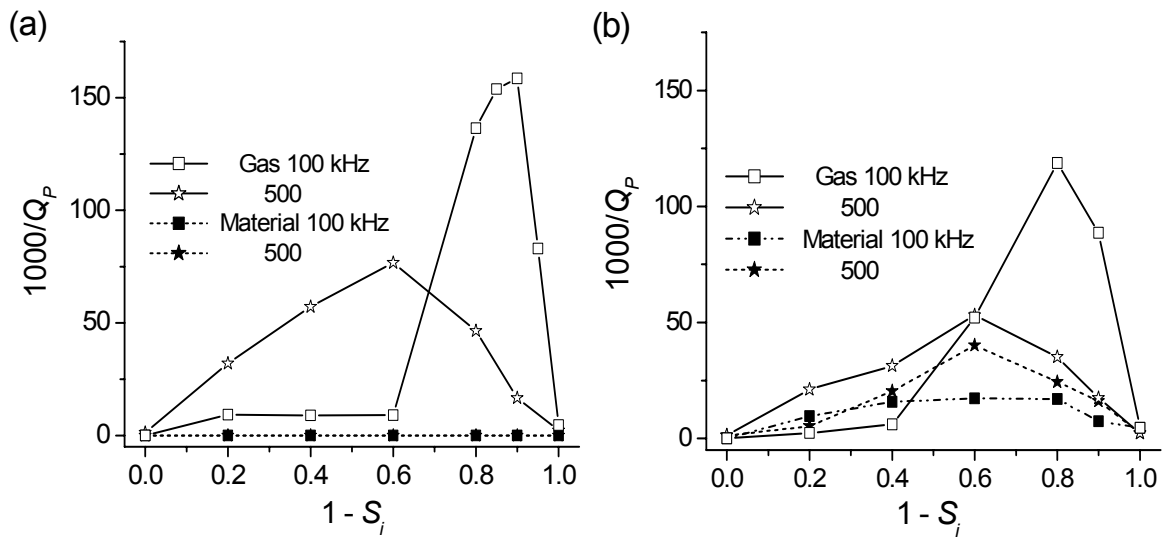


Figure 6.14: P-wave attenuation versus gas or material inclusion S_i determined from the numerical simulation in uniform (a) and patchy models (b).

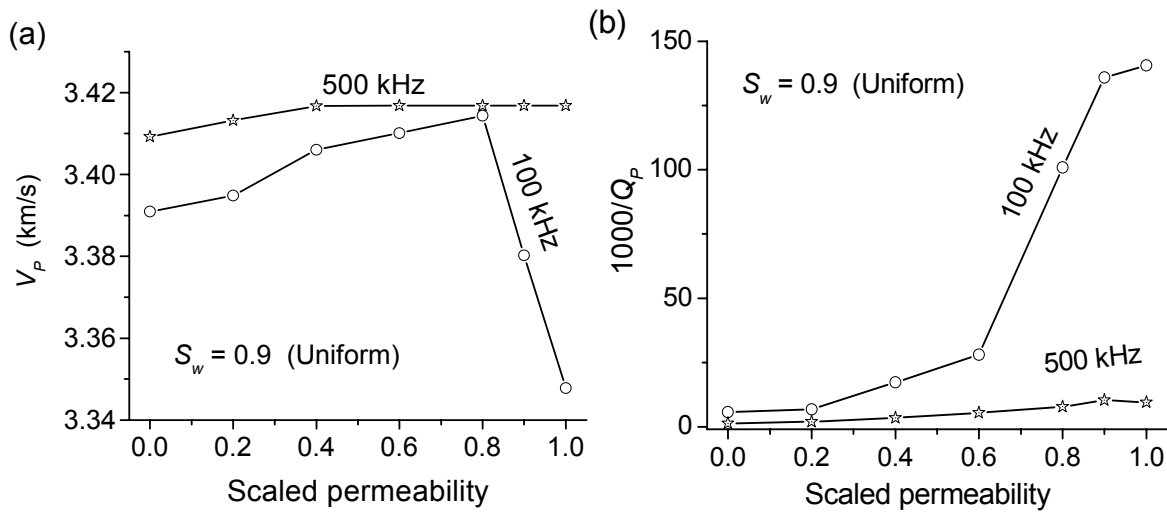


Figure 6.15: P-wave velocity V_P (a) and attenuation Q_P^{-1} (b) versus scaled permeability (2-2000 mD).

Heterogeneity in permeability is a related problem. We have shown (Figure 6.12) that in a fully saturated rock (gas or water) the permeability has minor effects on the wavefield. On the other hand, by introducing a small fraction of gas in water-saturated rocks, the permeability becomes a key parameter. Motivated by the observation of patchy distribution of permeability apparent from cores and well logs (Helle et al., 2001), we introduce the following model: The background model is the porous rock (Table 6.1) with an effective water saturation $S_w = 0.9$ where the water/gas mixture is distributed according to the uniform model. Super-imposed on the uniform fluid heterogeneities we introduce the patchy model for permeability, using the binary values of 2 mD and 2000 mD, respectively, to cover the range of effective permeability in a real reservoir. This experiment mimics a realistic situation where the rock contains a small fraction of gas (10 %) uniformly distributed throughout the matrix at a fine scale, but where patches of calcite cemented grains control the effective permeability at a coarser scale. Starting with a model of homogeneous permeability of 2 mD, we gradually add permeability patches of 2000 mD until the rock attains a homogeneous permeability of 2000 mD. The resulting velocity-attenuation pairs obtained from the poro-elastic simulation are shown in Figure 6.15. For 100 kHz, there is a strong response in velocity and attenuation due to the permeability patches, as may be expected from the results shown in Figure 6.12 where the response to permeability is at its maximum around $S_w = 0.9$. The response is comparable in magnitude to the case of partial saturation. For higher frequencies (500 kHz), the response is weak with a slow monotonic increase in velocity and attenuation with increasing effective permeability.

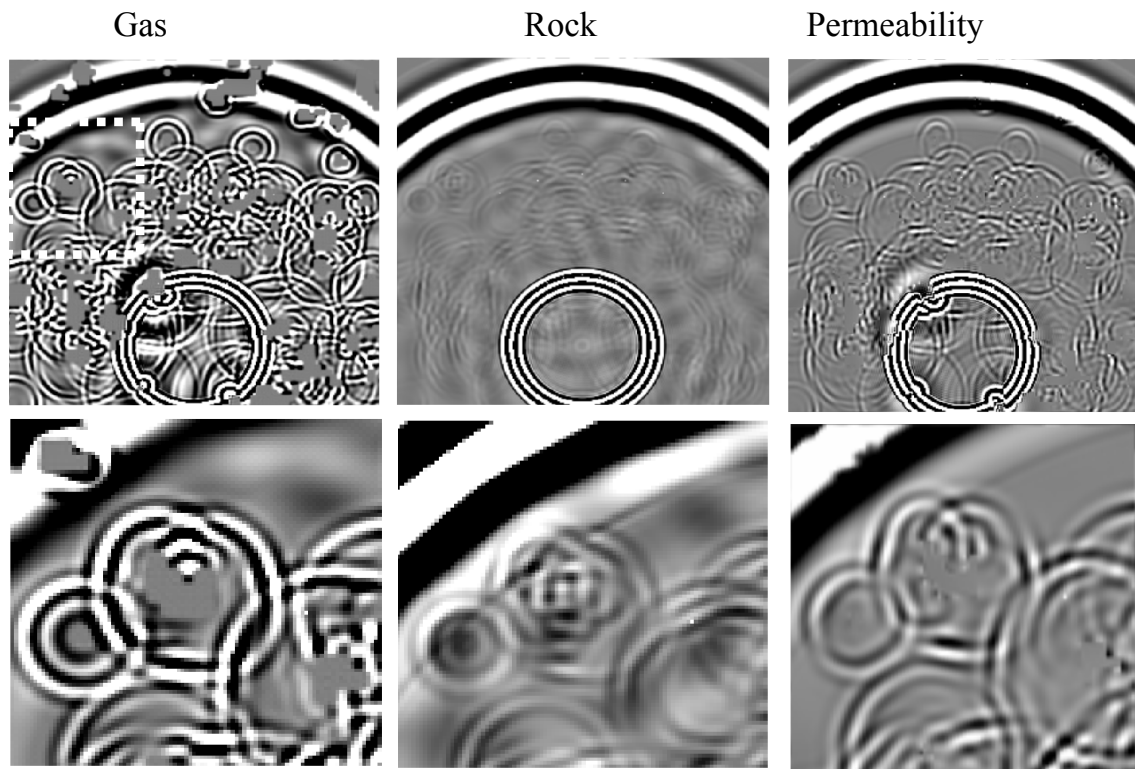


Figure 6.16: Snapshots (68.5×68.5 mm) after 300 time-steps ($18.6 \mu\text{s}$) of the fluid pressure p for patchy fluid/gas model for $S_g = 0.1$ (left), the equivalent concentration and same distribution of solid inclusions (middle) and permeability inclusions (right) in a fully water saturated rock. $f = 500$ kHz. Bottom pictures show details of slow wave conversion at the inclusion patches.

The snapshots of the fluid pressure for the three alternative inclusions (Figure 6.16) reveal that slow-waves are generated at the heterogeneities in all cases, but to varying degrees. Slow-wave generation thus seems to be an important factor for any type of heterogeneity in a fluid-filled porous rock, and is particularly effective in the presence of gas. Gas inclusions are the most effective slow-wave exciters whereas material inclusions in the case of full water saturation are less efficient. Effects of permeability patches are of great practical significance and therefore, deserve a more detailed evaluation and discussion. However, from the simple experiments above, we conclude that patches in the permeability give a strong response in the lower end of the ultrasonic band, and probably also at sonic frequencies.

6.5 Conclusions

Seismic wave propagation in porous rocks depends not only on the degree of saturation but also in the distribution of the fluid phase at various scales. In the present study, we have applied a numerical solution of Biot's poro-elastic differential equation to simulate the wavefield in a porous rock partially saturated with water and gas. Two fractal distributions of the fluid are designed to match published laboratory experiments; uniform distribution of small-scale patches corresponding to variation of saturation by depressurisation, and the large-scale patches characteristic for drainage by drying. We record and analyse the transmitted wave with respect to P-wave velocity and attenuation in the frequency range 10-500 kHz as a function of effective partial saturation.

Peaks in attenuation versus saturation are linked with a crossover frequency, from relaxed to unrelaxed modes, determined by the hydraulic properties of the host rock, the properties of viscous fluids and the fluid distribution within the rock matrix. The observed critical saturation from the poro-elastic simulation is in qualitative agreement with White's theory (more details in chapter 7) and equivalent to the published observations of attenuation peaks as function of viscosity, permeability and porosity (e.g., Klimentos and McCann, 1990; Murphy et al., 1986; Ogushwitz, 1985; Carcione et al., 2002b).

The fluid distribution plays a central role in both P-wave velocity and attenuation in partially fluid/gas saturated rocks. In general, V_p and Q_p factor in case of uniform distribution are lower than in case of patchy distribution, which is in agreement with published experimental data (e.g. Cadoret, 1995).

We have shown that the conversion of fast P-wave energy, into dissipating slow P-waves at heterogeneities in the fluid and rock properties, is the main mechanism for the observed P-wave attenuation. Inclusions of gas are far more efficient slow wave excitors than inclusions of rock material, and hence, more attenuation is observed for gas inclusions than for the equivalent inclusions of rock material.

Since a patchy distribution of permeability represents an important practical problem, we have included a limited study in the present work. With a small portion of gas in the pore fill, the wave response becomes very sensitive to permeability and to the permeability distribution. The most interesting result is that both P-wave velocity and its attenuation are sensitive to permeability in partially fluid/gas saturated rocks, while they are not sensitive in the case of full saturation. This may increase the opportunities for reservoir monitoring and detection of hydrocarbons in gas/condensate reservoirs from seismic, since the permeability is directly related to the mobility of hydrocarbon in reservoir.

Chapter 7

Comparison of White's model with numerical experiments in partially saturated rocks

7.1 Introduction

In the previous chapter, I have presented numerical experiments to study the effect of partial saturation on P-wave velocity and attenuation in typical reservoir rocks. In this chapter, we compare these poro-elastic numerical experiments with White's model (White, 1975) in order to better understand and evaluate the behaviour of acoustic properties (P-wave velocities and attenuation) in partially saturated rocks.

White's model describes wave velocity and attenuation as a function of frequency, permeability and porosity, among other parameters. Attenuation and velocity dispersion is caused by fluid flow between the water phase and the gas pockets, which have different pore pressures. The critical fluid-diffusion relaxation scale is proportional to the square root of the ratio of permeability to frequency (e.g., Mavko et al., 1998, p. 207).

White's model considers spherical gas pockets located at the centre of a cubic array saturated with liquid. For simplicity in the calculations, White considers two concentric spheres, where the volume of the outer sphere is the same as the volume of the elementary cube. The theory provides an average of the bulk modulus for a single gas pocket, without taking into account the interactions between gas pockets (main effect) and (Biot) global flow (i.e., no velocity dispersion in fully saturated rock). Dutta and Odé (1979) rederived White's model using Biot's theory. Dutta and Seriff (1979) point out some corrections in White's equation, regarding the use of the P-wave modulus, instead of the bulk modulus (see also Mavko et al., 1998, p.208). Gist (1994) has successfully used White's model to fit ultrasonic velocities obtained from saturations established

using drainage techniques. He uses saturation-dependent moduli as input to White's model instead of the dry-rock moduli. The predicted velocities, considering local fluid flow, are higher than the velocities predicted by White's model. Recently, Johnson (2001) developed a generalisation of White's model for patches of arbitrary shape. This model has two geometrical parameters, besides the usual parameters of Biot's theory: the specific surface area and the size of the patches.

The numerical simulation method is the same as in chapter 6. Use of numerical simulations, based on the full-wave solution of the poro-elastic equations, can be useful to study the physics of wave propagation in partially saturated rocks. Although White's model is an idealised representation of patchy saturation, its predictions are qualitatively correct, and serve as a reference theoretical framework. In this sense, it is useful to compare the results of White's model to numerical simulations based on Biot's theory of poro-elasticity. We should, however, consider that the theory and the modelling code have the same theoretical basis (Biot's theory) [although White's model does not take into account the interaction between gas pockets and (Biot) global flow]. This investigation can be the basis for more realistic analyses, where an arbitrary (general) pore-scale fluid-distribution is considered. By using computerised tomography (CT) scans it is possible to visualize the fluid distribution in real rocks (Cadoret et al., 1995). Fractal models, such as the von Kármán autocovariance function, calibrated by the CT scans, can be used to model realistic fluid distributions (chapter 6).

P-wave and S-wave velocities can be higher in partially saturated rocks than in dry rocks, but in some cases, they are lower. As predicted by White's model, this behaviour depends on frequency, viscosity and permeability. It is therefore important to investigate the sensitivity of wave velocity and attenuation to pore-fluid distribution. This is the basis for direct hydrocarbon detection and enhanced oil recovery and monitoring, since techniques such as 'bright spot' and AVO analyses make use of those physical properties. The modelling methodology used in the present study constitutes a powerful computational tool to investigate the physics of wave propagation in porous rocks, and, in some cases, can be used as an alternative method to laboratory experiments.

7.2 White's model for partial saturation

White (1975) has assumed spherical gas pockets much larger than the grains but much smaller than the wavelength. He developed the theory for a gas-filled sphere of porous medium of radius a_1 located inside a water-filled cube of porous medium. For simplicity in the calculations, White considers an outer sphere of radius a_2 ($a_2 > a_1$), instead of a cube. Thus, the system consists of two concentric

spheres, where the volume of the outer sphere is the same as the volume of the original cube. In 3-D space, the outer radius is $a_2 = x/(4\pi/3)^{1/3}$, where x is the size of the cube. In 2-D space, the outer radius is $a_2 = x/\sqrt{\pi}$, where x is the size of the square. The distance between pockets is x . Let us denote the saturation of gas and water (brine) by $S_1(S_g)$ and $S_2(S_w)$, respectively, such that $S_1 + S_2 = 1$. Then $S_1 = a_1^3/a_2^3$ in 3-D space and $S_1 = a_1^2/a_2^2$ in 2-D space. When $a_1 = x/2$ the gas pockets touch each other. This happens when $S_1 = \pi/6 = 0.52$ in 3-D space. Therefore, for values of the gas saturation higher than these critical value or values of the water saturation between 0 and 0.48, the theory is not rigorously valid. Another limitation to consider is that the size of gas pockets should be much smaller than the wavelength, i.e., $a_1 \ll V_{Pr}/f$, where V_{Pr} is a reference velocity and f is the frequency.

The complex P-wave velocity is given by

$$V_c = \sqrt{\frac{K_c + 4\mu_m/3}{\rho}}, \quad (7.1)$$

where K_c is the complex bulk modulus (given below). μ_m is the dry-rock shear modulus and ρ is the effective density (or bulk density).

The concept of complex velocity can be used to obtain the phase velocity and attenuation (e.g. Carcione, 2001, p. 55), given by

$$V_p = \left[\text{Re} \left(\frac{1}{V_c} \right) \right]^{-1} \quad (7.2)$$

and attenuation is defined as inverse quality factor

$$Q_p^{-1} = \frac{\text{Re}(V_c^2)}{\text{Im}(V_c^2)}. \quad (7.3)$$

The dry-rock moduli K_m and μ_m can be obtained, for instance, from laboratory measurements in dry samples. If V_p and V_s are the experimental dry-rock compressional and shear velocities, the moduli are given approximately by

$$K_m = (1-\phi)\rho_s \left(V_p^2 - \frac{4}{3}V_s^2 \right), \quad \mu_m = (1-\phi)\rho_s V_s^2, \quad (7.4)$$

where ρ_s is the grain density.

The effective density is given by

$$\rho = (1 - \phi) \rho_s + \phi \rho_f, \quad (7.5)$$

where $\rho_f = S_g \rho_{f1} + (1 - S_g) \rho_{f2}$ and ρ_{f1} and ρ_{f2} are the densities of fluid 1 and fluid 2 (gas and water in White's theory).

Assuming that the dry-rock and grain moduli, and permeability, κ , of the different regions are the same, the complex bulk modulus as a function of frequency is given by

$$K_c = \frac{K_\infty}{1 - K_\infty W}, \quad (7.6)$$

where

$$\begin{aligned}
 W &= \frac{3ia_1\kappa(R_1 - R_2)}{a_2^3w(\eta_1Z_1 - \eta_2Z_2)} \left(\frac{K_{A1}}{K_1} - \frac{K_{A2}}{K_2} \right), \\
 R_1 &= \frac{(K_1 - K_m)(3K_2 + 4\mu_m)}{K_2(3K_1 + 4\mu_m) + 4\mu_m(K_1 - K_2)S_1}, \\
 R_2 &= \frac{(K_2 - K_m)(3K_1 + 4\mu_m)}{K_2(3K_1 + 4\mu_m) + 4\mu_m(K_1 - K_2)S_1} \\
 Z_1 &= \frac{1 - e^{-2\gamma_1 a_1}}{(\gamma_1 a_1 - 1) + (\gamma_1 a_1 + 1)e^{-2\gamma_1 a_1}}, \\
 Z_2 &= \frac{(\gamma_2 a_2 + 1) + (\gamma_2 a_2 - 1)e^{2\gamma_2(a_2 - a_1)}}{(\gamma_2 a_2 + 1)(\gamma_2 a_1 - 1) - (\gamma_2 a_2 - 1)(\gamma_2 a_1 + 1)e^{2\gamma_2(a_2 - a_1)}}, \\
 \gamma_j &= \sqrt{\frac{i\omega\eta_j}{\kappa K_{Ej}}}, \tag{7.7}
 \end{aligned}$$

$$\begin{aligned}
 K_{Ej} &= \left[\frac{\alpha K_{fj} \left(1 - \frac{K_j}{K_s} \right)}{\phi K_j \left(1 - \frac{K_{fj}}{K_s} \right)} \right] K_{Aj}, \\
 K_{Aj} &= \left[\frac{\phi}{K_{fj}} + \frac{1}{K_s} (\alpha - \phi) \right]^{-1}, \\
 \alpha &= 1 - \frac{K_m}{K_s},
 \end{aligned}$$

and

$$K_\infty = \frac{K_2(3K_1 + 4\mu_m) + 4\mu_m(K_1 - K_2)S_1}{(3K_1 + 4\mu_m) - 3(K_1 - K_2)S_1} \tag{7.8}$$

is the - high frequency - bulk modulus when there is no fluid flow between the patches. K_1 and K_2 are the - low frequency - Gassmann moduli, which are given by

$$K_j = \frac{K_s - K_m + \phi K_m \left(\frac{K_s}{K_{fj}} - 1 \right)}{1 - \phi - \frac{K_m}{K_s} + \phi \frac{K_s}{K_{fj}}}, \quad j=1,2, \tag{7.9}$$

where K_s and K_m are the solid- and dry-bulk moduli.

7.3 Results

We consider the material properties shown in Table 7.1, where the moduli and density of the grain material correspond to a mixture of 90 % quartz and 10 % clay. Here, we use an effective average for the grain moduli K_s and μ_s . K_{s1} , μ_{s1} and K_{s2} , μ_{s2} are the sand-grain and clay-particle bulk and shear moduli, while we assume that K_s is equal to the average of the upper and lower Hashin-Shtrikman bounds (Mavko et al., 1998, p. 106). The same approach is used for the shear modulus.

The Hashin-Shtrikman bounds for the bulk modulus are

$$K^{HS\pm} = K_{s1} \frac{\phi_2}{(K_{s2} - K_{s1})^{-1} + \phi_1 \left(K_{s1} + \frac{4}{3} \mu_{s1} \right)^{-1}}. \quad (7.10)$$

The Hashin-Shtrikman bounds for the shear modulus are

$$\mu^{HS\pm} = \mu_{s1} \frac{\phi_2}{(\mu_{s2} - \mu_{s1})^{-1} + \frac{2\phi_1 (K_{s1} + 2\mu_{s1})}{5\mu_{s1} \left(K_{s1} + \frac{4}{3} \mu_{s1} \right)}}. \quad (7.11)$$

These equations give the upper bound when the stiffest material is termed 1, and the softer material is termed 2, then, $\phi_2 = C$ and $\phi_1 = 1 - C$. The average grain density is simply $\rho_s = (1 - C)\rho_{s1} + C\rho_{s2}$, where ρ_{s1} and ρ_{s2} are the density of quartz and clay, respectively. On another hand, the lower bound is computed by interchanging which softest material (clay) is termed 1 and stiffer material (quartz) is termed 2.

The presence of clay also affects the dry-rock bulk and shear moduli. Here we use the modified model of Krief et al. (1990) (eq. 2.5) to obtain the effective dry bulk and shear moduli, where the empirical values $A = 2$ and $a = 0.5$ were obtained by fitting data as reported by Han et al. (1986) (provided by Carcione et al., 2000). In general, the typical reservoir sandstone contains few percent clay. Therefore, in the present study we use 10 % clay. Here the HS bounds are used to obtain the effective material moduli, while the modified model of Krief et al. (1990) is used for estimating the frame moduli.

Note that White's theory does not consider tortuosity [the value of tortuosity given in Table 7.1 is typical of a sandstone (e.g., Johnson et al., 1987)]. If a_1 and a_2 are the outer and inner radii of the gas pockets, and we denote the space dimension by m , water saturation can be expressed by $S_w = 1 - (a_1/a_2)^m$. A source of discrepancy between theoretical and numerical results may arise from the fact that White's theory does not consider the interaction between gas pockets, while this interaction is present in the numerical simulations.

The transition frequency separating the relaxed and unrelaxed states, which is the location of the relaxation peak, is approximately given by

$$f_c = \frac{\kappa K_{E2}}{\pi \eta_2 (a_2 - a_1)^2}, \quad (7.12)$$

where κ is the permeability, K_{E2} is given in equation (7.7), and η_2 is the viscosity of water. Dutta and Seriff (1979) consider a_1^2 , instead of $(a_2 - a_1)^2$, in the denominator. However, the relevant relaxation distance should be the thickness of the outer shell, i.e., $a_2 - a_1$. White considers a harmonic displacement applied to the outer spherical surface, which creates two different pressures in the outer shell and the inner sphere. Therefore, the relaxation distance should be the difference between the two radii (Gist, 1994). Relaxation frequencies of essentially the same physical nature, but for the plane layered rocks, have been given by White et al. (1975), Norris (1993) and Gurevich and Lopatnikov (1995). The critical frequency from equation (7.12) presents for local flow mechanism, which increases, with increasing permeability and decreasing viscosity. On the other hand, the original Biot critical frequency (eq. 2.26) has opposite behaviours, since it presents for global flow mechanism.

There are two cases giving the same gas saturation. They are illustrated in Figure 7.1 for a two-dimensional porous medium. Figure 7.1a shows four gas pockets, where the gas saturation is $S_g = 4\pi a_1^2$ [the size of the square is $x = 1/2$, and $a_2 = 1/\sqrt{\pi}$ (see section 7.2)]. We may increase the saturation to $S_g = 16\pi a_1^2$ in two different ways. In Figure 7.1b, a_1 is constant, while in Figure 7.1c, a_2 is constant.

When a_2 is constant, we can deduce the critical water saturation, S_{wc} , for which the attenuation is maximum. For a given frequency, and using $S_w = 1 - (a_1/a_2)^3$, we obtain from equation (7.12):

$$S_{wc} = 1 - \left(1 - \sqrt{\frac{\kappa K_{E2}}{\pi \eta_2 f a_2^2}} \right)^3, \quad (7.13)$$

If a_1 is constant, the critical saturation is given by

$$S_{wc} = 1 - \left(1 + \sqrt{\frac{\kappa K_{E2}}{\pi \eta_2 f a_1^2}} \right)^{-3}, \quad (7.14)$$

Grain	bulk modulus,	K_{s1}	39 Gpa
	shear modulus,	μ_{s1}	33 Gpa
	density,	ρ_{s1}	2650 kg/m ³
Clay	bulk modulus,	K_{s2}	20 Gpa
	shear modulus,	μ_{s2}	15 Gpa
	density,	ρ_{s2}	2000 kg/m ³
Matrix	bulk modulus,	K_m	8.67 GPa
	shear modulus,	μ_m	6.61 GPa
	porosity,	ϕ	0.3
	permeability,	κ	0.55 D
	tortuosity,	T	2.5
Water	bulk modulus,	K_w	2.4 GPa
	density,	ρ_w	1040 kg/m ³
	viscosity,	η_w	1.8 cP
Gas	bulk modulus,	K_g	0.01 GPa
	density,	ρ_g	100 Kg/m ³
	viscosity,	η_g	0.02 cP
$C = 10 \%$, $K_s = 34.32$, $\mu_s = 35.32$ GPa, $\rho_s = 2585$ kg/m ³			

Table 7.1: Material properties of the rock.

As stated in section 7.2, the size of the gas pockets, a_1 , should be much smaller than the wavelength. Let us consider a reference velocity $V_{Pr} = 3000$ m/s, a maximum outer radius $a_2 = 7$ mm, and $S_g = 0.52$ [the upper-limit gas saturation for which White's model holds (see section 7.2)]. Since $a_1 = a_2 S_g^{1/3}$, the condition $a_1 \ll V_{Pr}/f$ implies $f \ll 536$ kHz. With these limitations in mind, we proceed in the following to analyse White's results and compare these results with numerical simulations.

The modelling algorithm uses a numerical mesh with rectangular cells (here we consider square cells). Let us assume that a_2 is constant. Since the size of the elementary square $x = \sqrt{\pi} a_2 = n \Delta x$, where n is a natural number and Δx is the grid

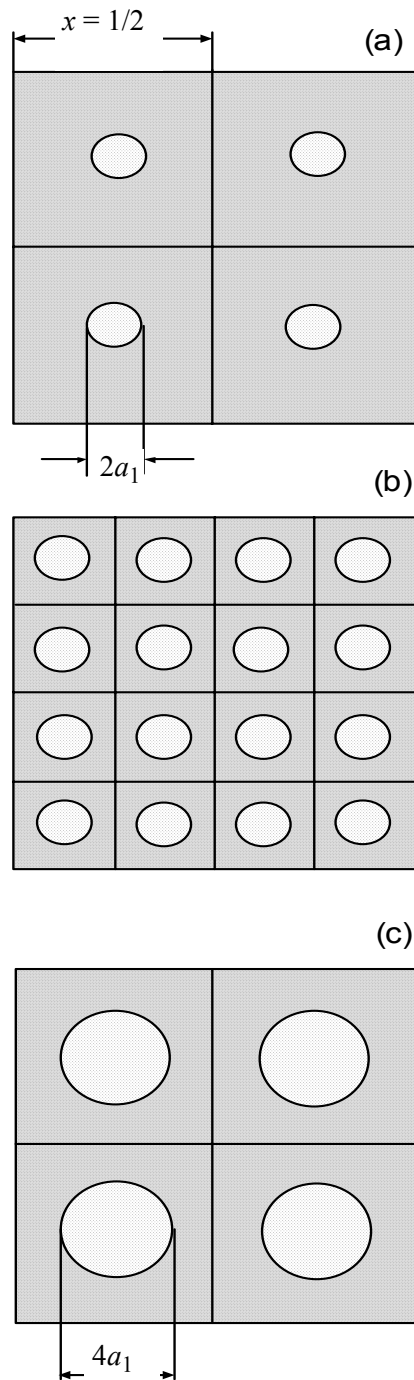


Figure 7.1: Two different sizes for the gas pockets give the same gas saturation, depending on the values of the inner and outer radii a_1 and a_2 . In (a) the saturation is $S_g = 4\pi a_1^2$, while in (b) and (c) the saturation is the same and equal to four times the saturation in (a). Gas saturation can then change by varying a_1 and keeping constant a_2 or vice versa.

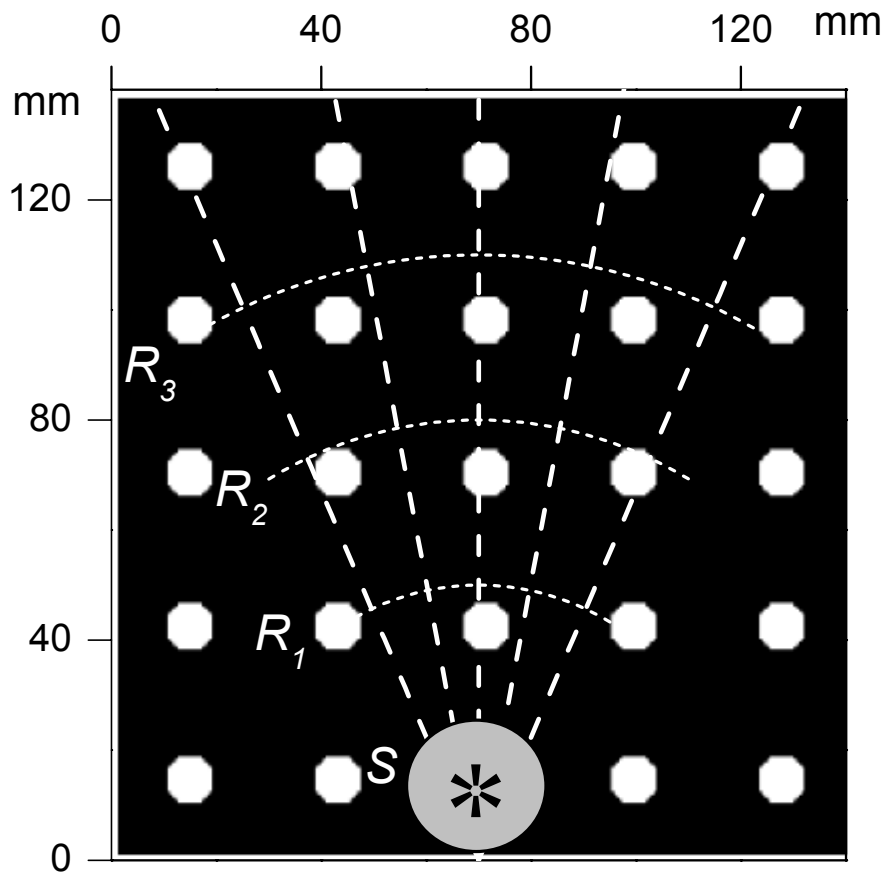


Figure 7.2: White's model in a two-dimensional numerical mesh. Water and gas are indicated by black and white colors, respectively. Source (S) and receivers (R_i) are indicated. A circular region surrounding the source is fully water saturated to assure a uniform initial wavefront. Gas pocket radius is $a_1 = 2$ mm and water saturation $S_w = 0.918$ ($a_2 = 7$ mm).

spacing, $\Delta x = \sqrt{\pi} a_2 / n$. If N is the number of cells of the gas pocket, then $N \Delta x^2 = \pi a_1^2$, and $S_g = N/n^2$. On the other hand, if a_1 is constant, the grid size is computed as $\Delta x = a_1 \sqrt{\pi / N}$. An example of White's partial saturation model represented on a 2-D numerical grid is shown in Figure 7.2, where water and gas are indicated by black and white colours, respectively. The model is an example for $a_1 = 2$ mm and a source central frequency of 100 kHz. The grid size is 208×208 and the grid spacing is $\Delta x = 0.886$ mm (30 grid points are used for the absorbing boundaries at the sides of the mesh). A gas pocket is modelled with $N = 16$ cells, $n = 14$, $x = 12.41$ mm and $a_2 = 7$ mm. Water saturation is then $S_w = 0.918$. The simulation corresponding to the model shown in Figure 7.2 uses a time step of $0.12 \mu\text{s}$. The source in all the simulations is a Ricker wavelet applied to the solid

skeleton and the fluid phase (a bulk source without shear components). A region with a radius of 30 grid points and 100 % water saturation surrounds the source location in order to obtain a uniform initial wavefront.

Let us first consider that the radius of the outer sphere, a_2 , is constant and equal to 4 mm. Figure 7.3 shows the P-wave velocity (a) and attenuation factor (b) versus water saturation for different frequencies and a permeability of 550 mD. The analytical and numerical (black dots) evaluation of Gassmann's velocity has been performed on a homogeneous porous medium by averaging the fluid bulk modulus with Wood's equation (Mavko et al., 1998, p. 112). Gassmann's velocity (e.g., Carcione, 2001b, p. 257) is also shown as a dotted curve. The differences in velocity can be important for increasing frequency. For instance, the difference between the seismic velocity (Gassmann's curve) and the ultrasonic velocity (100 kHz) predicted by White's model is 120 m/s at 90 % water saturation [the respective wavelengths are approximately 150 m (seismic frequencies) and 3 cm (100 kHz)]. The simulations predict higher velocities compared to White's model, and the relaxation peaks are shifted towards lower water saturations. At full saturation, the numerical results reveal slightly higher velocities than predicted by White's theory, since White's theory does not consider (Biot) global flow, i.e., K becomes real in fully saturated rocks (eqs. 7.6, 7.7), and therefore, no energy losses occur. However, the physics revealed by the numerical results is similar to that predicted by White's model.

Figure 7.4 shows the P-wave velocity (a) and attenuation factor (b) versus water saturation for different permeabilities and a frequency of 100 kHz. The dotted line is Gassmann's velocity, obtained by mixing the fluid moduli with Wood's average. The numerical phase velocities coincide with White's velocities for low permeabilities. For 550 and 5000 mD, the simulations predict higher velocities. This implies greater velocity dispersion (see also the higher attenuation levels in Figure 7.4b), due to additional dissipation mechanisms, which are not predicted by White's model.

Figure 7.5 shows the P-wave velocity (a) and attenuation factor (b) versus frequency for different water saturations. The permeability is 550 mD. As before, higher velocities and attenuation levels, compared to White's model, are observed by the numerical simulations. The shift of the peaks towards lower frequencies can be an indication of the presence of local fluid flow mechanisms.

Let us assume now that the radius of the gas pockets, a_1 , is constant and equal to 2 mm. The results, corresponding to Figures 7.3, 7.4 and 7.5, are respectively shown in Figures 7.6, 7.7 and 7.8. The results reveal the same physical behaviour as for constant a_2 .

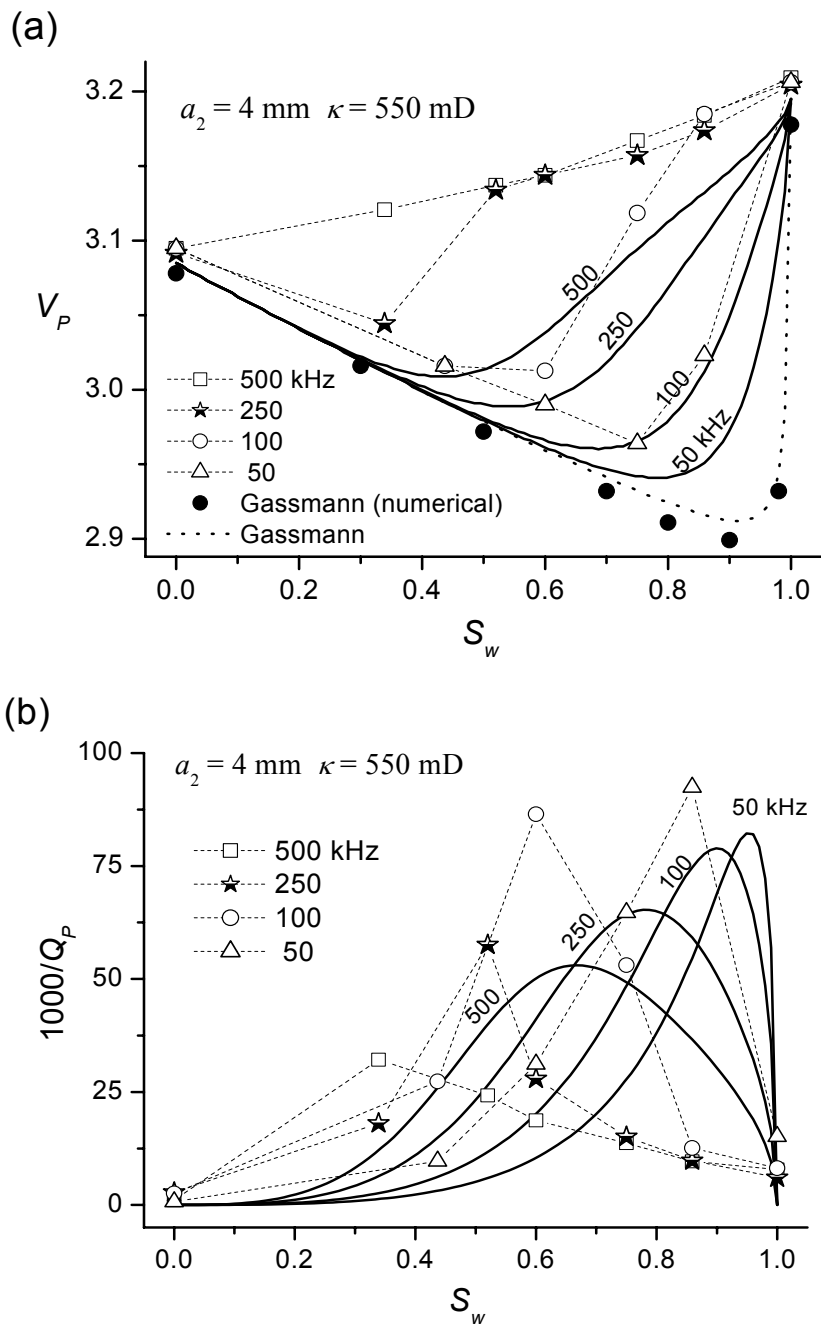


Figure 7.3: P-wave velocity (a) and attenuation factor (b) versus water saturation for different frequencies. The dashed line is the results from simulations, while the solid lines are from White's model. The dotted line in (a) is Gassmann's velocity, obtained by mixing the fluid moduli with Wood's average.

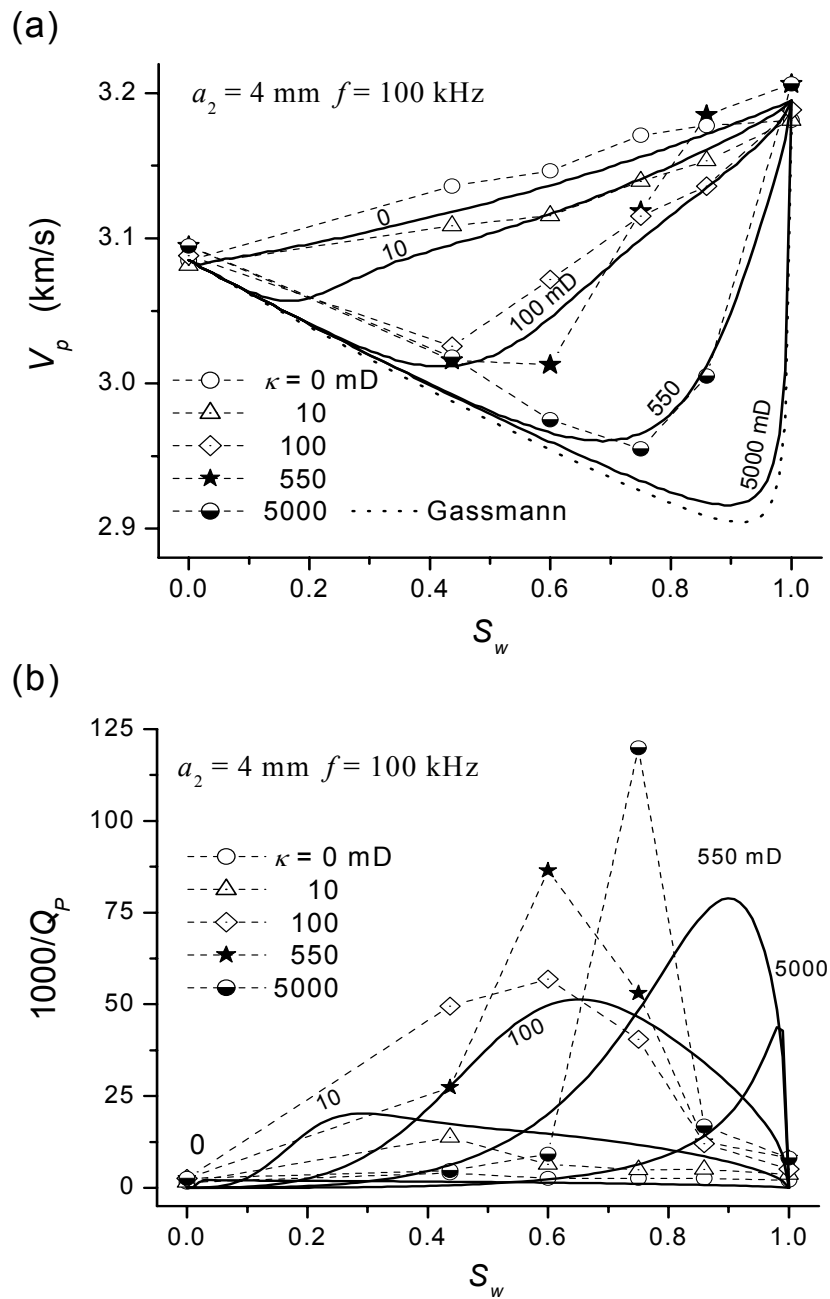


Figure 7.4: P-wave velocity (a) and attenuation factor (b) versus water saturation for different permeabilities and a frequency of 100 kHz. The dashed line is the results from simulations, while the solid lines are from White's model.

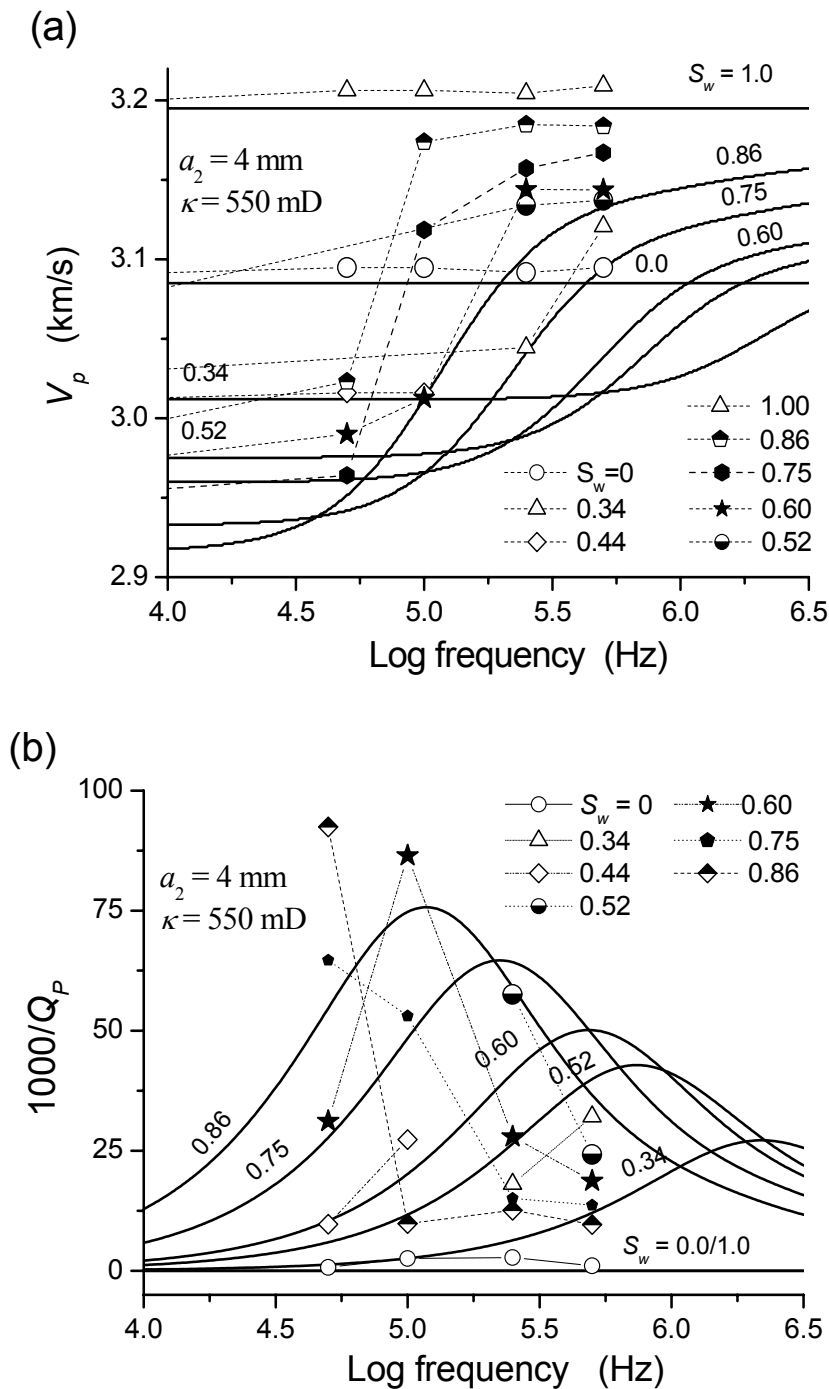


Figure 7.5: P-wave velocity (a) and attenuation factor (b) versus frequency for different water saturations. The location of critical frequencies is indicated for different saturations. The dashed lines are the results from simulations, while the solid lines are from White's model.

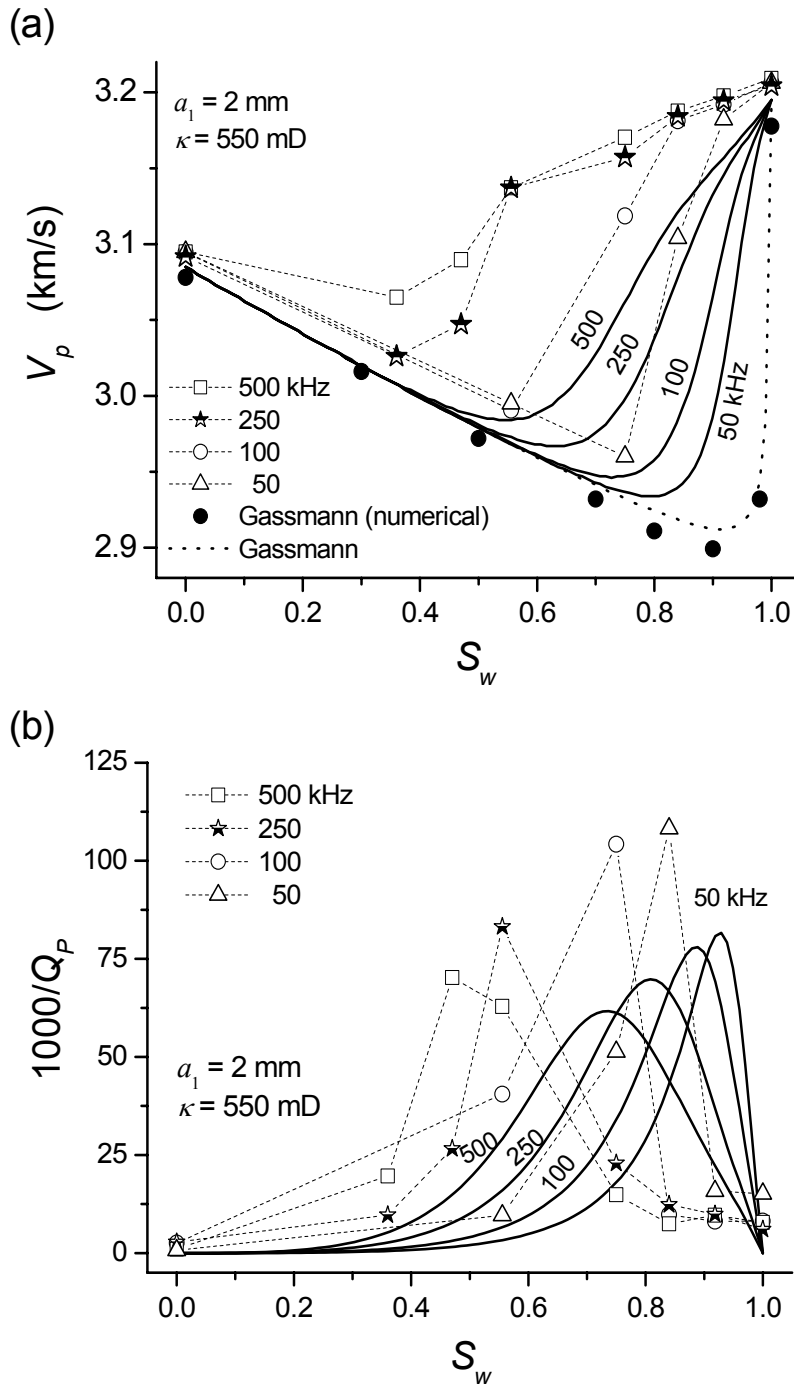


Figure 7.6: As in Figure 7.3, but in this case, we keep constant the radius of the gas pockets $a_1 = 2 \text{ mm}$.

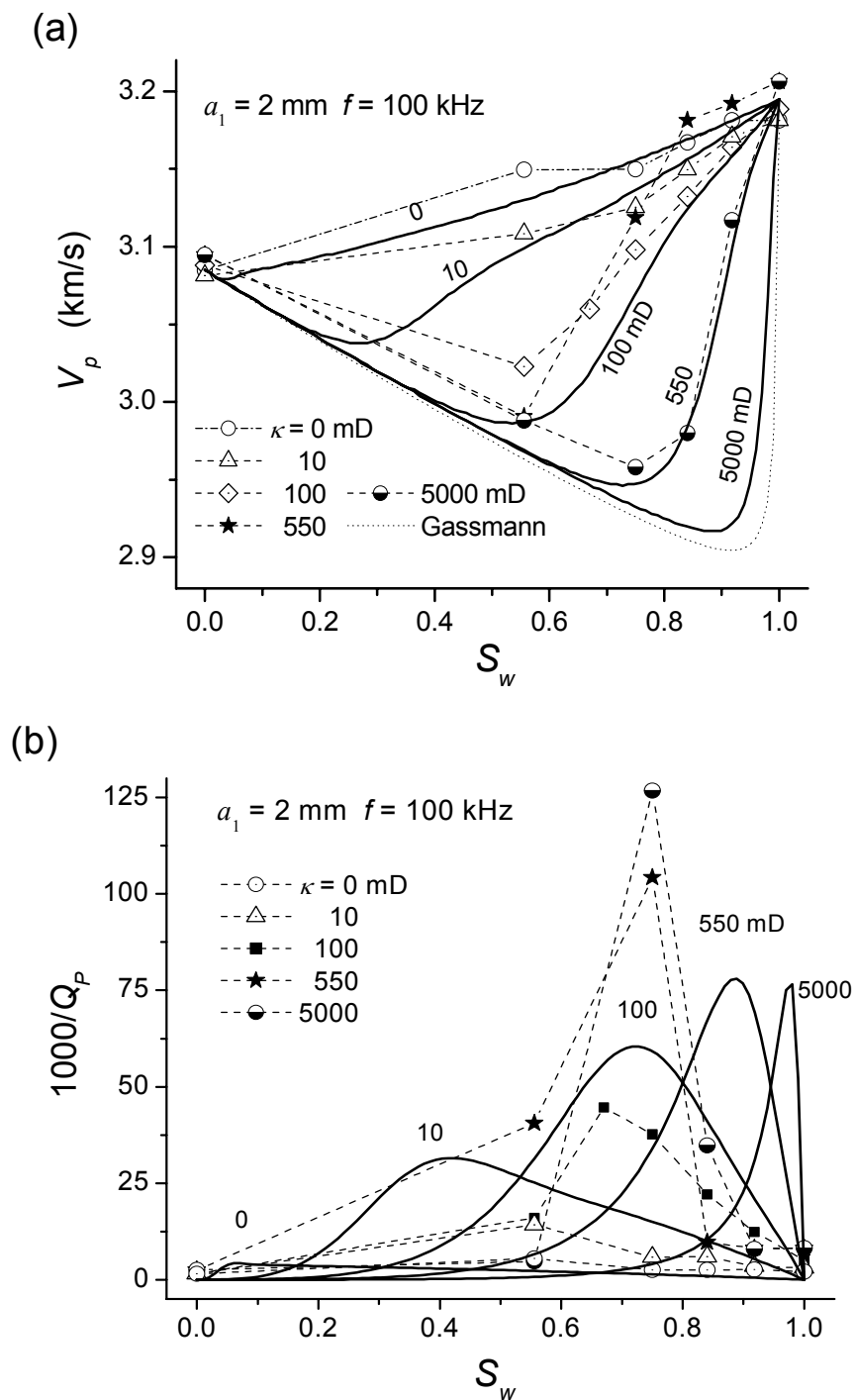


Figure 7.7: As in Figure 7.4, but in this case, we keep constant the radius of the gas pockets $a_1 = 2 \text{ mm}$.

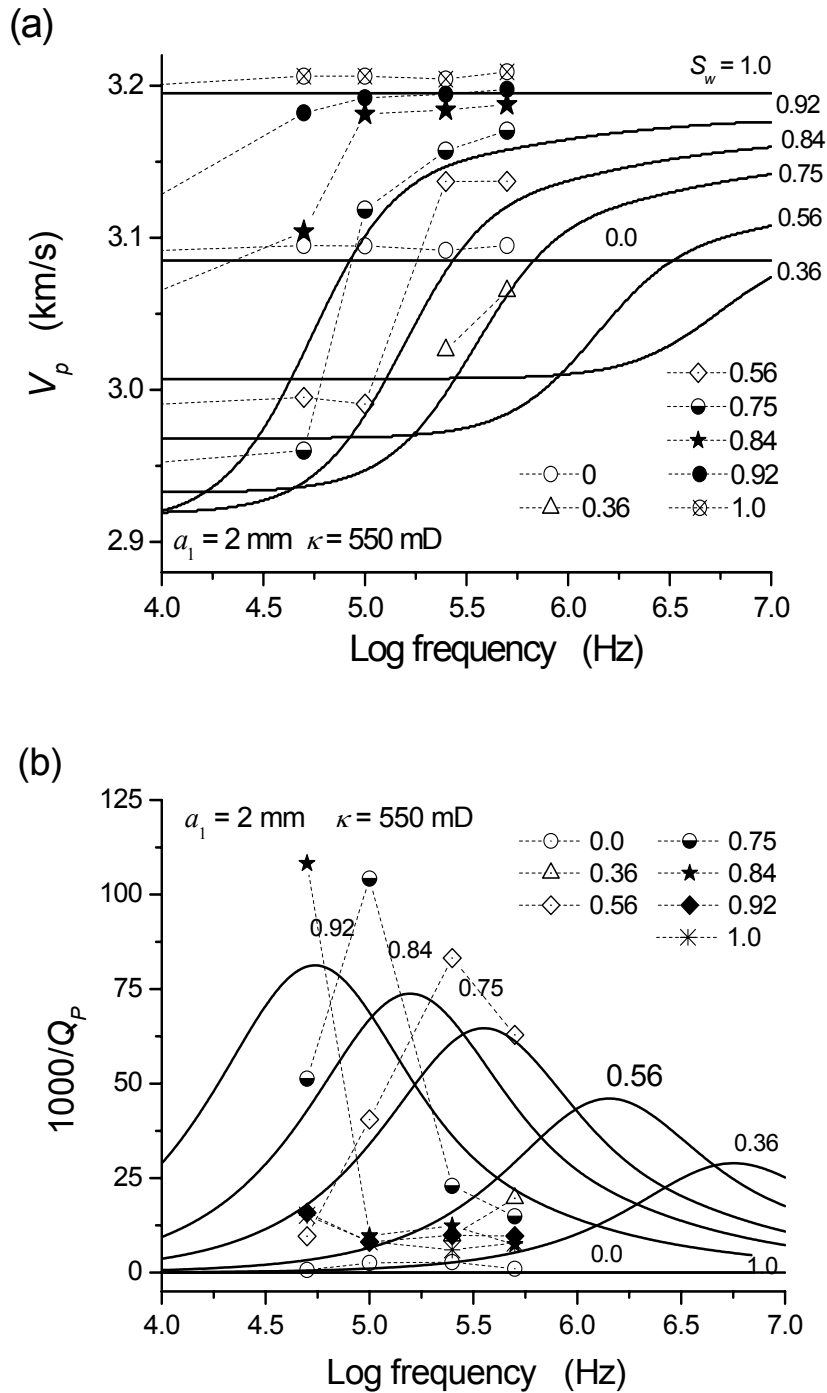


Figure 7.8: As in Figure 7.5 but, in this case, we keep constant the radius of the gas pockets $a_1 = 2$ mm.

The critical water saturation, shown in Table 7.2 is in fairly good agreement with the location of the relaxation peaks predicted by White's model. We observe the same physical behaviour for both constant a_2 and constant a_1 , indicating that the physics is substantially dependent on the difference $a_2 - a_1$ (see eq. 7.12).

Since equation (7.12) has the form of a length-squared dependency characteristic of diffusion phenomena, we define a critical length scale

$$L_c \approx \sqrt{\frac{\kappa K_{E2}}{\pi \eta_w f}} = (a_2 - a_1), \quad (7.15)$$

suggesting that during a seismic period the pore-pressure can equilibrate over a spatial scale smaller than L_c , corresponding to the distance over which the slow wave propagate/diffuses away from a gas-fluid interface (e.g. Johnson, 2001). In contrast, saturations that are heterogeneous over scales larger than L_c have wave induced pore pressure gradients that cannot equilibrate. Critical length scales are typically 1-10 mm for laboratory measurements and tens of centimetres for field seismic frequencies (Mavco and Mukerji, 1998). Critical saturation (solid line) and relaxation scale (dashed line) versus frequency, obtained from equations (7.14, 7.15), respectively, are shown in Figure 7.9. Note that the critical saturation theory from equations (7.14, 7.15) does not exist at full saturation. Using the material properties from table 7.1 the relaxation peaks appear close to $S_w = 1$ at laboratory saturation scales ($a_1 \sim 0.5$ -5 mm), and move to lower S_w with increasing a_1 , approaching to seismic saturation scale. In particular, the relaxation peak is independent of frequency for $a_1 = 0.1$ mm. However, we have to keep in mind that the size of the gas pockets, a_1 , should be much smaller than the wavelength following White's model. The relaxation scale L_c is dependent only on the rock and fluid properties, and decreases rapidly from several centimetres within the seismic frequency band to about 0.5 mm in the ultrasonic range.

Snapshots of the fluid particle velocity relative to the solid (a), fluid pressure (b), and particle velocity of the solid (c) are shown in Figure 7.10. They correspond to the model shown in Figure 7.2, with 92 % water saturation and a central frequency of 500 KHz and a corresponding smaller grid spacing $\Delta x = 0.1$ mm in a 660×660 to highlight the details (54 grid points are used for the absorbing boundaries at the sides of the mesh). The two main wavefronts are the fast P-wave and the slow P-wave. The conversion fast P-wave to slow P-wave at each gas pocket can clearly be appreciated. At 500 KHz, slow waves have a phase velocity of 841 m/s in the brine saturated region and 200 m/s in the gas pockets (the fast P-wave velocity is 3210 and 3094 m/s, respectively). The primary fast wave P^+ generates slow waves P^+P^- at the gas pockets. In addition, significant

$a_2 = 4 \text{ mm} , \kappa = 550 \text{ mD}$				
f (kHz)	50	100	250	500
White's model	0.95	0.90	0.78	0.67
S_{wc}	0.99	0.90	0.72	0.56
$a_2 = 4 \text{ mm} , f = 100 \text{ kHz}$				
κ (mD)	10	100	550	5000
White's model	0.29	0.65	0.90	0.98
S_{wc}	0.21	0.55	0.91	1.00
$a_1 = 2 \text{ mm} , \kappa = 550 \text{ mD}$				
f (kHz)	50	100	250	500
White's model	0.74	0.81	0.89	0.93
S_{wc}	0.70	0.79	0.89	0.94
$a_1 = 2 \text{ mm} , f = 100 \text{ kHz}$				
κ (mD)	10	100	550	5000
White's model	0.34	0.68	0.89	0.99
S_{wc}	0.41	0.73	0.55	0.98

Table 7.2: locations of relaxation peaks (in saturation) obtained from White's model and critical saturation expressions (7.13, 7.14).

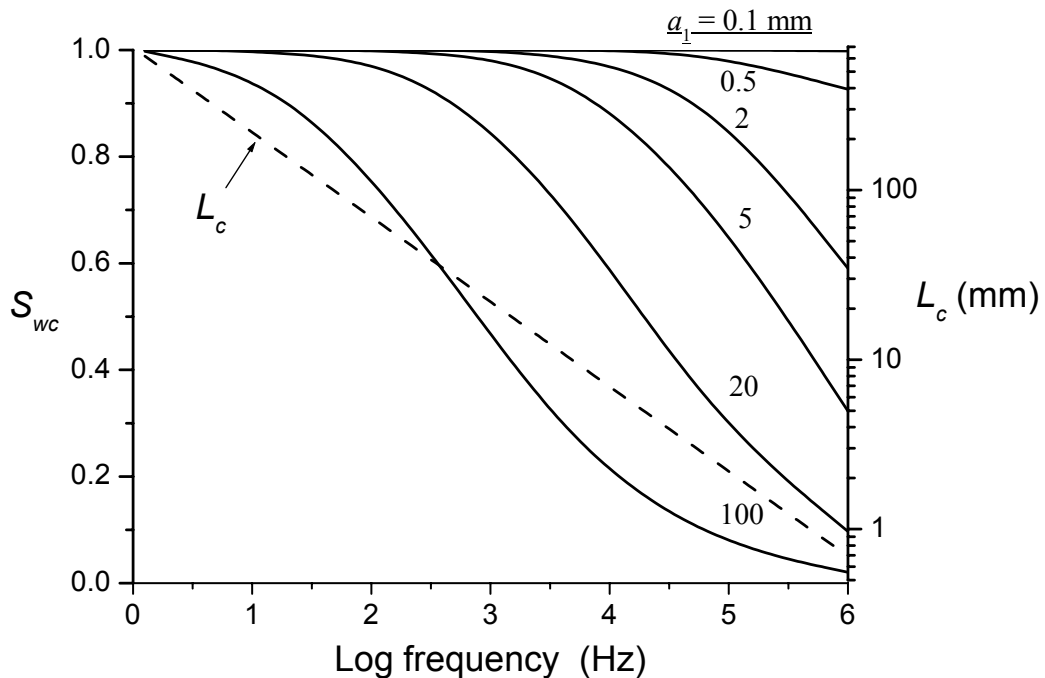


Figure 7.9: Critical water saturation S_{wc} (solid line) and relaxation scale L_c (dashed line) as a function of wave frequency f for a range of values of the radius a_1 of the gas spheres (patches). Material and fluid properties are as given in Table 7.1.

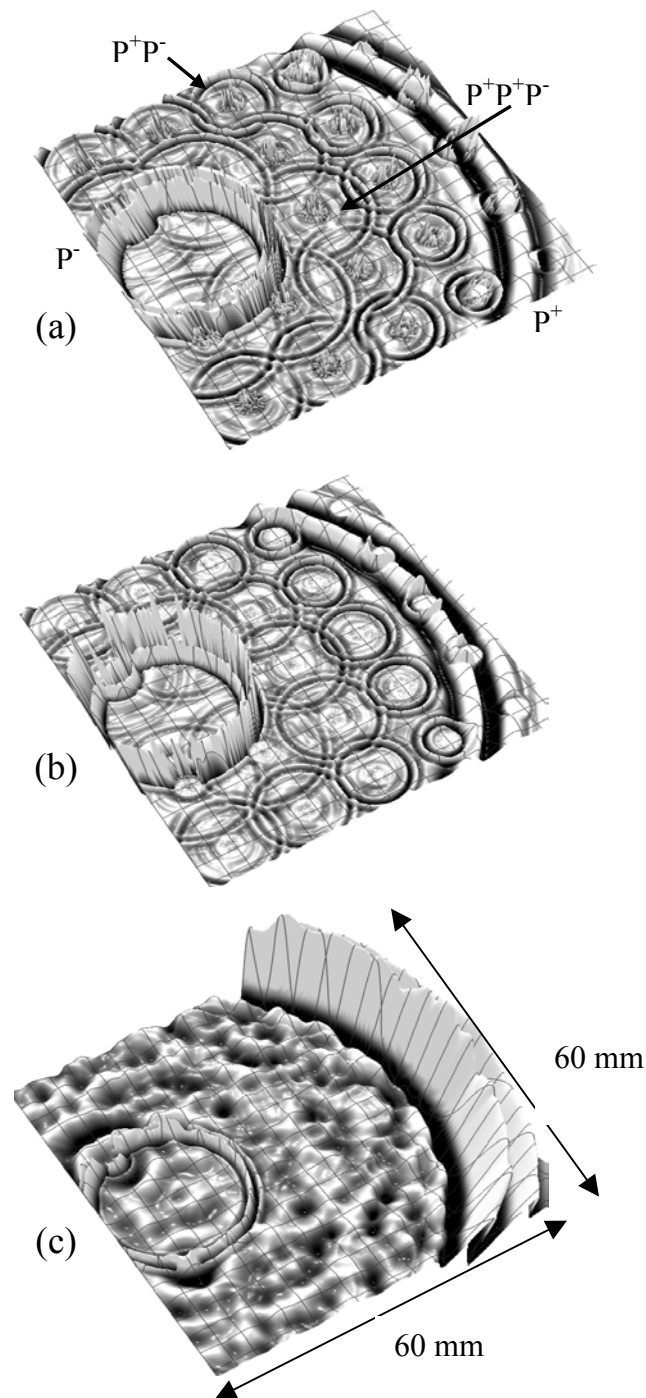


Figure 7.10: Snapshot of the fluid particle-velocity relative to the solid (a), fluid pressure field (b) and solid particle velocity (c) corresponding to the model shown in Figure 7.2, with 92% water saturation and a central frequency of 500 kHz. Propagation time is $18 \mu s$.

slow waves are generated by the scattered P^+ inside the gas pocket ($P^+P^+P^-$). These are the two main events generated in the fluid phase during passage of the primary P^+ , and thus represent the most significant loss components, removing energy from the front of the pulse and adding to its tail. The fluid particle velocity of the slow waves (Figure 7.10a) is high within the gas pocket and less pronounced in the brine, while for the fluid pressure (Figure 7.10b), the situation is the opposite. In the solid (Figure 7.10c), P^+ dominates the wavefield, while the slow waves are less clearly identified.

A final numerical experiment to illustrate the phenomenon is shown in Figure 7.11. Figure 7.11 shows a gas pocket of radius $a_1 = 5$ mm with a circular source located at a distance $a_2 = 23$ mm from its centre. The rock and pore-fill are the same as in the previous experiment (Table 7.1). We use a fine mesh of $\Delta x = 0.1$ mm and a source frequency of 500 kHz. The seismograms of the particle velocity (Figure 7.12) are recorded at receivers located 1 mm away from the fluid/gas boundary in the water saturated and gas saturated rock, respectively. P^+ denotes the direct fast wave and $P_C^+P^+$ is its return from the pocket centre (focus). $P_B^+P^-$ and $P_C^+P^-$ are their associated slow waves. In the solid, the P^+ arrival is shown together with the scattered $P_C^+P^-$ wave with opposite phase after focusing in the centre of the gas pocket. In the fluid wavefield, we observe the corresponding slow waves $P_B^+P^-$ and $P_C^+P^-$, respectively, generated at the fluid/gas boundary. These are equivalent to the two consecutive slow waves apparent from the experiment in Figure 7.10. The tail of arrivals recorded within the gas zone, following the main events, consists of slow waves due to P^+ ringing within the gas pocket, while the late P^- events at the end of the record are the direct (in the brine) and transmitted (in the gas) slow wave generated at the source.

More details of these experiments can be appreciated in Figure 7.13, which shows the seismograms of the fluid (relative) (a) and solid (b) particle velocities along the receiver line. The fast- and slow-wave events are clearly distinguishable by their different dips, i.e. low angles (high velocity) for P^+ and high angles (low velocity) for P^- . The focusing of the direct P^+ is well expressed in both fluid and solid particle velocities, and a similar focusing of P^+ is evident in the lower section of (b), originating from P^- to P^+ conversion at the water/gas interface. The latter, however, has less relevance for the problem at hand since this event is confined to the tail of the recorded pulse. On the other hand, the first event is important since it interferes with the primary pulse, and, moreover, continues to bounce around within the gas pocket (b) generating multiples of slow waves propagating inwards in the gas zone as well as outwards in the fluid zone (a). The two most significant slow-wave events ($P_B^+P^-$ and $P_C^+P^-$) are clearly separated in the seismograms.

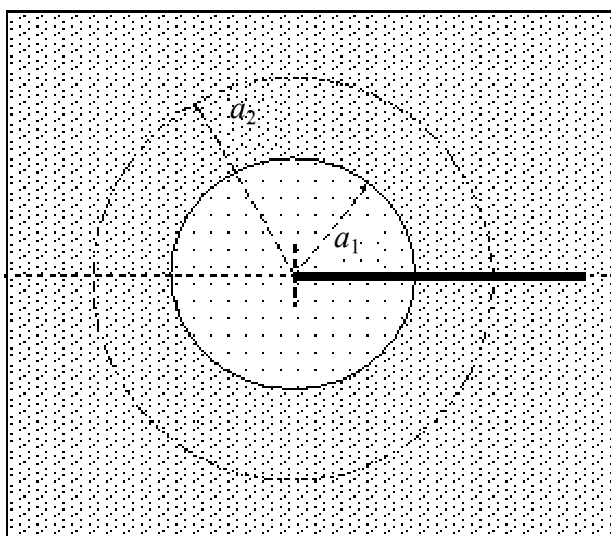


Figure 7.11: Model of a single gas pocket with radius $a_1 = 5$ mm and a circular source located at a distance $a_2 = 23$ mm.

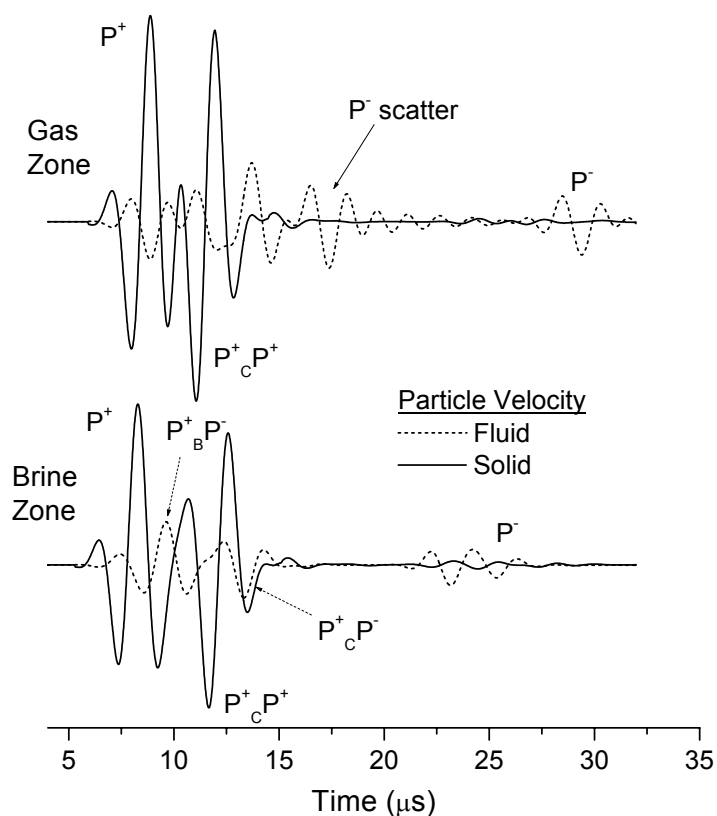


Figure 7.12: Fluid and solid particle velocities are recorded in receivers located on each side (1mm) of the gas/fluid boundary. The solid line indicates receivers for the seismograms in Figure 7.13.

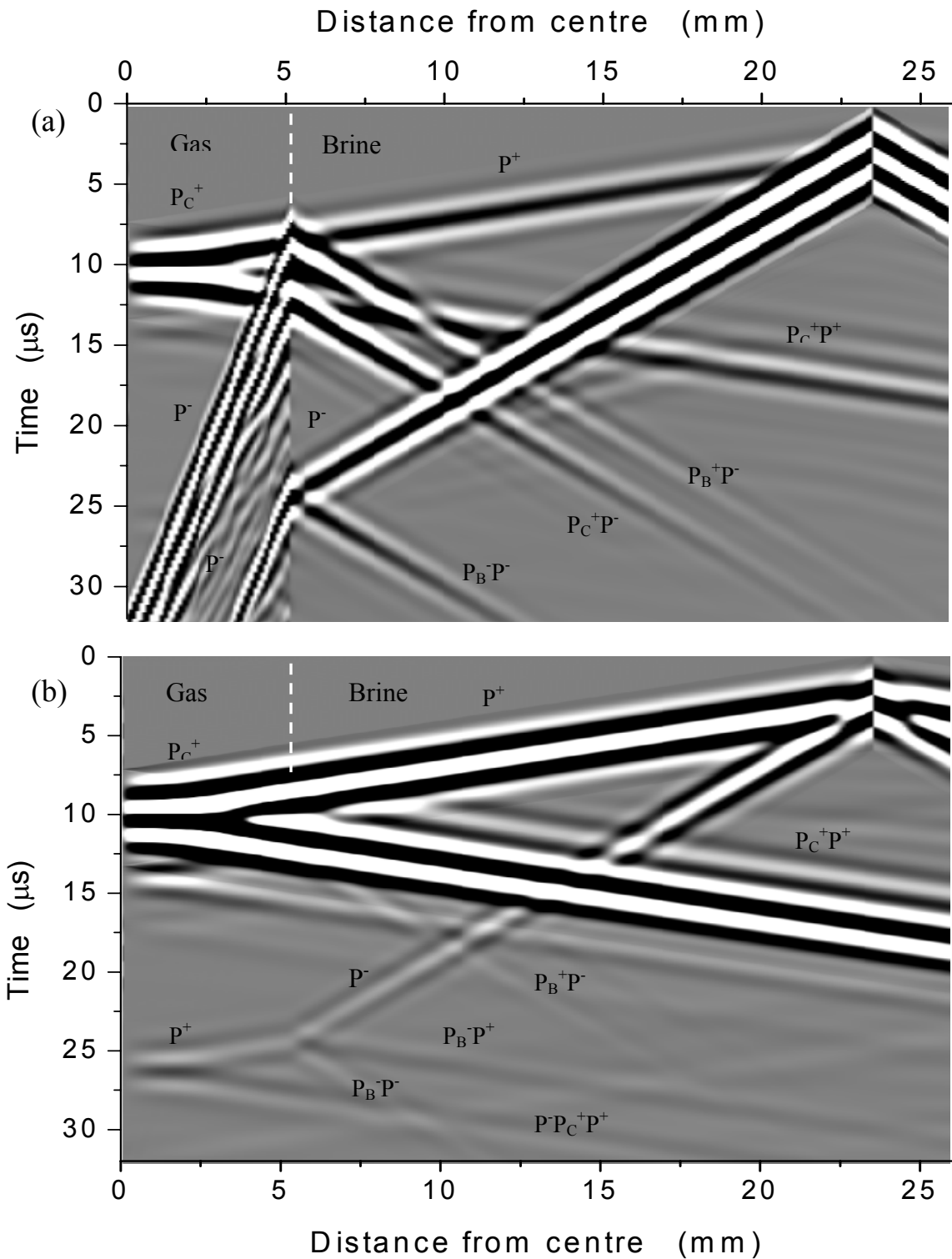


Figure 7.13: Seismograms of the fluid particle velocity relative to the solid (a) and particle velocity of the solid (b), corresponding to the model shown in Figure 7.10.

7.4 Conclusion

Fast P-wave conversion into slow P-waves is the dominant mechanism of wave dissipation and velocity dispersion in partially saturated rocks in the frequency range [10-500 kHz] (see also chapter 6). This phenomenon is observed in our numerical simulations, and is partially predicted by White's model, regarding the slow P-wave motion. This phenomenon is also described by Hudson (1988). Under compression, the liquid is driven into the space previously occupied by gas. Norris (1993) and Gurevich and Lopatnikov (1995), using alternating poro-elastic layers, have shown that attenuation and velocity dispersion measurements can be explained by the combined effect of layering and energy transfer between wave modes. If the fluid compressibility varies significantly from point to point, diffusion of pore fluid between different regions constitutes a mechanism that can be important at seismic frequencies. Carcione (1998) has observed this strong dissipation in numerical simulations of wave propagation in alternating plane layers saturated with water and gas. This phenomenon may explain the low signal-to-noise P-wave sections observed in some ocean bottom seismic data (Kommedal et al., 1997; Granli et al., 1999). In fact, the presence of gas, leaked from the reservoir to the overburden, has the effect of both lowering seismic velocities and increasing seismic attenuation, producing low signal-to-noise ratio P-wave sections. (This effect is not present in S-wave sections.)

In general, our simulations predict higher attenuation (although narrower relaxation peaks) and higher velocities than White's model. This is mainly due to additional wave dissipation due to multiple scattering and wave conversion. Moreover, White's model does not take into account local fluid flow (Gist, 1994) and (Biot) global fluid flow effects, while they are present in the numerical simulations (these effects increase the velocity). Other sources of discrepancy between model and numerical experiments can be attributed to the fact that the grid representations of gas pockets are not exactly circles, since the mesh is composed of rectangular cells. We obtain expressions for the relaxation critical frequency and critical saturation for which attenuation has a maximum value. Our simulations reproduce the trends regarding the location of the relaxation peaks as a function of frequency and saturation. That is, the peaks move towards higher water saturations for lower frequencies and higher permeabilities.

The final example shows an analysis of the wave field for a single gas pocket, modelling the conditions for which White (1975) has developed the theory. The physical phenomena involved in the problem are illustrated by this simulation. The conversion from fast to slow compressional wave and the multiple events generated at the gas bubble are clearly the main loss mechanisms for the primary pulse.

Chapter 8

Conclusions and future work

With a better understanding of rocks and porous media, together with a combination of the physical theory and observations on natural rocks, we are able to obtain a more comprehensive multi-phase model for shaley sandstones, which is a typical rock in hydrocarbon reservoirs. The model gives the elastic properties - wave velocity and quality factor - of sandstone as a function of clay content, pore pressure, frequency, and partial saturation. The theory includes fluid mixing laws in partial saturated rocks, viscoelasticity and viscodynamic effects to model the velocity dispersion and attenuation values observed in rocks from low (seismic) to high (ultrasonic) frequencies. The viscoelastic effect is included in the theory where a constant- Q model represents internal friction, thermal effects and other similar effects, and Zener's model presents for Squirt flow phenomena. Modelling of viscoelasticities requires first calibration to fit a general functional behaviour of quality factor (and velocity dispersion) versus frequency. Gas chimneys can also be however explained by elastic wave propagation (O'Brien et al., 1999). Here the gas zones are detected by using elastic modelling experiment.

For instance, the model predicts the behaviour of natural sandstones in many respects; i) Wave velocity increases considerably at high frequencies compared to low frequencies (the fluid has enough time to achieve pressure equilibration at low frequencies, while at high frequencies, the fluid cannot relax and the pores are stiffer than at low frequencies). ii) There is a strong decrease of the velocity and Q -factor with decreasing differential pressure (this effect is mainly due to the dry-rock moduli, which are sensitive functions of the effective pressure). The advantage of the model is that the frame moduli are not only a function of porosity and clay content but also of the pressure. iii) For a Berea sandstone the attenuation has maximum at approximately the location of the squirt flow peak and 90 % water saturation in sonic frequency range. iv) In general, attenuation increases with increasing clay content. However, attenuation is strongly

dependent on both clay content and fluid saturation. For shaley sandstone with gas, the attenuation has a peak in the sonic-frequency band, while the partially saturated sample has its relaxation peak at ultrasonic frequencies.

The method has been applied to the Tune field in the Viking Graben sedimentary basin of the North Sea (Carcione et al., 2002a). A high-resolution velocity map that reveals the sensitivity to pore pressure and fluid saturation in the Tarbert reservoir is obtained from 3-D pre-stack velocity by tomography and depth imaging. The pressure map predicted in Tabert formation has good agreement with the local well data and the structural features of the Tarbert formation and its known pressure compartments. The theory of model can be used for inversion applications such as sonic-log interpretation, pressure and fluid prediction, lithological inversion, AVO inversion, and others.

The limitation of the model relates to modelling of the viscoelasticity to describe attenuation mechanisms, which are not of viscodynamic nature (local and global fluid-flow losses). However, this limitation is a consequence of the absence of experimental data in the sonic and seismic bands, while reliable Q -factor measurements are difficult to obtain. The constant- Q model could be substituted by a generated Zener model (parallel or series connection of Zener elements), which can be used to fit a general functional behaviour of quality factor (and velocity dispersion). In this sense, the model is not a predicting tool. Due to lack of a micro-structural theory, we consider here the effective properties for the mixture in partially saturated rocks rather than the detailed flow patterns at pore scale, which are invisible to the waves commonly applied in field and laboratory experiments.

In future work, the model should be developed and improved in order to solve the limitations of multi-phase model and better describe the microscopic behaviours in the natural rocks (e.g., heterogeneity, crack, local flow). In addition, the fluids-distribution scale effect should be considered and taken into account. With more reliable Q -factor measurements the static mixing law for effective fluid properties could be developed for better describing the dynamic behaviours (at microscopic scale) in partially saturated rocks. Moreover the model should calibrate with experimental data in different frequency ranges, seismic (Hz), sonic (kHz) and ultrasonic (MHz) in order to better quantify and qualify the values of empirical parameters in the model such as the parameters of Krief et al. and of Brie et al., and others corresponding to different rock types. Despite the limitations, for instant, the multi-phase Biot-type model for shaley sandstones should be applied to hydrocarbon fields for detection and prediction of hydrocarbons, lithology and anomalies in pore pressure in the formation.

Using the numerical solution of the poro-elastic wave equation, based on Biot's theory, we are able to conduct wave propagation experiments in a rock sample with partial saturation, where the fluid distribution (gas/water) pattern is based on published tomography scans (Cadoret et al., 1995) and modelled using the random-fractal approach of Frankel and Clayton (1986). Furthermore, our numerical experiments of wave propagation are compared with those of White's theory for partial saturation (White, 1975). Without resorting to additional phenomenological matrix-fluid interaction mechanisms, we are able to reproduce the main features of published experiments (Cadoret et al., 1995, 1998; Murphy, 1982) on P-wave velocity and attenuation in partially saturated rocks at sonic and ultra-sonic frequencies [10-500 kHz]. By analysis of results, we arrive at the following conclusions: i) Wave propagation in porous rocks depend not only on the saturation but also on the distribution of the fluid phase at various scales. In the case of unknown fluid distribution, it is suggested that one should use the modified model of Brie et al. (1995) for mixing bulk moduli of the mixture (Pham et al., 2002c). ii) Fast P-wave conversion into slow P-waves and the multiple events generated at the gas bubbles is the main mechanism of wave dissipation and velocity dispersion in partially saturated rocks. This phenomenon may explain low signal-to-noise P-wave sections, since the present of gas, leaked from reservoir to the overburden, causes both lower seismic velocities and increased seismic attenuation (this effect is not present in S-wave sections). The dissipation of P-wave is less in case of heterogeneity in rock material, compared to fluid heterogeneity of equivalent seismic contrast. iii) The results reveal the strong responses of both P-wave velocity and attenuation corresponding to permeability, while at full saturation the sensitivity to permeability is insignificant. iv) Although the modelling is two-dimensional and the interaction between the gas pockets is neglected in White's model, the numerical results show the trends predicted by theory. Following White's theory, the main mechanism in partially saturated rocks is due to pressure equilibration, which induces partial fluid flows, and hence causes attenuation and velocity dispersion of the wave field. v) The expressions of the relaxation (critical) frequency (and critical saturation) for which attenuation has a maximum value, are obtained and are generally in good agreement with our simulations and White's model.

Numerical rock physics experiments provide full control on sample specifications and composition of the fluids. Since grid methods provide more monitoring options than possible in a physical experiment, the methods outlined in this study offer capabilities for designing and interpreting physical experiments.

The successful results of numerical rock physics experiments give a good guide for future work, i.e. the strong effects on P-wave propagation related to saturation distributions, the permeability and frequency. As discussed before, fluid-distribution scale is one of the key factors in affecting the acoustic properties. The saturation scale in a reservoir depends on several factors, porosity, saturation

history (drainage, imbibition), capillary pressure and others. In order to obtain the velocity and attenuation of seismic with the actual fluid-distribution scale in reservoir, we suggest the following processing sequence; 1) First, run reservoir simulation (Eclipse) to obtain the image of fluid saturation in the reservoir where the well data and geological model are required as input data, 2) Then simulate the synthetic data, based on the full-wave solution of the poro-elastic equations (Appendix B), in order to obtain more reliable results of P-wave velocity and attenuation, corresponding to the in-situ state of fluid distribution in reservoir.

Appendix A

Three-phase Biot-type theory of shaley sandstones

Saturated shaley sandstones require the consideration of a medium consisting of three phases: sand clay and fluid. A three-phase Biot-type theory first developed by Leclaire et al. (1994) explicitly takes into account the presence of three phases: solid, ice and water. Carcione et al. (2000) replaced the ice with clay and included the contributions to the potential and kinetic energies due to the contact between the sand grains and the clay.

The total potential energy of the system can be expressed as

$$\begin{aligned} E_p = & \frac{1}{2} K_{11} \theta_1^2 + \mu_{11} d_1^2 + K_{12} \theta_1 \theta_2 + \frac{1}{2} K_{22} \theta_2^2 \\ & + K_{23} \theta_2 \theta_3 + \frac{1}{2} K_{33} \theta_3^2 + \mu_{33} d_3^2 + K_{13} \theta_1 \theta_3, \end{aligned} \quad (\text{A-1})$$

where θ_i and d_i are the invariants of the strain tensor, called dilatations and deviators, while K_{ij} and μ_{ij} are respectively the bulk and shear moduli of the effective phases. The indices $i, j = 1, 2, 3$, denote sand, fluid, and clay, respectively.

For a three-phase medium the bulk stiffness matrix is

$$\begin{aligned} R_{11} &= K_{11} + 4/3 \mu_{11} = [(1-c_1)\phi_s]^2 K_{av} + 4/3 \mu_{11}, \\ R_{12} &= K_{12} = (1-c_1)\phi_s \phi K_{av}, \\ R_{13} &= K_{13} + 2/3 \mu_{13} = (1-c_1)(1-c_3)\phi_s \phi_c K_{av}, \\ R_{22} &= K_{22} = \phi^2 K_{av}, \\ R_{23} &= K_{23} = (1-c_3)\phi_c \phi K_{av}, \\ R_{33} &= K_{33} + 4/3 \mu_{33} = [(1-c_3)\phi_c]^2 K_{av} + 4/3 \mu_{33} \end{aligned} \quad (\text{A-2})$$

where

$$K_{av} = \left[(1-c_1) \frac{\phi_s}{K_s} + (1-c_3) \frac{\phi_c}{K_c} + \frac{\phi}{K_f} \right]^{-1},$$

$$c_1 = \frac{K_{sm}}{\phi_s K_s}, \quad c_3 = \frac{K_{cm}}{\phi_c K_c}, \quad \phi_s + \phi_c + \phi = 1$$

Here K_s , K_c and K_f are the sand, clay and fluid bulk moduli, respectively, K_{av} is the average bulk modulus, K_{sm} , K_{cm} are sand and clay matrix bulk modulus, ϕ_s , ϕ_c and ϕ are the proportion of sand, clay and porosity, respectively. The factors c_1 and c_3 are called the bulk consolidation coefficients for sand and clay, respectively, and are always between 0 and 1. For a nonconsolidated medium such as a suspension of sand grains in a fluid, $c_1 = 0$, while $c_1 = 1$ corresponds to a situation where the sand grains form a monolithic block.

The shear stiffness matrices are expressed as follows:

$$\begin{aligned} \mu_{11} &= \mu_{sm}, \\ \mu_{13} &= 0, \\ \mu_{33} &= \mu_{cm}, \end{aligned} \tag{A-3}$$

where μ_{sm} , μ_{cm} are sand and clay matrix bulk moduli.

The displacements of sand, fluid, and clay are respectively represented by the vectors u_1 , u_2 and u_3 . The kinetic energy density E_k is a function of the local velocities \dot{u}_1 , \dot{u}_2 and \dot{u}_3 given by the time derivative of displacements. With a development of E_k to the second order and assuming that the motion of any phase is only caused by the wave propagation,

$$E_k = \frac{1}{2} \rho_{11} \dot{u}_1^2 + \rho_{12} \dot{u}_1 \dot{u}_2 + \rho_{13} \dot{u}_1 \dot{u}_3 + \frac{1}{2} \rho_{22} \dot{u}_2^2 + \rho_{23} \dot{u}_2 \dot{u}_3 + \frac{1}{2} \rho_{33} \dot{u}_3^2. \tag{A-4}$$

We now want to determine the induced mass tensor ρ_{ij} . To obtain this purpose, we first deduce an expression for the kinetic energy through a microstructural argument and then compare the result with (A-4). Let us define the macroscopic velocities

$$\begin{aligned} \dot{w}_1 &= \phi(\dot{u}_2 - \dot{u}_1), \\ \dot{w}_3 &= \phi(\dot{u}_2 - \dot{u}_3), \end{aligned} \tag{A-5}$$

which describe the flow of fluid with respect to sand and clay, respectively. Likewise

$$\dot{q} = \phi_c(\dot{u}_3 - \dot{u}_1) \quad \text{and} \quad \dot{r} = \phi_s(\dot{u}_1 - \dot{u}_3) \quad (\text{A-6})$$

denote the macroscopic velocities characterising the movement of clay relative to the sand grains and vice versa, respectively. Since the relative flows are assumed to be of laminar type, the microscopic velocities can be expressed as

$$v_1 = \alpha_1 \dot{w}_1 \quad \text{and} \quad v_3 = \alpha_3 \dot{w}_3 \quad (\text{A-7})$$

and

$$s = \beta_1 \dot{q} \quad \text{and} \quad t = \beta_3 \dot{r}, \quad (\text{A-8})$$

where α_1 and α_3 are the fluid/sand and fluid/clay matrix coefficients, and β_1 and β_3 are the clay/sand and sand/clay matrix coefficients, respectively.

The total kinetic energy is given by the expression

$$\begin{aligned} E_k = & \frac{1}{2} \rho_f \iiint_{\Omega_f} (\dot{u}_1 + v_1)^2 d\Omega + \frac{1}{2} \rho_f \iiint_{\Omega_f} (\dot{u}_3 + v_3)^2 d\Omega + \\ & \frac{1}{2} \rho_c \iiint_{\Omega_c} (\dot{u}_1 + s)^2 d\Omega + \frac{1}{2} \rho_s \iiint_{\Omega_s} (\dot{u}_3 + t)^2 d\Omega - \frac{1}{2} \rho_f \phi \dot{u}_2^2, \end{aligned} \quad (\text{A-9})$$

where Ω_f , Ω_c , and Ω_s are the volumes of fluid, clay and sand, respectively.

Following Leclaire et al. (1994), we define

$$(m_{ij})^{(l)} \equiv \rho_f \iiint_{\Omega^{(l)}} \sum_k \alpha_{ki}^{(l)} \alpha_{kj}^{(l)} d\Omega, \quad l=1,3, \quad (\text{A-10})$$

$$(n_{ij})^{(1)} \equiv \rho_c \iiint_{\Omega_c} \sum_k \beta_{ki}^{(1)} \beta_{kj}^{(1)} d\Omega, \quad (\text{A-11})$$

$$(n_{ij})^{(3)} \equiv \rho_s \iiint_{\Omega_s} \sum_k \beta_{ki}^{(3)} \beta_{kj}^{(3)} d\Omega,$$

where $\Omega^{(1)} = \Omega_c$, $\Omega^{(3)} = \Omega_s$, $\alpha_{ij}^{(l)} = \alpha_l \delta_{ij}$ and $\beta_{ij}^{(l)} = \beta_l \delta_{ij}$.

Assuming statistical isotropy, we obtain $m_{ij}^{(l)} = m_l \delta_{ij}$ and $n_{ij}^{(l)} = n_l \delta_{ij}$, therefore (A-9) simplifies to

$$\begin{aligned}
E_k = & \frac{1}{2} \rho_2 \dot{u}_1^2 + \rho_f \dot{u}_1 \dot{w}_1 + \frac{1}{2} m_1 \dot{w}_1^2 + \frac{1}{2} \rho_2 \dot{u}_3^2 + \rho_f \dot{u}_3 \dot{w}_3 + \frac{1}{2} m_3 \dot{w}_3^2 \\
& - \frac{1}{2} \rho_2 \dot{u}_2^2 + \frac{1}{2} \rho_3 \dot{u}_1^2 + \rho_c \dot{u}_1 \dot{q} + \frac{1}{2} n_1 \dot{q}^2 + \frac{1}{2} \rho_1 \dot{u}_3^2 + \rho_s \dot{u}_3 \dot{r} + \frac{1}{2} n_3 \dot{r}^2,
\end{aligned} \tag{A-12}$$

where

$$\rho_1 = \rho_s \phi_s, \quad \rho_2 = \rho_f \phi, \quad \text{and} \quad \rho_3 = \rho_c \phi_c.$$

Finally, expressing the energy as a function of \dot{u}_1 , \dot{u}_2 and \dot{u}_3 , the equation (A-12) can be written as

$$\begin{aligned}
E_K = & \frac{1}{2} (n_3 \phi_s^2 - \rho_2 + m_1 \phi^2 - \rho_3 + n_1 \phi_c^2) \dot{u}_1^2 + \frac{1}{2} (m_1 \phi^2 + m_3 \phi^2 - \rho_2) \dot{u}_2^2 \\
& + \frac{1}{2} (n_1 \phi_c^2 - \rho_2 + m_3 \phi^2 - \rho_1 + n_3 \phi_s^2) \dot{u}_3^2 + (\rho_2 - m_1 \phi^2) \dot{u}_1 \dot{u}_2 \\
& + (\rho_2 - m_3 \phi^2) \dot{u}_2 \dot{u}_3 + (\rho_1 - n_3 \phi_s^2 + \rho_3 - n_1 \phi_c^2) \dot{u}_1 \dot{u}_3.
\end{aligned} \tag{A-13}$$

The generalised mass densities ρ_{ij} are obtained from the identification of the coefficients of expression (A-13) with those of (A-4). This gives

$$\begin{aligned}
\rho_{11} = & \rho_s \phi_s a_{13} + (a_{21} - 1) \rho_f \phi + (a_{31} - 1) \rho_c \phi_c, \\
\rho_{22} = & (a_{21} + a_{23} - 1) \rho_f \phi, \\
\rho_{33} = & \rho_c \phi_c a_{31} + (a_{23} - 1) \rho_f \phi + (a_{13} - 1) \rho_s \phi_s, \\
\rho_{12} = & -(a_{21} - 1) \rho_f \phi, \\
\rho_{23} = & -(a_{23} - 1) \rho_f \phi, \\
\rho_{13} = & -(a_{13} - 1) \rho_s \phi_s - (a_{31} - 1) \rho_c \phi_c,
\end{aligned} \tag{A-14}$$

where

$$\begin{aligned}
a_{21} = & \frac{m_1 \phi}{\rho_f}, \quad a_{23} = \frac{m_3 \phi}{\rho_f}, \\
a_{13} = & \frac{n_3 \phi_s}{\rho_s}, \quad a_{31} = \frac{n_1 \phi}{\rho_c}
\end{aligned} \tag{A-15}$$

are the tortuosity parameters.

When there is no relative motion between the three phases, the following relationship holds

$$\rho \equiv \rho_{11} + \rho_{22} + \rho_{33} + 2(\rho_{12} + \rho_{23} + \rho_{13}) = \rho_1 + \rho_2 + \rho_3, \tag{A-16}$$

where ρ may be viewed as the effective mass density.

In order to obtain the viscous flow resistance coefficients b_{11} and b_{33} , we first consider the idealised situation when the solid part can be modelled as a dilute concentration of sand and clay spherical particles in the fluid. This situation is realised in the high porosity limit ($\phi \rightarrow 1$). Since the concentration is dilute, each particle can be considered independently from the others. The viscous resistance force for a single sphere of radius R moving in a flow of average velocity V and a fluid viscosity η_f obeys Stokes' law,

$$F = 6\pi\eta_f VR. \quad (\text{A-17})$$

Suppose that in a unit volume we have N_i particles of radius R_i , where $i = 1$ (sand grains) or 3 (clay particles). Then, the viscous resistance to the flow by particles of type i can be written as

$$F_i = 6\pi\eta_f VN_i R_i. \quad (\text{A-18})$$

The density numbers N_i can be thought of as the total volume of the particles of type i divided by the volume of a single particle,

$$N_i = \frac{\phi_i}{\frac{4}{3}\pi R_i^3}. \quad (\text{A-19})$$

Substitution of (A19) into (A18) yields

$$F_i = \frac{9}{2}\eta_f V \phi_i R_i^{-2}, \quad (\text{A-20})$$

or, for the viscous resistance coefficient,

$$b_{ii} = F_i \frac{\phi_i^2}{V} = \frac{9}{2}\eta_f \phi_i^2 \phi_i R_i^{-2}. \quad (\text{A-21})$$

Note that the quantity

$$\kappa_i = \frac{2}{9} \frac{R_i^2}{\phi_i} \quad (\text{A-22})$$

can be thought of as a partial permeability of the matrix formed by particles of type i . Hence

$$b_{ii} = \frac{\eta_f \phi}{\kappa_i}. \quad (\text{A-23})$$

Appendix B

Numerical algorithm for wave propagation in poro-elastic isotropic media

The theory of seismic wave propagation in porous media is modelled based on Biot's theory and developed by Carcione (1998). In a porous medium, the particle velocity in the fluid is in general different from the particle velocity in the solid. This differential motion causes the existence of two P-waves, a fast P-wave and a slow P-wave.

The fast P-wave has solid and fluid displacements in phase, and the slow compressional wave has out of phase displacement. The slow wave is generated by conversion at heterogeneities.

The constitutive equations for an inhomogeneous, transversely isotropic poro-elastic medium under plane strain conditions are given by [Biot and Willis (1957); Biot 1962]

$$\partial_t \tau_{xx} = E \partial_x v_x + (E - 2\mu) \partial_z v_z + \alpha M \varepsilon + s_x, \quad (\text{B-1})$$

$$\partial_t \tau_{zz} = (E - 2\mu) \partial_x v_x + E \partial_z v_z + \alpha M \varepsilon + s_z, \quad (\text{B-2})$$

$$\partial_t \tau_{xz} = \mu (\partial_z v_x + \partial_x v_z) + s_{xz}, \quad (\text{B-3})$$

$$\partial_t p = -M \varepsilon + s_f, \quad (\text{B-4})$$

and

$$\varepsilon = \alpha (\partial_x v_x + \partial_z v_z) + \partial_x q_x + \partial_z q_z, \quad (\text{B-5})$$

where τ_{xx} , τ_{zz} , and τ_{xz} are the total stresses in component, p is the fluid pressure, v and q are the solid and fluid (relative to the solid) particle velocities, and s_x , s_z , s_{xz} and s_f are the external sources of stress, respectively.

The elastic coefficients are given by

$$E = K_m + \frac{4}{3} \mu, \quad (\text{B-6})$$

$$M = \frac{K_s^2}{D - K_m}, \quad (\text{B-7})$$

$$D = K_s \left[1 + \phi \left(\frac{K_s}{K_f} - 1 \right) \right], \quad (\text{B-8})$$

$$\alpha = 1 - \frac{K_m}{K_s}, \quad (\text{B-9})$$

where K_m , K_s and K_f are the bulk moduli of the drained matrix, the solid and the fluid, respectively. The stiffness E is the P-wave modulus of dry skeleton, M is the coupling modulus between the solid and the fluid, and ε is the poroelastic coefficient of the effective stress.

The dynamical equations are derived, based on Biot's theory, as

$$\partial_x \tau_{xx} + \partial_z \tau_{xz} = \rho \partial_t v_x + \rho_f \partial_t q_x, \quad (\text{B-10})$$

$$\partial_x \tau_{xz} + \partial_z \tau_{zz} = \rho \partial_t v_z + \rho_f \partial_t q_z, \quad (\text{B-11})$$

where ρ and ρ_f are the total and fluid densities, respectively.

On the other hand, the pressure can be expressed, based on Darcy's law

$$-\partial_x p = \rho_f \partial_t v_x + m \partial_t q_x + \frac{\eta}{\kappa} q_x, \quad (\text{B-12})$$

$$-\partial_z p = \rho_f \partial_t v_z + m \partial_t q_z + \frac{\eta}{\kappa} q_z, \quad (\text{B-13})$$

where $m = T\rho_f/\phi$, T denotes the tortuosity, η is the fluid viscosity and κ is the permeability of the isotropic medium.

From equations (B-10), (B-11), (B-12), and (B-13) the velocity-stress formulation of the poro-elastic equations is obtained

$$-\partial_t v_x = \beta_{11} (\partial_x \tau_{xx} + \partial_z \tau_{xz}) - \beta_{12} \left(\partial_x p + \frac{\eta}{\kappa} q_x \right), \quad (\text{B-14})$$

$$-\partial_t v_z = \beta_{11} (\partial_x \tau_{xz} + \partial_z \tau_{zz}) - \beta_{12} \left(\partial_z p + \frac{\eta}{\kappa} q_z \right), \quad (\text{B-15})$$

$$-\partial_t q_x = \beta_{21} (\partial_x \tau_{xx} + \partial_z \tau_{xz}) - \beta_{22} \left(\partial_x p + \frac{\eta}{\kappa} q_x \right), \quad (\text{B-16})$$

$$-\partial_t q_z = \beta_{21} (\partial_x \tau_{xz} + \partial_z \tau_{zz}) - \beta_{22} \left(\partial_z p + \frac{\eta}{\kappa} q_z \right), \quad (\text{B-17})$$

where

$$\begin{bmatrix} \beta_{11} & \beta_{12} \\ \beta_{21} & \beta_{22} \end{bmatrix} = (\rho_f^2 - \rho m)^{-1} \begin{bmatrix} -m & \rho_f \\ \rho_f & -\rho \end{bmatrix}. \quad (\text{B-18})$$

The system of equations for wave motion (B-1, ..., B-4, B-14, ..., B-17) can be written in matrix form as

$$\partial_t \mathbf{W} = \mathbf{M}\mathbf{W} + \mathbf{S}, \quad (\text{B-19})$$

where

$$\mathbf{M} = \begin{pmatrix} 0 & 0 & -\beta_{12} \frac{\eta}{\kappa} & 0 & -\beta_{11} \frac{\partial}{\partial x} & 0 & -\beta_{11} \frac{\partial}{\partial z} & -\beta_{12} \frac{\partial}{\partial x} \\ 0 & 0 & 0 & -\beta_{12} \frac{\eta}{\kappa} & 0 & -\beta_{11} \frac{\partial}{\partial z} & -\beta_{11} \frac{\partial}{\partial x} & -\beta_{12} \frac{\partial}{\partial z} \\ 0 & 0 & -\beta_{22} \frac{\eta}{\kappa} & 0 & -\beta_{21} \frac{\partial}{\partial x} & 0 & -\beta_{21} \frac{\partial}{\partial z} & -\beta_{22} \frac{\partial}{\partial x} \\ 0 & 0 & 0 & -\beta_{22} \frac{\eta}{\kappa} & 0 & -\beta_{21} \frac{\partial}{\partial z} & -\beta_{21} \frac{\partial}{\partial x} & -\beta_{22} \frac{\partial}{\partial z} \\ (E + \alpha^2 M) \frac{\partial}{\partial x} & (E - 2\mu + \alpha^2 M) \frac{\partial}{\partial z} & \alpha M \frac{\partial}{\partial x} & \alpha M \frac{\partial}{\partial z} & 0 & 0 & 0 & 0 \\ (E - 2\mu + \alpha^2 M) \frac{\partial}{\partial x} & (E + \alpha^2 M) \frac{\partial}{\partial z} & \alpha M \frac{\partial}{\partial x} & \alpha M \frac{\partial}{\partial z} & 0 & 0 & 0 & 0 \\ \mu \frac{\partial}{\partial z} & \mu \frac{\partial}{\partial x} & 0 & 0 & 0 & 0 & 0 & 0 \\ -\alpha M \frac{\partial}{\partial x} & -\alpha M \frac{\partial}{\partial z} & -M \frac{\partial}{\partial x} & -M \frac{\partial}{\partial z} & 0 & 0 & 0 & 0 \end{pmatrix}$$

and

$$\mathbf{W} = \begin{pmatrix} v_x \\ v_z \\ q_x \\ q_z \\ \sigma_{xx} \\ \sigma_{zz} \\ \sigma_{xz} \\ p_f \end{pmatrix}, \quad \text{and} \quad \mathbf{S} = \begin{pmatrix} 0 \\ 0 \\ 0 \\ 0 \\ s_x \\ s_z \\ s_{xz} \\ s_f \end{pmatrix}.$$

Here, the matrix, \mathbf{W} is a vector that represents the wave-field, \mathbf{M} is the propagation matrix, which contains the spatial derivatives and material properties, and \mathbf{S} is the source vector.

The source time function is a Ricker wavelet with central frequency f_c , given by

$$f(t) = e^{\left[\frac{-1}{2}(t-t_0)^2 \right]} \cos[\pi f_c (t-t_0)], \quad (\text{B-20})$$

where $t_0 = 3/f_c$.

Considering the 1-D version of eq. (B-19) with $\mathbf{S} = 0$, the plane wave

$$\mathbf{W} = \mathbf{W}_0 e^{i(\omega_c t - kx)}, \quad (\text{B-21})$$

where ω_c is the complex frequency and k is the wave number, is a solution of eq. (B-19) and gives an eigenvalue equation for the eigenvalues $\lambda = i\omega_c$. When using the Fourier pseudospectral method for computing the spatial derivatives, the wave numbers supported by the numerical mesh span from $k = 0$ to the Nyquist wave number $k = \pi/\Delta x$ where Δx is the grid spacing. It is shown that the eigenvalues come in complex conjugate pairs (Carcione and Quiroga-Goode, 1995). When the fluid viscosity is zero, they lie on the imaginary axis, and describe propagating modes without dissipation. For a viscous fluid, the eigenvalues have a negative real part meaning that the waves are attenuated, in particular the slow wave. To be precise, the largest negative eigenvalue corresponds to the slow wave for $k = 0$:

$$\lambda_s = -\left(\frac{\eta}{\kappa}\right)\beta_{22}. \quad (\text{B-22})$$

In order to have numerical stability, the domain of convergence of the time integration scheme should include this eigenvalue. For instance, an explicit fourth-order Runge-Kutta method (Jain, 1984, p. 71) requires $dt\lambda_s > -2.78$, implying a very small time step dt . In this case, the method is restricted by numerical stability rather than by accuracy. The presence of this large eigenvalue, together with small eigenvalues, indicates that the problem is stiff. In stiff problems, the solution to be computed is slowly varying but perturbations exist that are rapidly damped. In this case, the perturbation is the slow wave, which, in the presence of fluid viscosity, displays a diffusive character.

As mentioned above, the spatial derivatives are calculated with the Fourier method by using the FFT (Fast Fourier Transform). This approximation is infinitely accurate for band limited periodic functions with cutoff spatial wave numbers, which are smaller than the cutoff wave number of the mesh. The stability problem posed by the eigenvalue λ_s can be solved if an A-table method (Jain, 1984) is used, implying stability in the open left-half-plane. A better time integration technique can be achieved by using a partition method (Carcione and Quiroga-Goode, 1995). Here, the system can be partitioned into two set of differential equations, one stiff and the other nonstiff, such that they can be

treated by two different methods, one implicit and the other explicit, respectively. The stiff equations

$$\partial_t v_x = \frac{\eta}{\kappa} \beta_{12} q_x \quad (\text{B-23})$$

$$\partial_t v_z = \frac{\eta}{\kappa} \beta_{12} q_z \quad (\text{B-24})$$

$$\partial_t q_x = \frac{\eta}{\kappa} \beta_{22} q_x \quad (\text{B-25})$$

$$\partial_t q_z = \frac{\eta}{\kappa} \beta_{22} q_z \quad (\text{B-26})$$

can be solved analytically, giving

$$\partial_t v_x^* = v_x^n - \frac{\beta_{12}}{\beta_{22}} (e^{-\lambda_s dt} - 1) q_x^n \quad (\text{B-27})$$

$$\partial_t v_z^* = v_z^n - \frac{\beta_{12}}{\beta_{22}} (e^{-\lambda_s dt} - 1) q_z^n \quad (\text{B-28})$$

$$\partial_t q_x^* = (e^{-\lambda_s dt}) q_x^n \quad (\text{B-29})$$

$$\partial_t q_z^* = (e^{-\lambda_s dt}) q_z^n \quad (\text{B-30})$$

Note that, when $\eta = 0$, is $v^* = v^n$ and $q^* = q^n$, giving the pure elastic problem.

The next step is to solve the nonstiff part by using an explicit method; a 4 th-order Runge-Kutta algorithm is applied to solve equation (B-19)

$$\mathbf{W}^{n+1} = \mathbf{W}^* + \frac{dt}{6} (\Delta_1 + 2\Delta_2 + 2\Delta_3 + \Delta_4) \quad (\text{B-31})$$

where $\mathbf{W}^* = [v_x^*, v_z^*, q_x^*, q_z^*, \tau_{zz}^n, \tau_{xz}^n, p^n]^T$ is the input, and

$$\Delta_1 = \mathbf{M}\mathbf{W}^* + \mathbf{S}^n \quad (\text{B-32})$$

$$\Delta_2 = \mathbf{M} \left(\mathbf{W}^* + \frac{dt}{2} \Delta_1 \right) + \mathbf{S}^{n+\frac{1}{2}} \quad (\text{B-33})$$

$$\Delta_3 = \mathbf{M} \left(\mathbf{W}^* + \frac{dt}{2} \Delta_2 \right) + \mathbf{S}^{n+\frac{1}{2}} \quad (\text{B-34})$$

$$\Delta_4 = \mathbf{M} (\mathbf{W}^* + dt \Delta_3) + \mathbf{S}^{n+1} \quad (\text{B-35})$$

The advantage of the partition method is that the time step is determined by the algorithm that solves the nonstiff equations.

Since a geophone receiver detects the motion of the bulk, we follow Sahay (1994) and express the centre of mass particle velocity vector by

$$\boldsymbol{\Psi} = \mathbf{v} + \left(\frac{\rho_f}{\rho} \right) \mathbf{q}, \quad (\text{B-36})$$

where \mathbf{v} and \mathbf{q} are the solid and fluid particle velocity vectors, respectively.

References

- Akbar, N., Dvorkin J. and Nur, A., 1993, Relating P-wave attenuation to permeability, *Geophysics* **58**, 20-29.
- Audet, D. M., 1996, Compaction and overpressuring in Pleistocene sediments on the Louisiana shelf, Gulf of Mexico, *Marine and Petroleum Geology*, **13**, 467-474.
- Batzle M., Hofmann R., 2001, Fluids and frequency dependent seismic velocity of rocks, *The Leading Edge*, **20**, 168.
- Ben-Menahem A. and Singh, S. J., 1981, *Seismic waves and sources*. Springer.
- Bear, J., and Bachmar, Y., 1990, *Introduction to modeling of transport phenomena in porous media*, Kluwer Academic. Pub.
- Belotti, P, and Giacca, D., 1978, Seismic data can detect overpressure in deep drilling, *Oil and Gas Journal*, August issue.
- Berryman, J. G., 1980, Confirmation of Biot's theory, *Applied Physical Letters* **37**, 382-384.
- Berryman, J. G., 1992, Effective stress for transport properties of inhomogeneous porous rock, *Journal of Geophysical Research*, **97**, 17409-17424.
- Berryman, J. G., 1995, Mixture theories for rock properties. in Ahrens, T. J., ed., *Rock Physics and Phase Relations. A Handbook of Physical Constants*, 205-228.
- Best, M. E., Cant, D. J., Mudford, B. S., and Rees, J. L., 1990, Can velocity inversion help map overpressure zones?. Examples from an offshore margin, 60th Ann. Internat. Mtg., Soc. Expl. Geophys.. Expanded Abstracts, 763-765.
- Best, A. I., McCann, C. and Sothcott, J., 1994, The relationships between the velocities, attenuation and petrophysical properties of reservoir sedimentary rocks, *Geophysical Prospecting*, **42**, 151-178.
- Bilgeri, D., and Ademenio, E. B., 1982, Predicting abnormally pressured sedimentary rocks, *Geophysical Prospecting*, **30**, 608-621.

- Biot, M. A., 1956. Theory of propagation of elastic waves in a fluid saturated porous solid. I. Low frequency range and II. Higher-frequency range, *Journal of the Acoustical Society of America*, **28**, 168-191.
- Biot, M. A., 1962, Mechanics of deformation and acoustic propagation in porous media, *J. Appl. Phys.*, **33**, 1482-1498.
- Biot, M. A. and Willis, D. G., 1957, The influence of the theory of consolidation, *J. Appl. Mech.*, **24**, 594-601.
- Bland, D. R., 1960, *The theory of linear viscoelasticity*, Pergamon Press Inc.
- Blair, D. P., 1990, A direct comparison between vibrational resonance and pulse transmission data for assessment of seismic attenuation in rock, *Geophysics*, **55**, 51-60.
- Bourbié, T., Coussy, O., and Zinszner, B., 1987, *Acoustics of porous media*, Éditions Technip.
- Bourbié, T. and Zinszner, B., 1984, Saturation methods and attenuation versus saturation relationships in Fontainebleau sandstone. 54th SEG meeting, Atlanta, Expanded Abstracts, 344-347.
- Bowers, G. L., 1995, Pore pressure estimation from velocity data Accounting for overpressure mechanisms besides undercompaction, IADC/SPE Drilling Conf., #27488, 515-530.
- Gregory, A. R., 1976, Fluid saturation effects on dynamic elastic properties of sedimentary rocks, *Geophysics*, **41**, 895-921.
- Brie, A., Pampuri, F., Marsala, A. F., and Meazza, O., 1995, Shear sonic interpretation in gas-bearing sands, SPE Annual Technical Conf., #30595, 701-710.
- Bryant, T. M., 1989, A dual pore pressure detection technique, SPE #18714.
- Cadoret, T., Marion, D., and Zinszner, B., 1995, Influence of frequency and fluid distribution on elastic wave velocities in partially saturated limestones, *Journal of Geophysical Research*, **100**, 9789-9803.
- Cadoret, T., Mavco G., and Zinszner, B., 1998, Fluid distribution effect on sonic attenuation in partially saturated limestones, *Geophysics*, **63**, 154-160.

Carcione, J. M., 1996, Wave propagation in anisotropic, saturated porous media: Plane-wave theory and numerical simulation, *Journal of the Acoustical Society of America*, **99**, 2655-2666.

Carcione, J. M., 1998, Viscoelastic effective rheologies for modeling wave propagation in porous media, *Geophysical Prospecting*, **46**, 249-270.

Carcione, J. M., 2001a, Energy balance and fundamental relations in dynamic anisotropic poro-viscoelasticity, *Proc. Roy. Soc. London A*, **457**, 331-348.

Carcione, J. M., 2001b, Wave fields in real media: Wave propagation in anisotropic, anelastic and porous media: *Handbook of Geophysical Exploration*, vol. **31**, Pergamon Press Inc.

Carcione, J. M., 2001c, Amplitude variations with offset of pressure-seal reflections, *Geophysics*, **66**, 283-293.

Carcione, J. M., Cavallini, F., and Mainardi, F., and Hanyga, A., 2001a, Time-domain seismic modeling of constant Q -wave propagation using fractional derivatives, *PAGEOPH*, **159** (7), 1719-1736.

Carcione, J. M., Helle, H. B., Pham, N. H., and Toverud, T., 2001b, Pore pressure estimation from seismic reflection data. Expanded abstract at EAGE/SEG Research Workshop on Reservoir Rocks-Pau, France, 30 April - 4 May, 2001.

Carcione, J. M., and Gangi, A., 2000a, Non-equilibrium compaction and abnormal pore-fluid pressures: effects on seismic attributes, *Geophysical Prospecting*, **48**, 521-537.

Carcione, J. M., and Gangi, A., 2000b, Gas generation and overpressure: effects on seismic attributes, *Geophysics*, **65**, 1769-1779.

Carcione, J. M., Gurevich, B. and Cavallini, F., 2000, A generalized Biot-Gassmann model for the acoustic properties of clayey sandstones, *Geophysical Prospecting*, **48**, 539-557.

Carcione, J. M. and Helle, B. H., 1999, Numerical simulation of the poro-viscoelastic wave equation on a staggered mesh, *J. Comp. Phys.*, **154**, 520-527.

Carcione, J. M., Helle, H. B., Pham, N. H., and Toverud, T., 2002a, Pore pressure estimation from seismic reflection data. Accepted for publication in *Geophysics*.

Carcione, J. M., Helle, H. B., Pham, N. H., 2002b, White's model for wave propagation in partially saturated rocks: Comparison with poroelastic numerical experiments. Accepted for publication in *Geophysics*.

- Carcione, J. M., and Quiroga-Goode, G., 1995, Some aspects of the physics and numerical modelling of Biot compressional waves, *J. Comput. Acoust.*, **3**, 261-280.
- Carcione J. M. and Seriani G. 1998. Seismic velocities in permafrost, *Geophysical Prospecting*, **46**, 441-454.
- Carcione, J. M., and Tinivella, U., 2001, The seismic response to overpressure: a modeling methodology based on laboratory, well and seismic data. Accepted for publication in *Geophysical Prospecting*.
- Carman, P. C., 1961, L'écoulement des gaz à travers les milieux, *Bibliothèque des Sciences et Techniques nucléaires*, Presses Universitaires de France, Paris.
- Childs, C., Manzocchi, T., Nell, P. A. R., Walsh, J. J., Strand, J. A., Heath, A. E., and Lygren, T. H., 2001, Geological implications of a large pressure difference across a small fault in the Viking Graden, *in* Hydrocarbon Seal Quantification. (Koestler, A. G. and Hunsdale, R., Eds.). Submitted Norwegian Petroleum Society (NPF), Special Publication.
- Christensen I. N., Wang, F. H., 1985, The influence of pore pressure and confining pressure on dynamic elastic properties of Berea sandstone, *Geophysics*, **50**, 207-213.
- Domenico S. N., 1977, Elastic properties of unconsolidated porous sand reservoirs, *Geophysics*, **42**, 1339-1368.
- Dullien, F. A. L., 1991, One and two phase flow in porous media and pore structure, in Bideau, D., and Dodds, J., eds, *Physics of Granular Media*, Science Publishers Inc., New York, 173-214.
- Dutta, N. C. and Levin, F. K., 1990, Geopressure, *Geophysical Reprint Series No. 7*, Society of Exploration Geophysicists.
- Dutta, N. C. and Odé, 1979, Attenuation and dispersion of compressional waves in fluid-filled porous rock with partial gas saturation (White model) – Part II: Results, *Geophysics*, **44**, 1789-1805.
- Dutta, N. C. and Seriff A. J., 1979, On White's model of attenuation in rocks with partial gas saturation, *Geophysics*, **44**, 1806-1812.
- Dvorkin, J., Nolen-Hoeksema, R. and Nur, A., 1994, The squirt-flow mechanism: Macroscopic description, *Geophysics*, **59**, 428-438.

Eaton, B. A., 1976, Graphical method predicts geopressure worldwide, *World Oil*, July issue, 100-104.

Eaton, B. A., and Eaton, T. L., 1997, Fracture gradient prediction for the new generation, *World Oil*, October issue, 93-100.

Endres, A., Knight, R., 1989, The effect of microscopic fluid distribution on elastic wave velocities, *The Log Analyst*, **30**, 437-445.

Endres, A., Knight, R., 1991, The effect of pore scale fluid distribution on the physical properties of partially saturated tight sandstones, *J. Appl. Phy.*, **69**, 1091-1098.

Fagin S., 1998, *Model-Based Depth Imaging*. Society of Exploration Geophysicists, Course Notes Series, **10**.

Fedorov, F. I., 1968, *Theory of elastic waves in crystals*, Plenum Press.

Foster, J. B., and Whalen, J. E., 1966, Estimation of formation pressures from electrical surveys offshore Louisiana, *Journal of Petroleum Technology*, February issue.

Frankel, A., and Clayton, R. W., 1986. Finite difference simulation of seismic wave scattering: implications for the propagation of short period seismic waves in the crust and models of crustal heterogeneity, *J. Comp. Phys.*, **154**, 520-527.

Gangi, A. F., Carlson, L. R., 1996, An asperity-deformation model for effective pressure, *Tectonophysics*, **256**, 241-251.

Gassmann, F., 1951, Über die elastizität poröser medien, *Vierteljahrsschrift der Naturforschenden Gesellschaft in Zurich*, **96**, 1-23.

Gist, G. A., 1994, Interpreting laboratory velocity measurements in partially gas saturated rocks, *Geophysics*, **59**, 1100-1109.

Goldberg, I., and Gurevich, B., 1998, A semi-empirical velocity-porosity-clay model for petrophysical interpretation of P- and S- velocities, *Geophysical Prospecting*, **46**, 271-285.

Granli, J. R., Arntsen, B., Sollid, A. and Hilde, E., 1999, Imaging through gas-filled sediments using marine shear-wave data, *Geophysics, Soc. of Expl. Geophys.*, **64**, 668-677.

Gregory A. R. 1976, Fluid saturation effects on dynamic elastic properties of sedimentary rocks, *Geophysics*, **41**, 895-921.

Gurevich, B., and Lopatnikov, S. L., 1995, Velocity and attenuation of elastic waves in finely layered porous rocks, *Geophysical Journal International*, **121**, 933-947.

Han, D. H., Nur, A., and Morgan, D., 1986, Effects of porosity and clay content on wave velocities in sandstones: *Geophysics*, **51**, 2093-2107.

Harrold, T. W. D., Swarbrick, R. E., and Goult, N. R., 1999, Pore pressure estimation from mudrock porosities in tertiary basins, Southeast Asia, *AAPG Bulletin*, **83**, 1057-1067.

Hart, B. S., Flemings, P. B., and Desphande, A., 1995, Porosity and pressure: role of compaction disequilibrium in the development of geopressures in a Gulf Coast Pleistocene basin, *Geology*, **23**.

Hashin, Z., and Shtrikman, S., 1963, A variational approach to the elastic behavior of multiphase materials, *J. Mech. Phys. Solids*, **11**, 127-140.

Helle, H. B., Bhatt, A. and Ursin, B., 2001, Porosity and permeability from wireline logs using artificial neural networks: a North Sea case study, *Geophysical Prospecting*, **49**, 431-444.

Helle, H. B., Pham N. H., and Carcione, J. M., 2002a, Velocity and attenuation in partially saturated rocks – Poroelastic numerical experiments. Submitted to *Geophysical Prospecting*.

Helle, H. B., Pham N. H., and Carcione, J. M., 2002b, Effects of heterogeneities in fluid and rock properties on wave velocity and attenuation - Numerical experiments. Expanded abstract at EAGE 64th Conference & Exhibition - Florence, Italy, 27-30 May, 2002.

Hill, R. 1963, Elastic properties of reinforced solids: Some theoretical principles: *J. Mech. Phys. Solids*, **11**, 357-372.

Holbrook, P., Maggiori, D. A., and Hensley, R., 1995, Real time pore pressure and fracture pressure determination in all sedimentary lithologies, *SPE Formation Evaluation*, December issue, 215-222.

Hudson, J. A., 1988, Seismic wave propagation through materials containing partially saturated cracks, *Geophysical Journal International*, **92**, 33-37.

Hudson, J. A., Liu, E., and Crampin, S., 1996, The mechanical properties of materials with interconnected cracks and pores, *Geophysical Journal International*, **124**, 105-112.

Jacobson, C. I., 2000, An assessment of factors controlling permeability behaviour with pressure, MSc Thesis, PRIS, University of Reading/ NH-E&P Research Centre R-091250.

Jain, M. K., 1984, Numerical Solutions of Differential Equations, Wiley Eastern, New Delhi.

Johnson, D. L., 2001, Theory of frequency dependent acoustics in patchy-saturated porous media, Journal of the Acoustical Society of America, **110**, 682-694.

Johnson, D. L., Koplik, J., and Dashen, R., 1987, Theory of dynamic permeability and tortuosity in fluid-saturated porous media: J. Fluid Mech., **176**, 379-402.

Kan, T. K., and Sicking, C. J., 1994, Pre-drill geophysical methods for geopressure detection and evaluation in abnormal formation pressures, Chapman, R. Ed., Elsevier, 155-186.

Keller, J. D., 1989, Acoustic wave propagation in composite fluid-saturated media, Geophysics, **54**, 1554-1563.

Keyser, W. Johnston, L. Reeses, R., and Rodriguez, G., 1991, Pore pressure prediction from surface seismic, World Oil, 212, September issue, 115-125.

King, M. S., Marsden, J. R., and Dennis, J. W., 2000, Biot dispersion for P- and S-waves velocities in partially and fully saturated sandstones, Geophysical Prospecting, **48**, 1075-1089.

Kjartansson, E., 1979, Constant Q -wave propagation and attenuation, Journal of Geophysical Research, **84**, 4737-4748.

Klimentos, T., and McCann, C., 1988, Why is the Biot slow compressional wave not observed in real rocks?, Geophysics, **12**, 1605-1609.

Klimentos, T., and McCann, C., 1990, Relationships among compressional wave attenuation, porosity, clay content, and permeability in sandstones, Geophysics, **55**, 998-1014.

Knight, R. and Dvorkin, J., 1992, Seismic and electrical properties of sandstones at low saturations, Journal of Geophysical Research, **97**, 17425-17432.

- Knight R. and Nolen-Hoecksema R. 1990, A laboratory study of the dependence of elastic wave velocities on pore scale fluid distribution, *Geophysical Research Letters*, **17**, 1529-1532.
- Kommedal, J. H., Barkved, O. I., and Thomsen, L., 1997, Acquisition of 4 component OBS data - A case study from the Valhall field, 59th Ann. Internat. Mtg. Europ. Assoc. Expl. Geophys.. Expanded Abstracts, B047.
- Koren, Z., Kosloff, D. Zackhem, U., and Fagin, S., 1998, Velocity model determination by tomography of depth migrated gathers, in S. Fagin, ed., *Model-Based Depth Imaging*, Society of Exploration Geophysicist, Course Note Series Nr. 10, 119-130.
- Krief, M., Garat, J., Stellingwerff, J., and Ventre, J., 1990, A petrophysical interpretation using the velocities of P and S waves (full waveform sonic), *The log Analyst*, **31**, 355-369.
- Lecleire Ph., Cohen-Ténoudji F. and Aguirre-Puente J., 1994. Extension of Biot's theory of wave propagation to frozen porous media. *Journal of the Acoustical Society of America*, **96**, 3753-3768.
- Lesso, W. G. Jr., and Burgess, T. M., 1986, Pore pressure and porosity from MWD measurements, IADC /SPE Drilling Conf., #14801.
- Lucet N. and Zinszner B., 1992. Effect of heterogeneities and anisotropy on ultrasonic attenuation in rocks, *Geophysics*, **57**, 1018-1026.
- Luo, X., and Vasseur, G., 1996, Geopressuring mechanism of organic matter cracking: numerical modeling, *AAPG Bull.*, **80**, 856-874.
- Mann, D. M., and Mackenzie, A. S., 1990, Prediction of pore fluid pressures in sedimentary basins, *Marine and Petroleum Geology*, **7**, 55-65.
- Mavco, G. and Mukerji, T., 1998, Bounds on low-frequency seismic velocities in partial saturated rocks, *Geophysics*, **65**, 918-924.
- Mavko, G., Mukerji, T. and Dvorkin, J., 1998, *The rock physics handbook: tools for seismic analysis in porous media*, Cambridge University Press.
- Mavko, G., and Nur, A., 1997, Effect of a percolation threshold in the Kozeny-Carman relation, *Geophysics*, **62**, 1480-1482.
- Miley, M. P., 1999, *Converted modes in subsalt seismic exploration*, Msc, Thesis, Rice University.

- Miley, M. P., and Kessinger, W. P., 1999, Overpressure prediction using converted mode reflections from base of salt, 60th Ann. Internat. Mtg., Soc. Expl. Geophys.. Expanded Abstracts, 880-883.
- Murphy, W. F., 1982, Effect of partial water saturation on attenuation of Massillon sandstone and Vycor porous glass, *Journal of the Acoustical Society of America*, **71**, 1458-1468.
- Murphy, W. F., 1984, Acoustic measures of partial gas saturation in tight sandstones, *Journal of Geophysical research*, **89**, 11549-11559.
- Murphy, W. F., Winkler K. W. and Kleiberg R. L., 1986, Acoustic relaxation in sedimentary rocks: Dependence on grain contacts and fluid saturation, *Geophysics*, **52**, 757-766.
- Norris, A. N., 1993, Low-frequency dispersion and attenuation in partially saturated rocks: *Journal of the Acoustical Society of America*, **94**, 359-370.
- O'Brien J. M., Dan Whitemore N., Bransberg-Dahl S., Etgen T. J., Murphy E. G., 1999, Multicomponent modelling of the Valhall field. Expanded abstract at EAGE 61st Conference & Exhibition-Helsinki, Finland, 7-11 June, 1999.
- O'Connell R. J. and Budiansky B. 1977, Viscoelastic properties of fluid-saturated cracked solids, *Journal of Geophysical Research*, **82**, 5719-5735.
- Ogushwitz, P. R., 1985, Application of the Biot Theory. II. Suspension, *Journal of the Acoustical Society of America*, **77**, 441-452.
- Reid, R. C., Prausnitz, J. M., and Poling, B. E., 1987, *The properties of gases and liquids*, Mc-Graw-Hill Book Co.
- Reuss, A., 1929, Berechnung der fließgrenze von minkristallen: *Zeitschrift für Angewandte Mathematik und Mechanik*, **9**, 49-58.
- Pennebaker, E., 1968, Seismic data indicate depth and magnitude of abnormal pressures, *World*, **166**, 73-78.
- Pham, N. H., Carcione, J. M., Helle, H. B. and Ursin, B., 2001, Poro-viscoelastic representation of shaley sandstones with partial saturation. Expanded abstract at EAGE/SEG Workshop on Reservoir Rocks-Pau, France, 30 April - 4 May, 2001.
- Pham, N. H., Helle, H. B., and Carcione, J. M., 2002a, Velocity and attenuation in partially saturated rocks - Numerical experiments. Expanded abstract at EAGE 64th Conference & Exhibition - Florence, Italy, 27-30 May, 2002.

Pham, N. H., Carcione, J. M., and Helle, H. B., 2002b, Effects of frequency and fluid distribution on elastic waves in partially saturated rocks: Poroelastic numerical experiments. Expanded abstract in 2nd Biot Conference on Poromechanics - Grenoble, 26-28 Aug., 2002.

Pham, N. H., Carcione, J. M., Helle, H. B., and Ursin, B., 2002c, Wave velocities and attenuation of shaley sandstones as a function of pore pressure and partial saturation. Accepted for publication in Geophysical Prospecting.

Pointer, T., Liu, E., and Hudson, J. A., 2000, Seismic wave propagation in cracked porous media, *Geophysical Journal International*, **142**, 199-231.

Prasad, M., and Manghnani, M., H., 1997, Effects of pore and differential pressure on compressional wave velocity and quality factor in Berea and Michigan sandstones. *Geophysics* **62**, 1163-1762.

Sahay, J. N., 1994, Natural field variables in dynamic poroelasticity, Mtg. soc. Expl. Geophys.. Expanded Abstracts, 1163-1166.

Sayers, C. M., Johnson, G. M., and Denyer, G., 2000, Predrill pore pressure prediction using seismic data, IADC/SPE Drilling Conf., #59122.

Spencer T. W., Sonnad R. J., and Butler M. T. 1982, Sesmic Q-Stratigraphy or dissipation, *Geophysics*, **47**, 16-24.

Stoll, R. D., and Bryan, G. M., 1970, Wave attenuation in saturated sediments: *J. Acous. Soc. Am.*, **47** (2), 1440-1447.

Teja, A. S. and Rice, P., 1981a, Generalized corresponding states method for viscosities of liquid mixtures, *Industrial Engineering Chemistry Fundamentals*, **20**, 77-81.

Teja, A. S. and Rice, P., 1981b, The measurement and prediction of the viscosities of some binary liquid mixtures containing n-hexane, *Chemical Engineering Science*, vol. **36**, 7-10.

Toksöz, M. N., Johnston, D. H. and Timur, A. T., 1979, Attenuation of seismic waves in dry and saturated rocks - I laboratory measurements: *Geophysics, Soc. of Expl. Geophys.*, **44**, 681-690.

Traugott, M., 1997, Pore/fracture pressure determinations in deep water, *Deepwater Technology supplement, World Oil*, **218** August issue.

Ursin B. and Toverud T., 2002, Comparison of seismic dispersion and attenuation models, *Studia geophysica & geodaetica*, **46**, 293-320.

Van Genuchten, M. T., 1978, Calculating the unsaturated hydraulic conductivity with a closed form analytical model. Report 78-WR-08, Princeton University, NJ.

Voigt, W., 1928, Lehrbuch der kristallphysik: Teubner.

Vo-Thang D., 1990, Effects of fluid viscosity on shear-waves attenuation in saturated sandstones, *Geophysics*, **55**, 712-722.

White J. E., 1975, Computed seismic speeds and attenuation in rocks with partial saturation, *Geophysics*, **40**, 224-232.

White, J. E., Mikhaylova, N. G., and Lyakhovitsky, F. M., 1975, Low-frequency seismic waves in fluid saturated layered rocks: *Izvestija Academy of Sciences USSR, Phys. Solid Earth*, **11**, 654-659.

Winkler K. W. and Nur A. 1979, Pore fluids and seismic attenuation in rocks, *Geophysical Research Letters*, **6**, 1-4.

Winkler, K. W., and Nur, A., 1982, Seismic attenuation: Effects of pore fluid and frictional sliding: *Geophysics*, **47**, 1-15.

Wood, A. W., 1955, *A Textbook of Sound*, The MacMillan Co., New York, 360 pp.

Worthington, P. F., 1991, Reservoir characterization at the macroscopic scale. In: *Reservoir Characterization II*, (eds. L. W. Lake et al.), 123-165. Academic Press Inc.

Yin, C. S., Batzle, M. L., and Smith, B. J., 1992, Effects of partial liquid/gas saturation on extensional wave attenuation in Berea sandstone, *Geophysics Research Letters*, **19**, 1399-1402.

Zener, C., 1948, *Elasticity and anelasticity of metals*, University of Chicago Press.

Zimmerman, R. W., 1991, *Compressibility of sandstones*, Elsevier, New York.